UNIVERSITY OF CALIFORNIA SAN DIEGO

Hydrodynamics in Intermittently Closed Estuaries Over Multiple Timescales and Varying Forcing Conditions

A dissertation submitted in partial satisfaction of the
requirements for the degree Doctor of Philosophy

in

Oceanography

by

Madeleine Harvey

Committee in charge:

Sarah Giddings, Chair
Jeff Crooks
Falk Feddersen
Timu Gallien
Eugene Pawlak
Eric Terrill

2019

The dissertation of Madeleine Elizabeth Harvey is approved, and it is acceptable in quality and form for publication on microfilm and electronically:

_____

_____

_____

_____

_____

_____

Chair

University of California San Diego

2019

EPIGRAPH

I really don't know why it is that all of us are so committed to the sea, except I think it is because in addition to the fact that the sea changes and the light changes, and ships change, it is because we all came from the sea... When we go back to the sea, whether it is to sail or to watch it we are going back from whence we came.

-President John F. Kennedy

TABLE OF CONTENTS

LIST OF FIGURES

LIST OF TABLES

ACKNOWLEDGEMENTS

I acknowledge my advisor, Sarah Giddings, for teaching me how to be an oceanographer. Her dedication and guidance over the last six years have made me a better scientist, critical thinker, and communicator. She has put in countless hours going above and beyond typical advisor duties from arriving at pre-dawn field deployments with breakfast treats to staying up late into the night to provide insightful and constructive feedback on presentations or papers when I mismanaged deadlines. Above all she has been in incredible role model and mentor; I cannot thank her enough for all that she taught me. I also acknowledge my committee members, Drs. Jeff Crooks, Geno Pawlak, Timu Gallien, Falk Feddersen, and Eric Terrill, for their time and insightful feedback.

I'd like to thank Angelica and Isa who were both were amazing sources of support through all the ups and downs of this adventure. I dragged them both into the thigh high mud countless times, and yet they always came back with smiles on their faces ready to assist in whatever way possible. The observations here would have been possible without the help of volunteers including Andre, Andrew, and, Mia, Alex; past and present lab members including Jack, Adrian, and Alma; and the Guza field crew. I'd like to thank Brian, Kent, Rob, Lucian, Greg, Bill, and Michelle for all their hard work and for helping me become more competent in the field.

Thank you to Southern California SeaGrant, California SeaGrant, and California Department of Boats and Waterways for funding the research.

This would not have been possible with support of Mike Hastings from the Los Peñasquitos Lagoon Foundation and Darren Smith and Cara Stafford from CA State Parks. Additionally, the support of all the staff at TJNERR especially Jeff and Justin McCullough.

It has been a privilege to be a part of the SIO community. Thank you to my classmates, officemates, and colleagues, especially the 2013 cohort. I feel lucky to have so many colleagues whom I also consider to be my personal friends. I'm especially grateful to Sarah and Dara (and Dox) for becoming my sisters and building a home with me in San Diego.

I would not be where I am today without the love and support of my family. To James, thank you for moving to San Diego and being my companion on countless adventures. To John and Katharine, thank you for teaching me that physics is cool and for the occasional free meal. To Olivia, your perseverance and strength inspires me each and every day. To Mom and Dad, thank you for helping me discover my passions, instilling in me the value of education and hard work, and encouraging me in all my endeavors.

To the many friends and family members in San Diego and beyond have provided encouragement and support, thank you!

Chapter 2, in full, is currently being prepared for submission for publication of the material to Estuaries and Coasts. Harvey, Madeleine E.; Giddings S. N. Pawlak G.; Crooks, J. The dissertation author was the primary investigator and author of this paper.

Chapter 3, in full, is currently being prepared for submission for publication of the material to Estuaries and Coasts. Harvey, Madeleine E.; Giddings S. N. Pawlak G.; Crooks, J. The dissertation author was the primary investigator and author of this paper.

Chapter 4, in part is currently being prepared for submission for publication of the material. Harvey, Madeleine E.; Giddings S. N. Pawlak G.; Crooks, J; Davis, K. The dissertation author was the primary investigator and author of this material.

Chapter 5, in full, is a reproduction of Madeleine Harvey, Sarah N. Giddings, Eric D. Stein, Jeffrey A. Crooks, Christine Whitcraft, Timu Gallien, John L. Largier, Liesl Tiefenthaler, Hallee Meltzer, Geno Pawlak, Karen Thorne, Karina Johnston, Richard Ambrose, Stephen C. Schroeter, Henry M. Page, Hany Elwany (2019) Effects of Elevated Sea Levels and Waves on Southern California Estuaries during the 2015-2016 El Niño. *Estuaries and Coasts.* I was the primary investigator and author of this work.

VITA

2012 Bachelor of Science (Civil Engineering with a focus in Environmental Problem Solving and Planning), Brown University, Providence, RI

2016 Master of Science (Oceanography), University of California San Diego

2019 Doctor of Philosophy (Oceanography), University of California San Diego

PUBLICATIONS

Harvey, M.E., S.N. Giddings, E. Stein, J. Crooks, C. Whitcraft, T. Gallien, J. Largier, L. Tieffenthaler, H. Meltzer, G. Pawlak, K. Thorne, K Johnston, R. Ambrose, S. Schroeter, H. M. Page, H. Elwany (2019), Effects of elevated sea levels and waves on Southern California estuaries during the 2015-2016 El Niño. Estuaries and Coasts.

Young, A., R. Flick, T. Gallien, S. Giddings, R. Guza, **M. Harvey**, L. Lenain, B. Ludka, W. K. Melville, W. O'Reilly (2018), Southern California Response to the 2015-2016 El Nino. JGR: Earth Surface.

Harvey, M.E., S.N. Giddings, and G. Pawlak (2015), Morphodynamic and hydrodynamic responses to wind and wave events in a small Southern California Estuary, in P. Wang, J.D. Rosati, and J. Cheng. The Proceedings of the Coastal Sediments 2015. Coastal Sediments 2015, San Diego, USA. World Scientific. doi: 10.1142/9789814689977_0088.

ABSTRACT OF THE DISSERTATION

Hydrodynamics in Intermittently Closed Estuaries Over Multiple Timescales and Varying Forcing Conditions

by

Madeleine Elizabeth Harvey

Doctor of Philosophy in Oceanography

University of California San Diego, 2019

Professor Sarah N. Giddings, Chair

Small, shallow, low-inflow estuaries (LIEs) are common worldwide along steep coasts in regions with low or seasonal precipitation. LIEs along coasts with strong wave conditions are termed bar-built estuaries (BBEs) where a sand-bar sill near the mouth due to current and wave-driven sediment transport. The sill height and location can have profound impacts on the circulation, inundation, stratification, and dissolved oxygen in the estuary. In intermittently

closed estuaries (ICEs) the sill can periodically accrete to block the ocean-estuary exchange. In Los Peñasquitos Lagoon, an ICE in Southern California, the hydrodynamic variability of these traditionally under-researched systems is investigated through extensive observations.

Four and half years of continuous hydrodynamic observations over several periods of climatology add valuable insight into how ICEs respond to changing nearshore and upstream forcings. Observations during the open state reveal that when the sill near the mouth is low, the estuary functions like a canonical estuary with evidence of strain-induced period stratification and canonical exchange flows. As the sill accretes, tidal circulation weakens, and the estuarine exchange does not scale with the canonical pressure-friction balance.

When the inlet closes, estuary-ocean exchange is interrupted, and estuarine water levels increase due to freshwater inflows and overtopping. Reduced mixing due to interrupted tidal exchange and increased stratification due to freshwater inputs lead to hypoxic conditions developing at depth. The diurnal circulation when closed is forced by differential heating and cooling driving thermal exchange that can be weakened by strong diurnal winds.

To put the dynamics of LPL in context with similar estuaries, water levels were measured in 12 additional Southern California estuaries during the 2015-2016 El Niño winter. Water levels inside perennially open estuaries mirrored ocean water levels. ICEs exhibited enhanced higher-high water levels than offshore during large waves, and lower-low water levels were truncated due to the sill at the mouth, resulting in elevated detided water levels. The sill height and wave exposure were important to the individual estuarine response to ocean conditions. Understanding how LIEs, BBEs, and ICEs respond to increased sea levels and waves and the factors that influence closures will help managers develop appropriate adaptation strategies.

Chapter 1

Introduction

1.1 Background

Estuaries and associated wetlands provide extensive ecosystem functions and services, including biodiversity support, carbon sequestration, water quality improvement, and flooding abatement (e.g., Zedler and Kercher, 2005; Takekawa et al., 2011; Holmquist et al., 2018). It is important to understand how such systems will respond and adapt to climate change. In particular, the role of wetlands and estuaries in mitigating the effects of sea-level rise are not well-understood (Shepard et al., 2011). This is especially true in under-researched systems such as low-inflow estuaries.

Low-inflow estuaries (LIEs) are found worldwide (e.g., Australia, South Africa, Portugal, Spain, Morocco, Chile, Mexico, and the United States; Largier, 2010) and receive smaller and more episodic freshwater inputs than their "classical" counterparts found in wetter climates with larger watersheds (Largier et al., 1997; Ranasinghe and Pattiaratchi, 2003; Behrens et al., 2013; Rich and Keller, 2013; Williams and Stacey, 2016). In Southern California, all estuaries are LIEs and are threatened by both continued urbanization and climate change. More than 100 LIEs line the highly urbanized Southern California coastline (Doughty et al., 2018), all with varying degrees of physical modifications, including the damming and channelizing of river inflows; the construction of breakwaters and jetties at estuary inlets; the dredging of channels, inlets, and harbors; the construction of roads splitting systems; and the direct filling of wetlands (e.g., Pratt 2014; Los Peñasquitos Lagoon Foundation et al., 2016). Despite these threats, these systems are extremely important to the regional economy and ecology (Zedler and Kercher, 2005; California Natural Resources Agency, 2010).

Unlike in canonical estuaries where salinity decreases with distance from the ocean and a resulting density gradient drives an exchange flow, LIEs can exhibit reduced density gradients and can even become hypersaline during the dry season. This can stagnate the flow or, in certain conditions, reverse density gradients can induce an inverse estuarine exchange (Largier et al., 1997; Ranasinghe and Pattiaratchi, 2003; Behrens et al., 2013; Rich and Keller, 2013; Williams and Stacey, 2016). In some LIEs, urban runoff or upstream dam releases may suppress hypersalinity development (Largier et al., 1997).

In general, LIEs along coasts with strong wave conditions are bar-built estuaries (BBEs) affected by the presence of a wave-built bar/sill, and subject to mouth closure. BBEs are generally small, shallow systems with narrow tidal inlets (estuary mouth, cross-sectional area on the order of 100 m^2 or less) (Ranasinghe & Pattiaratchi, 2003) that experience rapid morphological changes. They are common on wave-dominant coasts with seasonal rainfall and microtidal (Cooper, 2001; Davidson et al., 2009) or mesotidal (Behrens et al., 2013; Rich & Keller, 2013) tidal range. BBEs can be found on worldwide including: California (Largier et al., 1996), Spain (Moreno et al., 2010), Portugal (Bertin et al., 2019; Dodet et al., 2013), Australia (Gale et al., 2007; Ranasinghe & Pattiaratchi, 1999; Roy et al., 2001), South Africa (Clark & O'Connor, 2019; Largier et al., 2019), and Chile (Dussaillant et al., 2009). In BBEs, flood tides, waves, and wave-current interactions drive alongshore and cross-shore sediment transport into the estuary inlets forming a sill comprised of sand and cobbles while ebb tides and fluvial events drive transport out of these systems (Behrens et al., 2013; Orescanin & Scooler, 2018; Ranasinghe et al., 1999; Rich & Keller, 2013). The sill height and location can have profound impacts on the circulation, inundation, stratification, and dissolved oxygen in the estuary (Behrens et al., 2016; Cousins et al., 2010; Gale et al., 2007; Largier et al., 1992). The estuary

tidal range depends on both the offshore tidal range and the sill height and location. For the flooding higher tides, the estuary and ocean water levels are approximately the same, allowing for connection between the nearshore ocean and estuarine environments. As the tide falls to its daily lower-low, the ocean retreats below the elevation of the sill and the nearshore ocean dynamically disconnects from the estuary (Williams & Stacey, 2016).

During particularly low river discharge, and/or large wave conditions, wave-driven sediment accumulation exceed tidal/fluvial erosion raising the sill and forming a barrier sill, completely separating the estuary and ocean (e.g., Largier et al., 1992; Elwany et al., 1998; Morris & Turner 2010; Behrens et al., 2011; Behrens et al., 2013; Rich & Keller 2013; Orescanin & Scooler 2018). Under these conditions, the estuary becomes akin to a salt-stratified lake and is considered closed. The duration of inlet closures can range from a part of a day to several years (Hastings and Elwany 2012; Behrens et al., 2013). A common feature globally, estuaries that close intermittently have been referred to by many names (Tagliapietra et al., 2009), including intermittently closed and open lakes and lagoons (ICOLL, Roy et al., 2001), seasonally open tidal inlets (Ranasinghe et al., 1999), temporarily opening and closing estuaries (TOCE, Whitfield 1992), intermittently open estuaries (IOE, Jacobs et al., 2010), intermittently open/closed estuaries (IOCE, McSweeney et al., 2017), as well as intermittently closed estuaries (ICE, Williams & Stacey 2016), the latter we use here.

Following closures, tidal circulation ceases and the estuarine vertical stratification and circulation can be influenced by wind, thermal heating, precipitation, and evaporation (Gale et al., 2006; Williams 2014; Behrens et al., 2016). Wind can upwell the denser layer inducing a longitudinal density gradient that can drive a horizontal circulation and generate a seiche when it relaxes (Okely and Imberger 2007; Behrens et al., 2016). Closures can significantly impact the

water quality of ICEs. Strong vertical stratification inhibiting vertical mixing combined with a lack of tidal flushing during closures can lead to hypoxia in the bottom waters (Gale et al., 2006; Becker et al., 2009; Cousins et al., 2010) in some ICEs. Hypoxia (dissolved Oxygen concentration < 2 mg/L) can stress organisms and induce fish kills and death of benthic organisms.

In developed regions such as Southern California, many ICEs fail to re-open naturally due to adjacent beach nourishment (Ludka et al., 2018), reduced tidal prism, structurally impeded inlet migration, and altered fluvial inputs (Hastings and Elwany 2012). This results in environmental concerns, including flooding of low-lying development, undesirable water quality and impacts to fish and other marine organisms that require management attention (Largier et al., 2019). Many Southern California ICEs are managed to maintain an open state through dredging, building hard structures to prevent sedimentation and enhance scour, or some combination of methods that functionally convert these ICEs to perennially open estuaries (POEs).

Due to the desire to keep inlets open for navigation and water quality purposes, much of the research in BBEs, particularly ICEs, has focused on understanding closure mechanisms (Gale et al., 2007; Ranasinghe & Pattiaratchi, 1999b; Roy et al., 2001). Less work has focused on the hydrodynamics of these systems in general, nor in the context of canonical estuarine theories (Geyer & MacCready, 2013; MacCready & Geyer, 2010). Some studies (Gale et al., 2006, 2007; Ranasinghe & Pattiaratchi, 2003) have examined the open inlet periods. While a few studies have examined the impact of the sill on the dynamic connection to the ocean (Williams & Stacey, 2016) and on the hydrodynamics during closed periods (Gale et al., 2006; Williams, 2014; Behrens et al., 2016), few have examined the variability of closures over multiple closures and multiple years. In general, few long-term studies of LIEs exist with the notable exception of

a study in Elkhorn Slough a small system in Central California that is open year-round and develops an inverse circulation during the summer and fall months (Nidzieko and Monismith 2013).

This dissertation seeks to provide new insights into the dynamics of small, shallow, bar-built and intermittently closed estuaries and address how they change over various time scales including tidal, diurnal, spring-neap, seasonal, and interannual. Unprecedented field observations were collected in Los Peñasquitos Lagoon (LPL) as well as 12 additional Southern California LIEs (Figure 1.1). Long-term continuous field observations in LPL are presented from December 2014 through May 2019 (Figure 1.2). These deployments covered several unique periods for Southern California climatology, allowing us to address interannual variability, seasonal variability, and response to oceanic and upstream forcing events. Moreover, the study period included 28 closed periods allowing an unprecedented examination of estuarine closure mechanisms, and circulation during the closed state. Long-term observations focused on physical parameters including water level, waves, bathymetry, currents, salinity, temperature, density, and oxygen. An intensive experiment in March and April of 2017 used a novel technology, a Distributed Temperature Sensing (DTS) system, to augment longer-term observations. Additionally, during the 2015-2016 winter, observations from 12 additional Southern California LIEs were gathered and used to compare estuarine response to similar offshore forcing conditions.

This dissertation first focuses on the detailed dynamics within LPL and then expands to a comparison that allows us to draw broader conclusions and discuss implications for LIEs and BBEs worldwide. First, in Chapter 2 I address the hydrodynamics of open, bar-built estuaries including how waves drive sediment into BBEs, how the tidal dynamics of BBEs change over

spring-neap cycles and various stages of sill height, placing the results in the context of traditional estuarine theory. In Chapter 3 I describe the general stratification patterns and circulation characteristics of the closures during different seasons. I then discuss how the frequency of closures has change over time and what drives some of the seasonal and diurnal variability during the closures. In Chapter 4 to complement longer-term studies, a DTS system, a novel tool was deployed to observe the along-channel and cross-channel bottom water temperature fluctuations and to assess the circulation, frontal propagation, and mixing in the estuary at unprecedented temporal and spatial resolution. In Chapter 5 I examine how anomalous ocean forcing from the 2015-2016 El Niño affected 13 LIEs in Southern California and compare the response of perennially open estuaries to ICEs. Finally, we briefly summarize the results and the implications for low-inflow, ICEs and BBEs worldwide.

1.1 Primary Study Site: Los Peñasquitos Lagoon

Between December 2014 and May 2019 measurements were conducted in Los Peñasquitos Lagoon (LPL) a small, bar-built estuary in Southern California (Figure 1.1). LPL is located in a Mediterranean climate with little precipitation during the summer and episodic inputs during the winter. LPL serves as the outlet to a 255 km^2 watershed draining Carmel Valley, Los Peñasquitos Canyon and Carroll Canyon (see Figure 1.1b). The estuary is a designated Natural Marsh Preserve by the state of California and is part of the Torrey Pines State Reserve. LPL is small and shallow (max depth less than 4 m) estuary covering approximately 2 km^2 with extensive marsh habitat (Figure 1.1c). The main channel is about 2.5 km long and less than 70 m wide. The estuary inlet crosses a nourished sand and cobble beach (last major nourishment in 2001 (SANDAG, 2018), minor nourishments every year during inlet dredging) which accretes in the summer and erodes in the winter (Ludka et al., 2016).

LPL has been subjected to physical modifications in and around the estuary which impact its hydrodynamics and connectivity with the ocean. In 1925 a railway berm was relocated to the middle of the estuary and between 1932-1933 Highway 101 (now Torrey Pines Road) was constructed along a berm along the ocean edge of the estuary. From 2015-2017 three wooden railway trestle bridges were replaced with concrete bridges. Over the main span a bridge with about 96 timber pilings was replaced with a concrete bridge with 27 concrete pilings. Historically the inlet location was able to migrate along the coast, however, during Highway 101 construction, the inlet was moved approximately 0.5 km south of its 1932 location and constricted to a bridge opening. The bridge was rebuilt in 2004-2005 leading to the current 38 m wide constricted inlet. According to historical records and a study of marsh sediments (Cole & Wahl, 2000; Scott et al., 2011), prior to development the inlet was primarily open with the first closure being recorded during the first railway construction in the late 1880s (Hastings & Elwany, 2012). While LPL was historically a LIE with hypersaline conditions likely developing during late summer and fall, increased freshwater runoff from urban development (White & Greer, 2006) prevents the main channel from becoming hypersaline (Largier et al., 1997) although smaller arms do continue to become seasonally hypersaline. Moreover, construction of an upstream damn and water impoundments have decreased winter time river flows (Henning et al., 2012).

Inlet constrictions, changes to the hydrograph, and infrastructure along the rivers as well as inside and adjacent to the estuary have increased the frequency of closure (Hastings & Elwany, 2012). The inlet is frequently dredged (Hastings & Elwany, 2012) in response to a combination of vector borne disease, flooding, and low dissolved oxygen, costing approximately $115,000 to $130,000 for each dredging event (Mike Hastings, personal communication). A

major restoration is proposed in the estuary in the coming years (Los Peñasquitos Foundation, 2016). Thus while the work presented in this dissertation is focused on understanding LIE and BBE dynamics in general, the results from LPL specifically will be useful for local restoration efforts and interpreting the estuary's potential response to climate change.

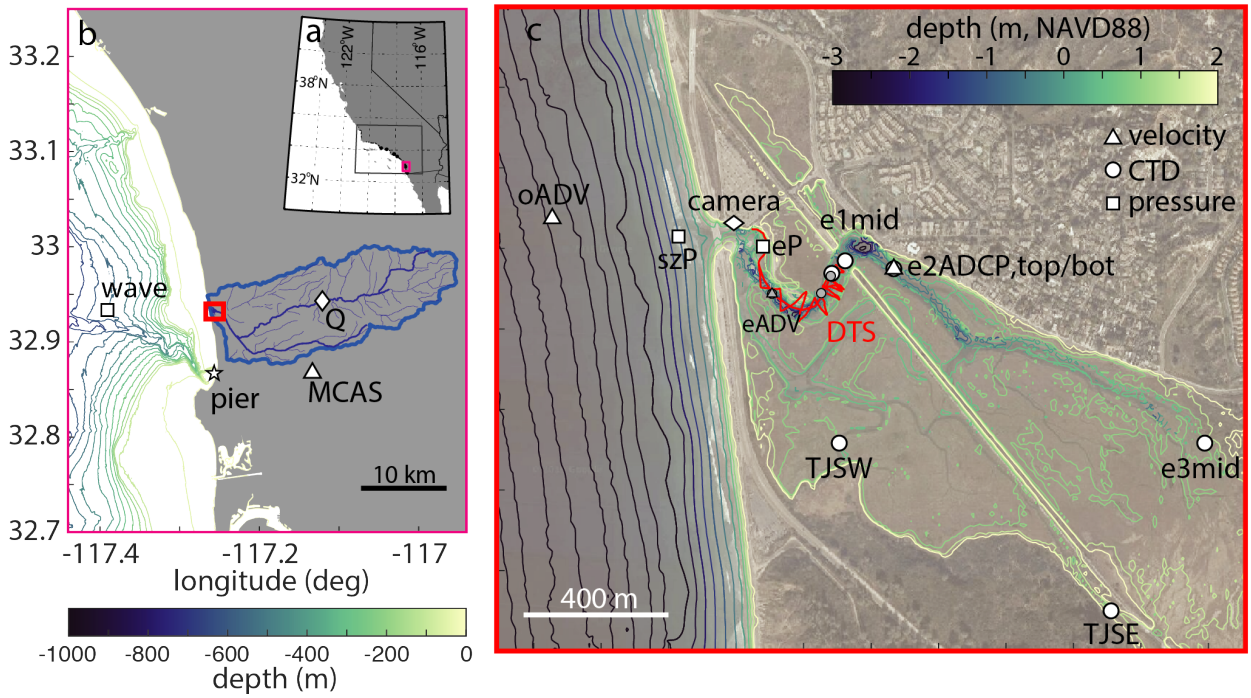

Figure 1.1: Location of Los Peñasquitos Lagoon and instruments deployed. a.) California coastline with San Diego delineated. b.) San Diego coastline with watershed of Los Peñasquitos Lagoon and offshore bathymetry. c.) Image of Los Peñasquitos Lagoon with instrument locations (white for nearly continuous measurements, gray and red for short-term deployments) overlain on marsh topography and bathymetry in teal (light colors are higher elevation). Estuary bathymetry was collected from a combination of UAV measurements and towed ADCP measurements, while those offshore are from the 1/3 arc-second San Diego Coastal DEM model from NOAA and all are referenced to NAVD88.

1.1 Overview of Observations

Between December 2014 and May 2019 measurements of the physical oceanographic parameters (Figure 1.1b, c, and Figure 1.2) were conducted in Los Peñasquitos Lagoon (LPL) a small, bar-built estuary in Southern California (Figure 1.1). A mooring at e2 (e indicates an estuary mooring with numbers increasing upstream) with a bottom-mounted ADCP with a surface CTD and bottom CTD-DO was deployed for most of the record. During the winters wave measurements of the nearshore, surfzone, and inlet (oADV, szP, and eP; ocean, surfzone and estuary respectively) were collected. For a short period, current and wave measurements were conducted near the inlet at eADV. Bathymetry measurements near the inlet were collected first

with a RTK GPS system and then with structure-from-motion photogrammetry from drone high-resolution imagery. A DTS was deployed with for a 1-month study with additional instrumentation including CTDs and thermistors. Periodic CTD casts were taken throughout the observation period.

We were lucky to have a wealth of additional longer term monitoring programs in the estuary, watershed and coastal zone. Additional instrumentation included CTDs and cameras maintained by Tijuana National Estuary Research Reserve (TJNERR) System-Wide Monitoring Program (Figure 1.1c), a stream gauge maintained by the USGS Geological Survey (USGS, Figure 1.1b), two offshore wave buoys maintained by Coastal Data Information Program (CDIP, one indicated on Figure 1.1b), three tide gauges maintained by National Oceanic and Atmospheric Administration (NOAA, one marked on Figure 1.1b), weather and hydroclimate stations on Scripps Pier archived by Earth Networks Inc., Daniel R. Cayan, and Douglas J. Alden, and at Miramar air base accessed through the National Climatic Data Center (NCDC, Figure 1.1b), and a CTD on Scripps Pier maintained by Southern California Coastal Ocean Observing System (SCCOOS). Instrumentation used is described in more detail within each chapter.

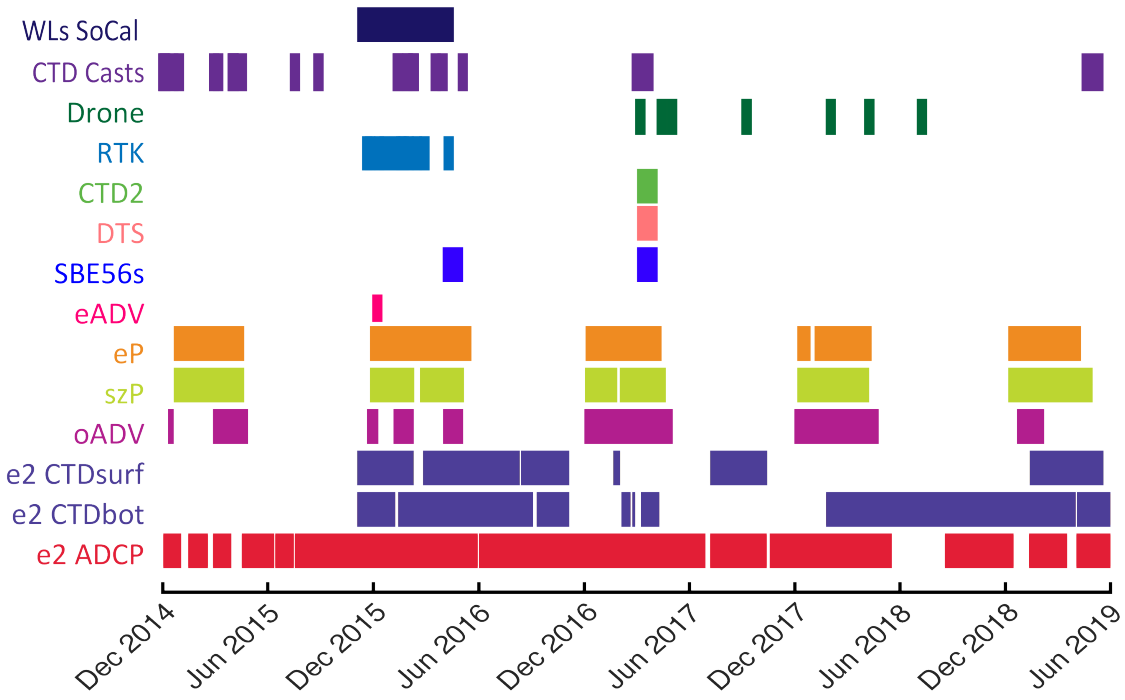

Figure 2.2: Times when instruments were deployed in Southern California. From bottom to top: At e2 nearly continuous ADCP and surface and bottom CTD measurements were collected. During the winters wave measurements were collected at oADV, szP, and eP. eADV was deployed briefly in January 2016. Several thermistors were deployed as at DTS test study the spring prior to the DTS deployment. During the DTS deployment several additional moorings and thermistors were deployed. Bathymetry measurements were conducted periodically first with an RTK GPS and then with an UAV and structure-from-motion photogrammetry. CTD casts were taken periodically during the observation period. During the 2015-2016 El Nino, water levels were measured in 12 additional estuaries throughout Southern California.

Chapter 2

Variability of the Hydrodynamics of an Intermittently Closed Estuary over Interannual, Seasonal, Fortnightly and Tidal Timescales

Shallow, low-inflow, bar-built estuaries are subject to intermittent mouth closures due to sill accretion near the mouth. Low-inflow and bar-built estuaries are common in Mediterranean climates worldwide, however their dynamics have been less well studied relative to more canonical estuaries. Here, we present hydrodynamic observations from Los Peñasquitos Lagoon, a low-inflow, bar-built, intermittently closed estuary in Southern California. Over 4 years of continuous hydrodynamic observations elucidate tidal, fortnightly, seasonal, and interannual variability in circulation. Tidal phase averages of conditions during open, partially-closed, spring, neap, and closed conditions highlight the large dynamic range that these estuaries experience. During open conditions, especially when the sill is low, circulation is similar to that in many deeper canonical estuaries, impacted by temporal variations in shear and stratification consistent with stratification-induced periodic straining and exhibiting a canonical subtidal estuarine exchange flow. However, as the sill grows, tidal circulation weakens and becomes strongly sheared and the estuarine exchange does not scale with the canonical pressure-friction balance, likely due to hydraulic processes at the sill. Wave observations near the estuary inlet show that wave energy in the system is dependent on sill height and has a strong tidal variation due to wave-current interactions.

2.1 Introduction

Low-inflow estuaries (LIEs) are commonly found in Mediterranean climates with episodic or seasonal river flow (Largier et al., 1997, 2013; Nidzieko & Monismith, 2013). Unlike in canonical estuaries where salinity decreases with distance from the ocean and a resulting density gradient drives an exchange flow, LIEs can exhibit reduced density gradients and even become hypersaline during the dry season. Weak density gradients can stagnate the flow or, in certain conditions, reverse density gradients can induce an inverse estuarine exchange. In some instances, while an estuary may have historically functioned as a LIE, urban runoff or upstream dam releases may be strong enough to suppress hypersalinity development (Largier et al., 1997).

Bar-built estuaries (BBEs) are a type of LIE. They are generally small, shallow systems with narrow tidal inlets (estuary mouth, cross-sectional area on the order of 100 m^2 or less) (Ranasinghe & Pattiaratchi, 2003) that experience rapid morphological changes. They are common on wave-dominant coasts with seasonal rainfall and microtidal (Cooper, 2001; Davidson et al., 2009) or mesotidal (Behrens et al., 2013; Rich & Keller, 2013) tidal range. BBEs can be found on Mediterranean coasts worldwide including: California (Largier et al., 1997, 2013; Nidzieko & Monismith, 2013), Spain (Moreno et al., 2010), Portugal (Bertin et al., 2019; Dodet et al., 2013), Australia (Gale et al., 2007; Ranasinghe & Pattiaratchi, 1999; Roy et al., 2001), South Africa (Clark & O'Connor, 2019; Largier et al., 2019), and Chile (Dussaillant et al., 2009). In BBEs, flood tides, waves, and wave-current interactions drive alongshore and cross-shore sediment transport into the inlets forming a sill comprised of sand and cobbles while ebb tides and fluvial events drive transport out of these systems (Behrens et al., 2013; Orescanin & Scooler, 2018; Ranasinghe et al., 1999; Rich & Keller, 2013). The sill height and location can have profound impacts on the circulation, inundation, stratification, and dissolved oxygen in the system (Behrens et al., 2016; Cousins et al., 2010; Gale et al., 2007; JL Largier et al., 1992). In

some BBEs, the dynamic inlet morphology can occasionally lead to inlet closures, in which case they are termed Intermittently Closed Estuaries (ICEs).

Wave-current interaction plays an important role in the circulation of tidal inlets (Behrens et al., 2013; M. M. Orescanin & Scooler, 2018; Ranasinghe et al., 1999; Rich & Keller, 2013). At the inlet, sea and swell waves can become blocked during ebb tides while they are able to propagate during flood tides. Wave radiation stress gradients can induce a water level set up within single inlet estuaries (Dodet et al., 2013; Olabarrieta et al., 2011). Recent work has focused on the influence of infragravity (IG hereafter) waves in sediment transport within tidal inlets. (Bertin et al., 2019; Dodet et al., 2013) provides a comprehensive review of the generation mechanisms of IG waves, their propagation and transformation in the nearshore, and their effects on coastal environments including on sediment transport and tidal inlet morphodynamics. Uncles et al. (2014) observed IG motions in a Spanish ria with velocities between ~0.1 ms^{-1} and ~0.4 ms^{-1} that traveled into the tidal river. In Pescadaro Estuary in Northern California, (Williams & Stacey, 2016) observed that the strength of IG motions resembling tidal bores correlated with offshore wave heights, and that the IG energy depended on the tidal phase and connectivity between the ocean and estuary. Additionally, they noted that IG orbital motions were on the same order as tidal velocities. In Albuferia Lagoon Inlet, Bertin and Olabarrieta (2016) noted that field observations and numerical simulations using XBeach show that IG waves are present in the lagoon during flood and high tide but are blocked during ebb tides and that IG wave-induced currents can reach 100% of the low-passed flood currents. Bertin et al. (2019) found that in storm wave conditions during flood tides, peaks in along-stream velocity currents occurred during the passage of IG wave crests and currents were reduced or reversed during the passage of troughs. Instantaneous sand fluxes increased up to 2 orders of magnitude during IG wave crests, which

contributed to inlet accretion. In the Carmel River in Central California, (M. M. Orescanin & Scooler, 2018) IG energy was only seen in the system just before closure when the river flow decreased in magnitude.

Due to the desire to keep inlets open for navigation and water quality purposes, much of the research in BBEs, particularly ICEs, has focused on understanding closure mechanisms (Gale et al., 2007; Ranasinghe & Pattiaratchi, 1999b; Roy et al., 2001). Less work has focused on the hydrodynamics of these systems in general, nor in the context of canonical estuarine theories (Geyer & MacCready, 2013; MacCready & Geyer, 2010). Some studies (Gale et al., 2006, 2007; Ranasinghe & Pattiaratchi, 2003) have examined the open inlet periods in microtidal systems (Hayes, 1979). A few studies have examined the impact of the sill on the dynamic connection to the ocean (Williams & Stacey, 2016) and on the hydrodynamics during closed periods in mesotidal systems (Hayes, 1979). In mesotidal BBEs, the estuary tidal range depends on both the offshore tidal range and the sill height and location. During the flooding higher tides, the estuary and ocean water levels are approximately the same, allowing for connection between the nearshore ocean and estuarine environments. As the tide falls to its daily lower-low, the ocean retreats below the inlet of the perched estuary and the nearshore ocean dynamically disconnects from the estuary (Williams & Stacey, 2016). Following closures, wind becomes an important forcing mechanism, leading to internal seiche motions forced by diurnal winds (Behrens et al., 2016) and wind dominated vertical mixing (Gale et al., 2006).

The hydrodynamics of BBEs and ICEs have historically been under studied, potentially because the shallow waters and turbulent wave activity near the inlet have prevented these systems from being used as ports and harbors (Williams & Stacey, 2016). This paper presents results from extensive field observations from Los Peñasquitos Lagoon (LPL) in Southern

California (Figure 2.1). Field observations were initiated in LPL in December 2014 and continued through May 2019 (Figure 2.2). Deployments in LPL covered several unique periods for Southern California climatology; during 2014-2015 “the Blob,” a Pacific Ocean warm temperature anomaly (Bond et al., 2015; Hartmann, 2015), led to warm ocean and air temperatures and a high pressure system contributing to drought conditions in Southern California. During this period, precipitation was relatively low (21 percent below average since 1939). The winter 2015-2016 El Niño brought above average offshore waves and elevated sea levels and relatively low rain (22 percent below average since 1939) which led to increased duration and frequency of inlet closures (Young et al., 2018). The winters of 2016-2017 and 2018-2019 had higher precipitation, approximately 41% and 37%, respectively percent above average respectively, while the winter of 2017-2018 had extremely low rain, in the bottom 5th percentile since 1939 or 61% below average (National Climatic Data Center, NCDC Station USW0023188).

Observations focused on physical parameters including water level, waves, bathymetry, currents, salinity, temperature, density, and oxygen. Few long data sets in small systems such as LPL exist, with the notable exception of a study in Elkhorn Slough a small system in Central California that is open year-round and develops an inverse circulation during the summer and fall months (Nidzieko & Monismith, 2013). Thus, we are able to provide new insights into the dynamics of a small, shallow, bar-built estuaries and how they change over various time scales including tidal, diurnal, spring-neap, seasonal, and interannual. After describing our methods, we describe the long-term trends in circulation, the wave forcing that propagates into the system, the circulation of the estuary over a tidal cycle with different sill heights, and the circulation of the estuary over a fortnightly spring-neap cycle. We then discuss how the interannual variability of

forcings affect the estuary and how the drive inlet morphodynamics, how those changes affect the tidal circulation, and finally how they affect the residual circulation.

2.1 Methods

2.1.1 Experimental Site Description: Los Peñasquitos Lagoon

Between December 2014 and May 2019 measurements were conducted in Los Peñasquitos Lagoon (LPL) a small, bar-built estuary in Southern California (Figure 2.1). LPL is located in a Mediterranean climate with little precipitation during the summer and episodic inputs during the winter. LPL serves as the outlet to a 255 km^2 watershed draining Carmel Valley, Los Peñasquitos Canyon and Carroll Canyon. The estuary is a designated Natural Marsh Preserve by the state of California and is part of the Torrey Pines State Reserve. LPL is small and shallow (max depth less than 4 m) estuary covering approximately 2 km^2 with extensive marsh habitat (Figure 2.1). The main channel is about 2.5 km long and less than 70 m wide. The estuary inlet crosses a nourished sand and cobble beach (last major nourishment in 2001, (SANDAG, 2018) minor nourishments every year during inlet dredging) which accretes in the summer and erodes in the winter (Ludka et al., 2016).

LPL has been subjected to physical modifications in and around the estuary which impact its hydrodynamics and connectivity with the ocean. In 1925 a railway berm was relocated to the middle of the estuary and between 1932-1933 Highway 101 (now Torrey Pines Road) was constructed along a berm along the ocean edge of the estuary. From 2015-2017 three wooden railway trestle bridges were replaced with concrete bridges. Over the main span a bridge with about 96 timber pilings was replaced with a concrete bridge with 27 concrete pilings. Historically the inlet location was able to migrate along the coast, however, during the Highway 101 construction, the inlet was moved approximately .5 km south of its 1932 location and

constricted to a bridge opening. The bridge was rebuilt in 2004-2005 leading to the current 38 m wide constricted inlet. According to historical records and a study of marsh sediments (Cole & Wahl, 2000; Scott et al., 2011), prior to development the inlet was primarily open with the first closure being recorded during the first railway construction in the late 1880s (Hastings & Elwany, 2012). While LPL was historically a low-inflow estuary with hypersaline conditions likely developing during late summer and fall, increased freshwater runoff from urban development (White & Greer, 2006) prevents the main channel from becoming hypersaline (Largier et al., 1997) although smaller arms do continue to become seasonally hypersaline. Moreover, construction of an upstream dam and water impoundments have decreased winter time river flows (Henning et al., 2012).

Inlet constrictions, changes to the hydrograph, and infrastructure along the rivers as well as inside and adjacent to the estuary have increased the frequency of closure (Hastings & Elwany, 2012). The inlet is frequently dredged (Hastings & Elwany, 2012) in response to a combination of vector borne disease, flooding, and low dissolved oxygen costing approximately $115,000 to $130,000 for each dredging event (Mike Hastings, personal communication). A major restoration is proposed in the estuary in the coming years (Foundation et al., 2016).

2.1.2 LPL Observations

2.1.2.1 Velocity Measurements

A long-term mooring ~0.75 km upstream from the inlet (e2, Figure 2.1) with an upward-looking 1200 kHz acoustic Doppler current profiler (ADCP, RDI Workhorse Monitor) sampling at 0.5 Hz in mode 12 was deployed on a bottom-mounted flat plate measuring velocity in 10-20 cm bins with blanking distances of 0 to 15 cm collecting data in either Beam (December 01, 2014 to February 17, 2015) or Earth coordinates (February 26, 2015 to June 14, 2019). The

ADCP was swapped every 2-3 months collecting a nearly continuous record from December 01, 2014 until June 14, 2019. Due to deployment logistics, the exact location and depth of each deployment varied slightly. They were adjusted to a consistent depth by aligning them to surveyed in pressure sensors at e1 or, if the system was closed, eP.

Individual velocity measurements were ensemble averaged into 10-minute bins. For each deployment, velocities were rotated into the principal axis coordinates (u, v) based on each deployment's maximum variance during open periods. Velocities were transformed into depth-normalized coordinates ($\sigma = z/D$), where D is the instantaneous water depth. Velocities were extracted to the bed (assuming no flow at the bed and interpolating using a shape-preserving piecewise cubic interpolation) and surface (using a quadratic extraction that assumes $\frac{\partial u}{\partial z} = 0$ at the surface). Gray thatched areas on velocity and shear figures indicate extrapolated data. Shear (S) is defined as the along-channel component of shear, $S = \sqrt{\left(\frac{\partial u}{\partial z}\right)^2}$.

2.1.2.2 CTD Measurements

Adjacent to the ADCP at e2 (Figure 2.1), near-surface (mounted just beneath a floating buoy) and near-bottom conductivity, temperature, and depth sensors (CTD, SBE -37 SMP) sampling at 1 minute and 2 minutes (5 minutes after June 2017) respectively, were deployed (Figure 2.2d, light and dark blue). Dissolved oxygen measurements were collected using SBE-63 optical dissolved oxygen sensor at the bed from November 03, 2015 to October 09, 2017 and Jan 10 2019 to June 20 2019 (Figure 2.2e) and at the surface between January 10 2019 and Apr 2 2019. The CTDs periodically experienced significant biofouling and/or sediment entrainment resulting in artificially low salinity measurements. Unrealistic data was removed from all analysis. In some cases, the instrument was not obviously fouled, however data was questionable and is denoted by a dashed line in Figure 2.2d. Surface and bottom density measurements were

used to calculate a bulk stratification using the Brunt–Väisälä frequency, $N^2 = -\frac{g}{\rho_o}\frac{\Delta\rho}{\Delta z}$ where ρ_o is the average density.

In addition to the moorings, four CTD-DO instruments with turbidity and pH (YSI dataSondes) were deployed on pilings by the Tijuana River National Estuarine Research Reserve (TRNERR) System Wide Monitoring Program (SWMP) fixed at approximately 1 m above the bed (i.e., mid-water column) sampling at 15-minute intervals. Two instruments at e1 and e3 (upstream and downstream of our ADCP/CTD mooring respectively) were deployed in the main channel (Figure 2.1, Figure 2.2d, medium blue (e1mid) and purple (e3mid)) and two (TJSW and TJSE) were deployed in side arms (TJSE is not used in this manuscript). TJSW was discontinued on July 02, 2017. Due to bridge construction, the e1 sensor was moved approximately 50 meters downstream October 29, 2015 and was located about 0.75 m higher in the water column from October 29, 2015 to February 27, 2017. All data from e1mid will be analyzed as a mid-water column instrument. The absolute elevation of e1 was obtained with a Spectra Precision Epoch 50. Water elevations at e1 were corrected with atmospheric pressure at SIO Pier or Los Peñasquitos when available. During 2 ~1 month gaps in the water elevation time series at e1 (September 2015 and March 2017) water levels were supplemented with pressure measurements from the ADCP corrected with atmospheric pressure at SIO Pier. All data was interpolated to 10-minute data.

2.1.2.3 Wave Measurements

During each winter (approximately November through late March/early April) two buried Paroscientific, Inc. pressure sensors were deployed just offshore (in the surfzone, szP) and just inside of the inlet (eP) . Sensors were buried approximately 1 m under the sand, although sediment accreted and eroded throughout the deployment period. Sensor locations varied

slightly year to year due to a mobile cobble layer and the ease of jetting the sensor into the sand. In February 2016 and January 2017 sand at szP eroded more than about half a meter, and thus the sensor was relocated for safety of public. eP was moved once on March 17, 2017 when accretion exceeded one meter causing the sensor to no longer be in direct wave action. The pressure sensors sampled at 2 Hz continuously for 59.73 minutes each hour. szP and eP pressure measurements were corrected to account for frequency attenuation effects due to burial (Raubenheimer et al., 1998).

An acoustic Doppler velocimeter (ADV) was deployed just offshore of the LPL inlet in ~9 m water depth at oADV. The upward facing ADV sampled velocity and pressure at 2 Hz at 0.5 to 0.9 m above the sand bed. A 2 Hz pressure sensor stationed at Scripps Institution of Oceanography, approximately 7.5 km south of the LPL inlet, was used to remove the barometric pressure from szP, eP, and oADV.

Variance preserving spectra were computed for 30 minute windows every 15 minutes from the pressure signals at oADV, szP, eP, and e2ADCP. Each 30-minute window was divided into 11 segments with 75% overlap. Significant wave heights for the swell and infragravity bands (H_{IG} and H_{SW}) were calculated according to $H = 4 * \sqrt{\int_{f1}^{f2} \text{Energy df}}$ where $f_1 = .167$ Hz, $f_2 = .04$ Hz, (6 to 25 sec periods) for swell energy, and $f_1 = .04$ Hz, $f_2 = .004$ Hz (25 to 250 sec periods) for infragravity wave energy .

A downward facing ADV sampling at 8 Hz at a height of 0.28 m above the bed with an attached optical backscatter sensor sampling at 0.67 m above the bed was deployed for 1 day on January 22, 2016 near the estuary mouth (eADV) .

2.1.2.4 Meteorological Measurements

Earth Networks, Inc. provided barometric pressure, precipitation, air temperature, and wind data from Scripps Pier approximately 7.5 km south. Long-term records of precipitation were obtained from the National Climatic Data Center (NCDC) Station USW0023188 at San Diego Airport 26 km south of LPL.

2.1.2.5 Bathymetry

Bathymetric data was collected in transects using a downward-looking, towed ADCP (see Figure 2.1). The depth was converted into absolute elevation by subtracting the surveyed water level sensor. Upstream of the railroad bridge bathymetric transects were collected on January 11, 2015, January 12, 2016, January 29, 2016, and February 08, 2016. Downstream of the Bridge bathymetric transects were collected on February 23, 2017, and March 06, 2016. Additionally, depth measurements using depth from occasional CTD casts were incorporated for depths in the channel. Elevation of the shallower regions near the mouth are from drone data converted into elevation with structure-from-motion software (Pix4D). The composite bathymetric picture (Figure 2.1) shows a relatively uniform, shallow channel which decreases in depth upstream with a sill near the mouth and two deeper holes near the outside of the two sharpest bends. The sill elevation is defined as the lower-low water level at e1 (Harvey et al. 2019).

2.1.2.6 Additional measurements

Ocean (o) water level, temperature, and salinity at Scripps Pier were extracted from the Southern California Coastal Ocean Observing System (SCCOOS, sccoos.org). Offshore wave data (significant wave height, H_{sig}; peak period, T; and peak direction) was extracted from the Coastal Data Information Program (CDIP, cdip.ucsd.edu) Torrey Pines Outer Buoy 100, 12 km west (offshore) of the inlet.

River flow rates are from United States Geological Survey (USGS) Los Peñasquitos Creek Gauge 11023340. Elwany (2011) calculated that the continuous Los Peñasquitos Creek USGS gauge accounts for 85% of the inflow, thus the USGS reported values are multiplied by 118% to approximate the total river inflow.

A time-lapse camera taking photos of the inlet area during daylight every 15 minutes was deployed near the mouth by the TRNERR SWMP.

2.1.3 Analysis Methods

2.1.3.1 Removal of Tides

Tidal velocities were lowpass filtered using a Godin filter (Walters & Heston, 1982) to remove the tides. Data that has been Godin-filtered is denoted with a subscript G.

2.1.3.2 Empirical Orthogonal Functions

Singular value decomposition (SVD) (Thomson & Emery, 2014) of the low-passed velocities was used to calculate the first three empirical orthogonal function modes (EOF1, EOF2, and EOF3).

2.1.3.3 Asymmetry

Asymmetry can be an important parameter for sediment transport into or out of an inlet. The asymmetry can be defined in several ways including inlet asymmetry, and tidal asymmetry. Skewness is generally defined as the third central moment about the mean (Thomson & Emery, 2014). Nidzieko (2010) defines the normalized skewness, γ, as the third moment about the window mean normalized by the second moment about the window mean to the 3/2 power.

In order to better incorporate sediment transport which is generally proportional to velocity cubed (Bagnold, 1966), Nidzieko & Ralston (2012) define γ_0 as the third sample moment about zero normalized by the second sample moment about zero. To construct a time series, a

running window of 2 times a lunar day (24.84 h) is used where the lunar day starts on an offshore high-high water (HHW). γ_0 was calculated for phase-averaged periods.

$$\gamma_0 \equiv \frac{\mu_3}{\mu_2^{3/2}} = \frac{\frac{1}{\varepsilon-1}\sum_{t=1}^{\varepsilon}(A_t)^3}{\left(\frac{1}{\varepsilon-1}\sum_{t=1}^{\varepsilon}(A_t)^2\right)^{3/2}}$$

For $\gamma_0^{o,\frac{\delta\eta}{\delta t}}$, A is defined as $\frac{\delta\eta_o}{\delta t}$ where η_o is the offshore water level. For $\gamma_0^{e,\frac{\delta\eta}{\delta t}}$, A is defined as $\frac{\delta\eta_e}{\delta t}$ where η_e is the estuary water level. For $\gamma_0^{e,u}$, A is defined as the depth averaged estuary along-stream velocity, $[u]$, (square-brackets indicate depth-averaged).

The tidal asymmetry factor (Friedrichs & Madsen, 1992; Nidzieko, 2010) of the inlet morphology is defined as γ_{Inlet} where,

$$\gamma_{Inlet} = (1+\alpha)\frac{a}{h} - \frac{\bar{b}-B}{\bar{b}}$$

a is the tidal amplitude (i.e., half the tidal range between MHHW and MLLW), h is the mean estuary depth, B is the main channel width (below MLLW), $\bar{b}$ is mean of the total estuary width between MLLW and MHHW, and α is a weighted friction term. B and $\bar{b}$ were approximated with drone imagery and based on distances in the inlet area near the mouth.

2.1.3.4 Phase Averaging

2.1.3.4.1 Tidal Phase Averaging

Various parameters were phase-averaged in order to examine consistently repeatable patterns. All variables were interpolated or bin-averaged to 10-minute data prior to phase averaging. All data was then tidal-phase averaged, fortnightly-phase averaged, and diurnally-phase averaged

Tidal phase averages are between two high-high water (HHW) events in order to capture the mixed semi-diurnal tide. For the phase averages, 0-phase is the offshore HHW water-level and 2π-phase is the following HHW. If there are two HHW events in a row, the segment is ignored. If there is a HHW followed by two HW events, 0-phase is the offshore HHW and 2π-phase is the second HW event. This results in 1796 individual realizations of HHW events during the study period with average length of 24.76 hours. The number of realizations of each variable is dependent on the availability of data as most instruments had data gaps, Table 1.1. If more than 75% of a given tidal cycle is missing data, that tidal cycle was ignored and not included in the average.

The tidal averages were performed for three separate inlet states: open, constricted, and closed. The open or closed inlet state was determined from estuary water levels and time-lapse camera imagery. Constricted refers to 7 days prior to a mouth closure. For some analyses (as stated below) periods of high river flow (defined as any time 24 hours before or after the stream gauge or the first EOF mode amplitude was in the top 5 percentile of measurements) were removed.

Open period averages were divided into spring and neap periods based on the top and bottom 33.3 percentiles of offshore tidal amplitude range (A) (spring: A> 1.78 m; neap A<1.35 m).

2.1.3.4.2 Phase-averaging Mixing Parameters

The phase-averaged shear squared, $\langle S^2 \rangle_\tau$,is defined as $\langle \frac{\delta u}{\delta z} \rangle_\tau^{\ 2}$, where the angle brackets with a τ indicate tidal phase-averaging. The bulk shear squared, , is defined as $\langle S_T^2 \rangle_\tau = \left(\frac{\langle u_{\sigma=.8} \rangle_\tau - \langle u_{\sigma=.25} \rangle_\tau}{\langle H \rangle_\tau (.8-.25)} \right)^2$ where depth-normalized heights of 0.8 and 0.25 are chosen to avoid the

region of extrapolated ADCP data, and to be approximately consistent with the near bottom and near surface CTD measurements at e1mid used to compute a bulk stratification. The phase-averaged Richardson Number is defined as, $\langle Ri \rangle_\tau = \frac{\langle N^2 \rangle_\tau}{\langle S_T^2 \rangle_\tau}$, (Geyer & MacCready, 2013; MacCready & Geyer, 2010)

2.1.3.4.3 Spring-Neap Phase Averaging

In a similar manner to the tidal phase averaging, variables were phase overaged over a spring neap period. A spring-neap period is defined as half a lunar month (14.77 days). The start of each spring-neap period is defined as a HHW event, and the end of the period is the nearest HHW event 14.77 days after the start of the spring. Angle brackets with a ϕ indicate spring-neap phase averaging, $\langle \quad \rangle_\phi$. Spring-neap cycles of 50% missing data are removed, resulting in 63 realizations for the ADCP data (less for the CTD data which has more bad data).

2.1.3.5 Exchange Velocity

An approximation of the magnitude of the exchange velocity is defined by

$$u_E^{theory} \approx \frac{g H^2 \frac{\Delta \rho}{\Delta X}}{48 \rho_o \sqrt{C_d} U_T}$$

where g is the gravitational acceleration, H is the water depth, $\frac{\Delta \rho}{\Delta X}$ is the longitudinal salt gradient between ρ_{e3mid} and ρ_o, $C_d = 1.0 \times 10^{-3}$, and U_T is the absolute value of the depth averaged velocity at the ADCP, $u_T = |[u]|$ (MacCready & Geyer, 2010). These values are Godin-filtered prior to analysis such that

$$u_E^{theory} \approx \frac{g H_G^2 \frac{\rho_{e3mid,G} - \rho_{o,G}}{\Delta X}}{48 \rho_o \sqrt{C_d} U_{T,G}}.$$

The observed exchange flow is defined as the Godin-filtered velocities minus the 1st mode of the EOF such that $u_E^{obs} = u_G - EOF1$. EOF1 is removed to remove most large river

flow events as described below. The magnitude of the exchange flow is defined as $\left|u_E^{obs}\right| = u_E^{obs}(\sigma_{max}) - u_E^{obs}(\sigma_{min})$. If σ_{max} or σ_{min} are above or below the interpolated locations, the last measured bin was used. The sign of $\left|u_E^{obs}\right|$ is negative if the outflow is below the inflow (i.e., inverse estuarine exchange flow).

2.2 Results

2.2.1 Overview of Long-term Circulation

The first 3 EOF modes of the 1-hour interpolated residual velocities for all open and closed periods transformed explain 94.0%, 5.1%, and 0.01% of the variance, respectively. The first mode is barotropic and correlates with river flow with the strongest correlation with EOF mode 1 lagged 7 hours behind the river flow ($r = 0.68$, $p<0.001$). The 2nd mode is baroclinic in vertical structure and correlates well ($r = 0.89$, $p<0.001$) with the difference between u_G at $\sigma = 0.8$ and $\sigma = 0.25$. The second mode is positive (indicating velocities are out at the surface, in at depth, i.e., a canonical estuarine circulation) 91.7% of the time when the estuary is open. The 2nd baroclinic mode also correlates well with the magnitude of the exchange flow, $\left|u_E^{obs}\right|$ ($r = 0.91$, $p<0.001$).

2.2.2 Wave Field Offshore and in the Estuary

Wave energy was measured at 4 locations from offshore to upstream: oADV, szP, eP, and e2. The peak period of the energy offshore varies with longer period waves (shorter frequency) arriving in sets before shorter period waves (higher frequency) (Figure 2.3a). Most of the energy in the offshore site was in the swell band (Figure 2.3a, Figure 2.4). Moving inshore to szP, there is less energy total and the peak period has increased (Figure 2.3b). At szP the height of the swell waves is much smaller than offshore but the height of the IG waves is larger than offshore (and the largest of the four locations) (Figure 2.4b). Moving into the inlet, the amount of

wave energy is dependent on the wave height offshore, the tidal height and velocity (the banded nature of Figure 2.4c), and the sill height. When the waves offshore are large, and the sill is lower IG waves are able to make it up to the ADCP at e2, 0.75 km upstream. The highest percentage of total energy in the IG band is found at eP during flooding tides (Figure 2.4c, red dot at eP). The IG percent of total energy at e2 is also high but slightly smaller, potentially because of the higher noise floor of the instrumentation.

Wave-current interaction can impede or facilitate wave energy from entering the inlet as flooding tides enable waves to propagate further into the estuary while stronger ebb tides can impede waves entering the system (Figure 2.5). For example, as the magnitude of outflowing velocity decrease at eADV (Figure 2.5a) and the water levels start to increase within the estuary (Figure 2.5b) some small waves pass over the sensor at eP (Figure 2.5c, blue). When the velocity switches sign at eADV (Figure 2.5a), the waves are able to propagate further (Figure 2.5c, pink). The waves reach the furthest distance upstream (Figure 2.5c, green) during inflowing velocities when the tide is highest (Figure 2.5b) and the largest waves are able to enter the system. During the inflowing tide, the dissipating waves are transporting suspended sediment as measured by the voltage from the OBS signal (Figure 2.5d). As the velocities reduce, so too does the amount of sediment transported into the system.

2.2.3 2xM_2 Circulation during Open, Constricted, and Closed Periods

2.2.3.1.1 Open

To examine the mixed semi-diurnal tide with the larger and smaller tides explicitly, a phase average (see section 3.3.5) of a lunar day or $2 \times M_2$ is examined. Hereafter, the larger tide will refer to the M_2 tide with the higher depth-averaged velocities (~0 to ~π, Figure 2.6f) and

the smaller tide will refer to tide with the lower depth-averaged velocities ($\sim\pi\ to\ \sim 2\pi$, Figure 2.6f).

During open periods, the phase-averaged offshore tide, $\langle \eta_o \rangle_\tau$, has a range of 1.54 m between HHW and LLW while $\langle \eta_e \rangle_\tau$ has a range of 0.75 m between HHW and LLW (Figure 2.6 a.i.). The HHW in the estuary is lagged 0.66 hours behind the tide offshore (measured 7.5 miles from the mouth) while the LLW in the lagoon is lagged 2.32 hours behind the LLW in the offshore. The normalized skewness about zero of the rate of change of the offshore water level is below zero while positive in the estuary ($\gamma_0^{o,\langle \frac{\delta \eta}{\delta t} \rangle_\tau} = -0.15;\ \gamma_0^{e,\langle \frac{\delta \eta}{\delta t} \rangle_\tau} = 0.60$) indicating that the duration of the falling tide in the estuary is longer than the rising tide and is significantly different from the nearly symmetrical offshore water level asymmetry (Nidzieko & Ralston, 2012).

Near-bottom estuarine density, $\langle \rho_{e2,bot} \rangle_\tau$, is slightly less dense than offshore, $\langle \rho_o \rangle_\tau$ (Figure 2.6 b.i). Near-surface estuarine density, $\langle \rho_{e2,top} \rangle_\tau$, is the least dense near the end of the larger flood tide and densest at the end of the smaller ebb tide. This results in maximum bulk stratification ($N^2 = 0.034\ s^{-2}$) near the end of the smaller ebb tide and minimum bulk stratification ($N^2 = 0.010\ s^{-2}$) near the end of the larger flood (Figure 2.6 b.i.). $\langle DO_{e2,bot} \rangle_\tau$ generally, has lower dissolved oxygen concentrations than $\langle DO_{e1mid} \rangle_\tau$ higher up in the water column. Additionally, $\langle DO_{e1} \rangle_\tau$ is more variable throughout the tidal cycle (Figure 2.6 c.i.), potentially due to both its height in the water column and longitudinal location closer to the estuary mouth.

Depth, phase-averaged velocity, $\langle [u] \rangle_\tau$, ranges from -0.07 to 0.09 $m \cdot s^{-1}$. The ebb tide is slower yet longer in duration ($\langle [u] \rangle_\tau$ is in the ebb direction 57% of the time). The normalized skewness of about zero of the velocity ($\gamma_0^{e,\langle [u] \rangle_\tau} = 0.66$) indicates flood-dominance. The

maximum velocity during the flood tide is mid-depth (σ=0.65) while the maximum velocity during the ebb tide is closer to the surface (σ= 0.85) (Figure 2.6 f.i.). The velocity is more depth-uniform during flood tides than ebb tides leading to higher mid-water column shear during ebb tides (Figure 2.6 g.i). Shear near the bottom is highest during flood tides and larger ebb tides. Note that hatched areas in Figure 2.6 f-g indicate the phase-averaged location of extrapolated data.

As shown with the short time-series described in section 4.2, tidal phase averages confirm that wave energy just inside the inlet (measured at eP) is dependent on the tidal amplitude as well as the magnitude and direction of velocity. Wave energy is larger during flooding tides and when the offshore water level is higher (Figure 2.3; Figure 2.6 e.i.). During the larger flooding tide and into the maximum high tide, the wave energy is greatest with the highest frequency of waves able to propagate into the mouth. Wave energy is lowest (and in lower frequencies) during the latter part of the larger ebb tide when the velocities are out of the estuary and the water level offshore is low.

The turbidity generally increases during the flood tide (Figure 2.6 d.i.). The turbidity correlates with the depth-averaged velocity (r = 0.73, p =.002); however, the turbidity signal is very noisy with the standard deviation over 2.8 times the range of the phase-averaged turbidity signal.

2.2.3.1.2 Constricted

During constricted periods (defined as 7 days before a closure), $\langle \eta_e \rangle_\tau$ decreases to 0.36 m between HHW and LLW while the asymmetry increases, $\gamma_0^{e,\langle \frac{\delta \eta}{\delta t} \rangle_\tau} = 1.01$ (Figure 2.6 a.ii.). The density of the surface water is generally slightly fresher and fluctuates less throughout a tidal cycle than during the open period, resulting in net higher stratification. The lowest stratification

still occurs during the high tide and the highest stratification remains at the end of the smaller ebb tide / start of the large flood tide (Figure 2.6 b.ii.).

The maximum value of $\langle [u] \rangle_\tau$ has decreased to 0.06 m·s^{-1} during the flood and -0.03 m·s^{-1} during the ebb tide. The normalized velocity skewness about zero ($\gamma_0^{e,\langle [u] \rangle_\tau} = 1.64$) indicates even stronger flood-dominance than during the open state. During the constricted period, nearly the entire ebb is constrained above the mid-water column depth while the bottom water is moving in the upstream direction (Figure 2.6 f.ii.) leading to increased mid-water column shear during the ebbs (Figure 2.6 g.ii). Because of overall reduced velocities, the lower water column is less sheared than during the during the open phase (Figure 2.6 g.ii.).

During the constricted period, the maximum phase-averaged total wave energy is 2.42 times the amount of energy during the flood tide of the open period. There is very little wave energy during the ebbing tide near offshore low water levels because the combined wave swash elevation and offshore water level are not large enough to exceed the sill height Figure 2.5 6.ii.).

2.2.3.1.3 Closed

During closed periods, $\langle \eta_e \rangle_\tau$ does not vary with the offshore tidal phase and is consistently elevated above $\langle \eta_o \rangle_\tau$. The densities at all locations in the estuary are fresher than during either the constricted or open periods. $\langle [u] \rangle_\tau$ are very small (<0.004m/s). The apparent tidal modulation of the velocities may be diurnal velocities leaking into the 24.84 hour tidal phase average. During the closed phase, waves occasionally overtop this sill at offshore high tide resulting in some wave energy propagating into the inlet. The wave energy able to make it over the sill is primarily in the IG band with more energy able to propagate in during the higher offshore high water levels.

2.2.4 Circulation during Spring and Neap Periods

During spring tides, $\langle \eta_e \rangle_\tau$ has a larger maximum tidal range than during neap tides (0.97 m and 0.52 m between HHW and LLW, for spring and neap tides respectively) (Figure 2.7 a. i,ii.), directly related to the method by which spring and neap tides are defined based on the offshore water level amplitudes as explained in section 2.1.3.4.1. The skewness of the rate of change of the water level is similar within the lagoon as well as offshore between the spring and neap, $\gamma_0^{e,\langle \frac{\delta \eta}{\delta t} \rangle_\tau} = 0.65 \; and \; 0.57$; $\gamma_0^{o,\langle \frac{\delta \eta}{\delta t} \rangle_\tau} = -0.19 \; and$ -0.05 for spring and neap, respectively). The skewness of the velocity, however, is much larger during the neap tides ($\gamma_0^{e,\langle [u] \rangle_\tau} = 0.41 \; and \; 1.20$, for spring and neap, respectively). $\langle [u] \rangle_\tau$ during the spring tides is much larger (~3 times) than during neap tides. Velocities extend deeper into the water column during spring tides (Figure 2.7f). Shear, both $\langle S^2 \rangle_\tau$ and $\langle S_T^2 \rangle_\tau$, is slightly larger during the spring tides, whereas $\langle N^2 \rangle_\tau$ is higher during the neap tides (Figure 2.6 b. i,ii. And 4.e.). The combination of higher $\langle S^2 \rangle_\tau$ and lower $\langle N^2 \rangle_\tau$ results in lower phase-averaged bulk Richardson numbers, $\langle Ri \rangle_\tau$ during the spring tides. The lowest $\langle Ri \rangle_\tau$ occurs during the larger ebb spring tide $\langle Ri \rangle_\tau = 2.42$.

When the Godin-filtered data is phase averaged based on a spring-neap cycle (Section 3.3.4.2) during the open, low river flow periods, the estuary water level range (higher-high minus lower-lower) exhibits a smaller variation than the offshore range (Figure 2.8 a.). The $\langle sill \; elevation \rangle_\phi$ does not exhibit a clear spring-neap cycle as it has a very large standard deviation, however the majority of the mouth closures occur during the neap tide (red lines, Figure 2.8a). The vertical stratification, $\langle N^2 \rangle_\phi$ (Figure 2.8d) and the along-channel density gradient, $\left\langle \frac{\rho_{e3,G} - \rho_{o,G}}{\Delta X} \right\rangle_\phi$ are maximum during neap tides. The theoretical estuarine exchange flow, $\left\langle \mathrm{u_E^{theory}} \right\rangle_\phi$ (Figure 2.8b) is a maximum during neap tide and a minimum during spring tide.

However, the observed exchange flow $\langle u_E^{obs} \rangle_\phi$ for the entire open time period (except during extreme river flows), is a maximum at the end of the spring tide (Figure 2.8c). Furthermore, the magnitude of the calculated exchange flow is greater than that predicted by theory (Figure 2.8b). When the exchange is calculated only during the lowest sill elevations (sill below 0.69 m, NAVD88, lowest 1/3 of sill height measurements, and also restricting to open, non-extreme river flows), the strength of the exchange increased from spring, to between spring and neap, to a maximum during the neaps (Figure 2.9). When the sill was high (above 0.89 m, NAVD88, highest 1/3 of sill height measurements), the strength of the exchange was greatest during spring and between spring and neap and lowest during the neap tide.

2.3 Discussion

2.3.1 Interannual Variability of Atmospheric and Wave Forcing

The objective of this paper was to understand how the dynamics of a small, shallow, bar-built estuary change over various time scales including tidal, diurnal, spring-neap, seasonal, and interannual. Over the period of data collection, December 2014 – May 2019, several distinct large-scale oceanic and atmospheric forcing events occurred including the Blob, a large El Niño, and anomalously wet and dry years. This interannual variability impacted both upstream (with fluctuating river flows) and downstream of the estuary (with varying wave conditions and offshore water levels). River discharge can affect the degree of stratification and strength of the tidal and residual circulation in the estuary directly (e.g., (Geyer & MacCready, 2013; Hansen & Rattray, 1966); while both the amount of river flow and the offshore water levels and wave energy affect the sill height (Behrens et al., 2013; Rich & Keller, 2013), which has impacts on the circulation, sediment transport, and mixing near the inlet (Behrens et al., 2016; Cousins et al., 2010; Gale et al., 2007; JL Largier et al., 1992).

The 2014-2015 Blob resulted in small waves, high air and sea surface temperatures, high atmospheric pressure (Bond et al., 2015; Hartmann, 2015) and small river flows (Figure 2.2f). During the summer and early fall weak and sometimes negative exchange occurred (negative exchange 32.6% of the time from June 01 2015 to Sept 30 2015, Figure 2.2b), hypothesized due to weaker along-stream density gradients. The side estuary arm that has a smaller watershed went hypersaline during these periods as evidenced from comparing the salinity at TJSW to offshore salinity (not shown here).

The 2015-2016 El Niño brought extremely large waves and slightly below average precipitation (Barnard et al., 2017; Siler et al., 2017; Young et al., 2018). The large waves and lack of river flows (Figure 2.2f) during the El Niño caused significant accretion to estuarine inlets all along the Southern California Bight (Harvey et al., 2019; Young et al., 2018) and increased estuarine inundation (Harvey et al., 2019; Goodman et al., 2018). In LPL, the anomalously strong wave conditions and weak precipitation (thus small river flow) contributed to 2016 having a total of 235 closed days, far exceeding than the annual average (excluding 2016) of 42 closed days since 2004.

The 2016-2017 winter was an anomalously wet winter (precipitation at San Diego Airport was 41% above the 1939-2019 winter average) with large river flows and large waves. The largest river flow event of the study period occurred in the last week of February 2017 which resulted in extremely high velocities ($|u|$ = 2.00 m/s) at e2. The large velocities scoured the sill causing the lowest sill elevation for the study period (~ -0.1m NAVD88). The large scouring from the rainfall event may have contributed to the lower sill elevations and more symmetric water levels and velocities the following summer and fall.

2017-2018 winter was extremely dry with low river flows and small waves (winter precipitation at San Diego Airport was in the bottom 5 percentile, 61% below 1939-2019 winter average). The sill elevations during the 2018 spring were fairly high resulting in higher asymmetries in the water levels and velocities (Figure 2.1c). The 2018-2019 winter had moderate waves and high precipitation (precipitation at San Diego Airport 37% above 1939-209 average) and river flows. The sill was scoured to its second lowest level during the study period in February 2019.

This interannual variability in waves and precipitation (i.e., river flows) results in changes to sill height. As described below, the sill height can affect the tidal circulation, residual circulation, and the amount of wave energy in the system.

2.3.2 Drivers of Inlet Accretion and Erosion

2.3.2.1 River Discharge

River discharge is one of the main drivers of inlet erosion (Behrens et al., 2013; Ranasinghe et al., 1999; Rich & Keller, 2013). Following large discharge events, the sill was generally low (Figure 2.1a and 1f) with the lowest sill observed after the largest river discharge event. During particularly dry periods the sill steadily grew (2017-2018).

2.3.2.2 Tidal Asymmetry

Despite asymmetry indicating an ebb-dominant tide offshore (Nidzieko, 2010) ($average\ \gamma_0^{o,\frac{\delta\eta}{\delta t}} = -0.13$ during the study period) the asymmetry for both water level and tidal velocities within the estuary are indicative of a flood-dominant system (average $\gamma_0^{e,\frac{\delta\eta}{\delta t}} = 0.99;\ \gamma_0^{e,u} = 0.76\ during\ the\ study\ period$) and thus the bed-load sediment transport of coarse sediments is directed into the inlet (Dronkers, 1986). Additionally, the mouth geometry

itself is positive (γ_{inlet} = 0.80), also indicative of a flood-dominant system (Friedrichs & Madsen, 1992; Nidzieko, 2010). Interestingly, the phase-averaged tidal, $\gamma_0^{e,\langle\frac{\delta\eta}{\delta t}\rangle_\tau}$ and $\gamma_0^{o,\langle\frac{\delta\eta}{\delta t}\rangle_\tau}$ both showed a slightly reduced magnitude of asymmetry during the neap than spring. When using the velocity to calculate the asymmetry over a phase-averaged tidal period, in the estuary, $\gamma_0^{e,\langle[u]\rangle_\tau}$ becomes more much positive during the neap periods. While the skewness is also dependent on sill height (section 1.4.3.1.2)., as the velocity is responsible for movement of sediment, the more positive (flood-dominant) skewness is likely a contributing factor to that fact that closures are more common during neap tide (Figure 2.8a).

2.3.2.3 Waves

During the study period, the largest offshore waves occurred during the 2015-2016 El Niño winter (Barnard et al., 2017; Young et al., 2018). As estuary and surfzone wave measurements were only taken during the winter months (Figure 2.3) the estuary and surfzone wave energy in Figure 2.3 represents periods of only larger winter offshore waves. The sill is generally higher during the winter months partially due to wave build up, partially due to timing of dredging typically occurring during the spring.

Estuary wave energy is dependent on the magnitude and direction of velocity at the inlet (Figure 2.5), the offshore tidal amplitude, the sill height, and the offshore wave energy (Figure 2.3a). During open periods, wave energy propagates into the estuary on flooding tides when the water level is high offshore (Figure 2.6ei.). The waves bring in beach sand due to a combination of bed load and suspended sediment transport (Figure 2.5d and Figure 2.6dii). During the flood tides there is a stronger signal of turbidity (Figure 2.6di, dii) consistent with both higher near-bed velocities, higher near-bed shear, and larger waves (similar to Bertin et al., 2019). The maximum total wave energy was observed during the constricted phase of the large, flooding tide. These

events occurring in the 7 days preceding closure, likely facilitated the closure. Wave energy was blocked by large ebb currents such that at similar water levels, but with ebbing velocities, waves cannot propagate upstream (Figure 2.6ei and eii) (Bertin et al., 2019; Bertin & Olabarrieta, 2016; Williams & Stacey, 2016). As the waves move onshore, they both transform and dissipate. IG waves are released in the surfzone (Bertin et al., 2018). Moving onshore and upstream, both IG and higher frequency waves dissipate (resulting in a decrease in total energy). The percent of IG energy relative to the total wave energy within the estuary is higher compared with the surfzone and offshore because the sill acts as a low pass filter (Figure 2.4) (Bertin et al., 2019; Bertin & Olabarrieta, 2016; Williams & Stacey, 2016).

Similar to other studies, (Behrens et al., 2013; Ranasinghe et al., 1999; Rich & Keller, 2013) river discharge transports sand out of the inlet of LPL while velocity asymmetry and the propagation of larger waves during flood tides drive sediment transport into the estuary. Despite the erosion caused by the river discharge, there is generally a net accretion in the inlet resulting in inlet closures nearly every year (Figure 2.2a) (Hastings & Elwany, 2012; Young et al., 2018). The accretion can have profound impacts on the tidal and estuarine circulation.

2.3.3 2xM2 Phased Averaged Flows

The bottom water in the estuary is generally slightly less dense than the water offshore (Figure 2.6 b.i.) indicating that the bottom water is subjected to some mixing within the system. Despite the surface sensor being bio-fouled or not working for a large portion of the study period, the good data suggests that the surface water was least dense near the end of the ebb leading to maximum stratification at the end of the ebb/start of the flood as expected by strain-induced periodic stratification (SIPS), (Simpson et al., 1990). Within the spring-neap cycle, the stratification was generally higher during the neap (Figure 2.7 b. i-ii and Figure 2.8d) than the

spring leading to the minimum stratification near the end of the spring stronger flood tides and maximum stratification at the end of the neap weaker ebb tides as expected in a canonical estuary (Geyer & MacCready, 2013). As the estuary started to close (constricted state), the stratification generally increased compared to during the fully open period (Figure 2.6 b.ii. and Figure 2.2 d.).

The velocities are strongest and more depth-uniform during the flood (Figure 2.6 f.i) leading to lower shear within the water column during the flood than the ebb (Figure 2.6 g.i.) when the velocities are more surface intensified, consistent with SIPS. The strongest shears within the water column occur during the strong spring ebb tides, while the strongest near-bottom shear occurs during the strong spring flood tide (Figure 2.6 g i.). During neap tides, the weaker flood tide is deeper in the water column resulting in shear higher in the water column Figure 2.6 g ii.), again consistent with larger canonical estuaries (Geyer & MacCready, 2013).

When calculating a tidally averaged bulk Richardson number based on the density and velocity difference between the near-surface and near-bottom, the Richardson Number is weakest during the strong flood tide suggesting this period is when there is the most potential for mixing. The Richardson number values (2.4 to 22.9 during spring tides and 7.62 to 37.6 during the neap tides) suggest that mixing never occurs, however, note that our bulk method of estimating the Richardson number from mean gradients will bias the values high (e.g., (Geyer & Smith, 1987; Nepf & Geyer, 1996). For example, when the $\langle S^2 \rangle_\tau$, is calculated using maximum and minium values of $\langle u \rangle_\tau$, $\langle Ri \rangle_\tau$ is much lower and it would be expected to be lower in parts of the water column if we had full vertical profiles of both S^2 and N^2.

2.3.4 Exchange Variability

The first three EOF modes (EOF1, EOF2, and EOF3) of the low-pass filtered velocities were computed to examine how the velocity changed over time. The first mode is barotropic in

structure and peaks during periods of high river flow events (r = 0.68, p<0.001, EOF mode 1 lagged behind discharge by 7 hours).

EOF2 is baroclinic (2-layer) and correlates well the exchange velocity magnitude $\left|u_E^{obs}\right|$ (r = 0.91, p<0.001). While theory suggests that the exchange flow increases during periods of large river discharge,

$$u_E^{Theory,Riv} = \frac{2}{3}\left(\frac{\beta g S_0 Q_R}{W}\right)^{1/3}$$

(Chant et al., 2018; Ralston & Geyer, 2019), the $\left|u_E^{obs}\right|$ and $Q_R^{1/3}$ do not significantly correlate (r=0.12, p =0.25), suggesting that LPL's response to river discharge does not behave like a canonical estuary. This is not surprising, and is likely because the river flows are highly episodic and the small watershed results in steep hydrograph and a fast discharge response time. As EOFs are a tool that do not always accurately represent the physics, periods of high river flows (within the top 95%ile of river flows), create anomalous patterns in higher EOF modes. As such for analyses described in this paper, the periods of strongest river flows are ignored.

$\left|u_E^{obs}\right|$ is positive (outflowing velocities at the surface and inflowing velocities at depth) 91.2% of the time during the open state (excluding high river flows) indicating primarily a canonical estuarine circulation (MacCready & Geyer, 2010), unlike the circulation structure expected in an estuary in a Mediterranean climate during summer months (Hearn & Largier, 1997; Largier et al., 2013; Nidzieko & Monismith, 2013). This predominantly canonical circulation is likely the result of increased urban runoff leading to freshwater input year-round (White & Greer, 2006). During periods with a negative 2nd EOF mode (suggesting inverse estuarine exchange flow), the average Godin-filtered density difference between the upstream CTD and the downstream CTD (i.e. the longitudinal density gradient) is weaker, although not

inverse (-2.86 kgm-3), compared to the when the second EOF mode is positive(-3.57 kgm-3) (Figure 2.2d.)

The exchange velocity $\left|u_E^{obs}\right|$ is small ($\overline{\left|u_E^{obs}\right|}$ = 0.015; standard deviation = 0.0184 for open periods without extreme river flow) compared to the range of 0.05 to 0.3 m/s (reported in Geyer, 2010). However, the exchange velocity is larger than that predicted by the theoretical exchange velocity u_E^{theory} (Figure 2.8b), potentially because the stratification in the water column (Figure 2.8d) reduces the mixing term in the denominator (MacCready & Geyer, 2010; Ralston et al., 2008). The predicted theoretical exchange velocity is stronger during neap tides versus spring tides as expected with theory (W. Geyer & Cannon, 1982; MacCready & Geyer, 2010); however, the observed exchange velocity is strongest in between the spring and neap tides for the entire data set. Splitting the dataset between low and high sill conditions helps elucidate the spring/neap response of the observed exchange flow. When the sill is low (i.e., the estuary is less constricted, open dots Figure 2.9) the exchange flows is strongest during neap tide and weakest during the spring tide as theory would suggest (dashed lines Figure 2.8). However, when the sill is high (i.e., the estuary is constricted, closed dots Figure 2.9) the spring and between spring/neap tides exchange flows are strongest while the neap tide exhibits the weakest exchange (solid lines Figure 2.9). This response may be due to hydraulic controls near the sill where, when the sill is very high during ebb tides, only the top portion of the stratified water column flows out of the lagoon (Blanton et al., 2000; Seim & Gregg, 1997), with stronger outflows during the spring tides. In addition, if during higher sill conditions the flooding tide enters the system more like a density current (John L Largier et al., 1997, 2013; Nidzieko & Monismith, 2013) the net effect of stronger inflows along the bottom and outflows only along the surface during spring tides and overall weaker inflow and outflows during neap tides could contribute to the net higher

exchange flow during the spring tides than the neap tides. However, a lack of velocity and density observations near the sill limits our ability to fully understand the interplay of mechanisms between sill height and spring/neap tidal conditions that impact the estuarine exchange flow strength. This is an area that needs to be addressed with future observations or a numerical model as the exchange flow is important for the residence time, dispersal of larvae, and mixing of pollutants.

2.4 Conclusions

4.5 years of observations from Los Peñasquitos Lagoon show that the hydrodynamics have interannual, seasonal, fortnightly, and tidal variability. While this system would historically have functioned more like a primarily open, low-inflow estuary with periodic inverse circulation structures; development in and around the watershed has prevented it from going inverse (except during periods of extreme drought) and has encouraged sill growth and closures. When the sill near the mouth is low, the estuary functions, in many ways, like a larger, canonical estuary with evidence of strain-induced period stratification and a canonical exchange flow that is larger during neap tides. However, a combination of flood dominance and wave-induced sediment transport contribute to inlet accretion and sill growth. As the sill grows, the estuarine exchange strengthens, particularity during spring tides, thereby departing from canonical estuarine theory. These systems are ubiquitous around the world in Mediterranean climates, so continued observation of them is necessary to understand how the dynamics compare to canonical estuaries and how they might be expected to change under future climate conditions.

2.5 Figures

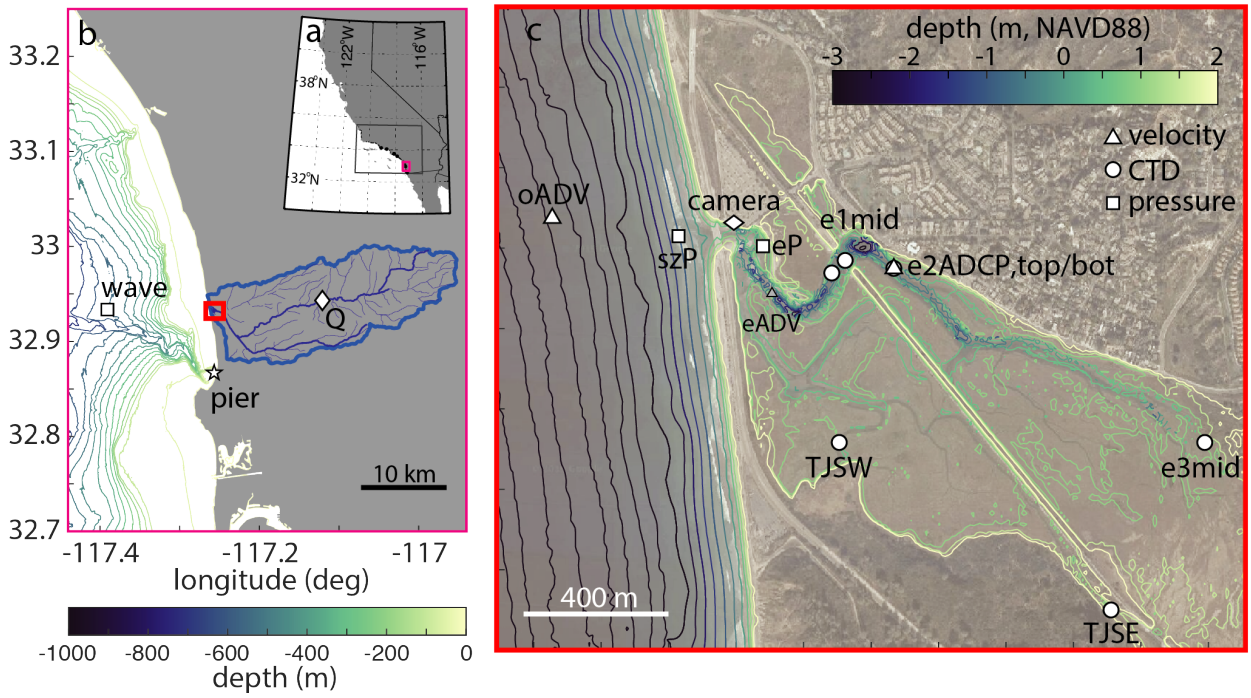

Figure 2.1: Location of Los Peñasquitos Lagoon and instruments deployed. a.) California coastline with San Diego delineated. b.) San Diego coastline with watershed of Los Peñasquitos Lagoon and offshore bathymetry. USGS river gauge noted as Q; SIO Pier denoted as pier; CDIP Buoy 100 denoted as wave. c.) Image of Los Peñasquitos Lagoon with instrument locations (white for nearly continuous measurements, gray for short-term deployments) overlain on marsh topography and bathymetry in teal (light colors are higher elevation). Estuary bathymetry was collected from a combination of UAV measurements and towed ADCP measurements, while those offshore are from the 1/3 arc-second San Diego Coastal DEM model from NOAA and all are referenced to NAVD88.

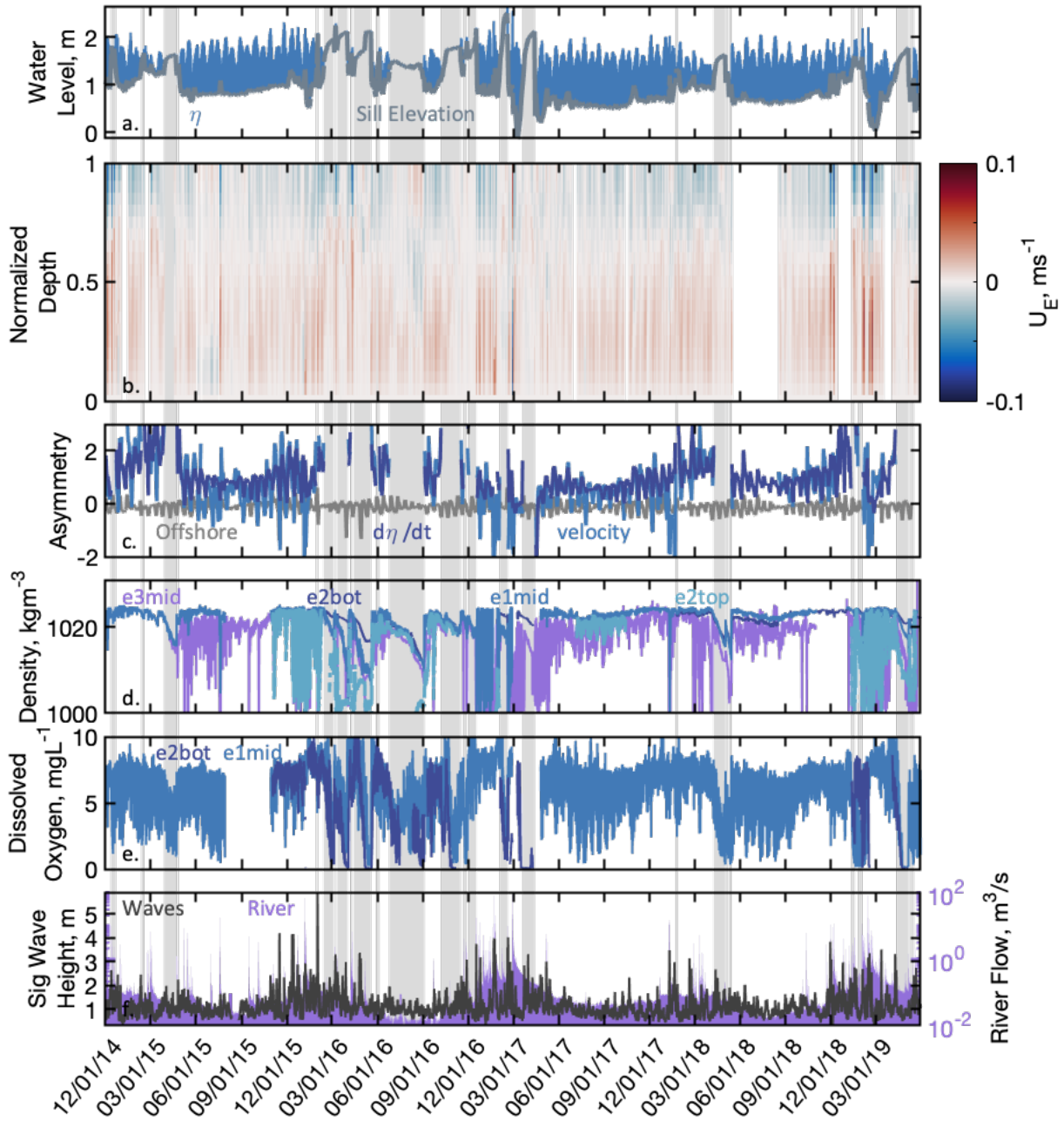

Figure 2.2: Los Peñasquitos Data from December 01, 2014 to May 31, 2019. Gray vertical bars indicate periods of inlet closure. a.) Water level (m, NAVD88, dark blue) and lower-lower water level (m, NAVD88 gray). b.) Exchange velocity defined as the Godin-filtered velocity minus the EOF mode 1 velocity (m/s) d. c.) Water level ($\gamma_0^{o,\frac{\delta\eta}{\delta t}}$ gray; $\gamma_0^{e,\frac{\delta\eta}{\delta t}}$, dark blue) and velocity ($\gamma_0^{e,u}$, medium blue) asymmetry in the estuary and offshore. Asymmetry in the lagoon is not calculated during periods of closure d.) Density at e2top (light blue), e1mid (medium blue), e2bot (dark blue) and e3mid (purple) locations. e.) Dissolved oxygen at e2bot (dark blue) and e1mid (medium blue) sensors. f.) Significant wave height from Torrey Pines Outer Buoy (black, Buoy #100) and river flow (purple, USGS gauge 11023340) .

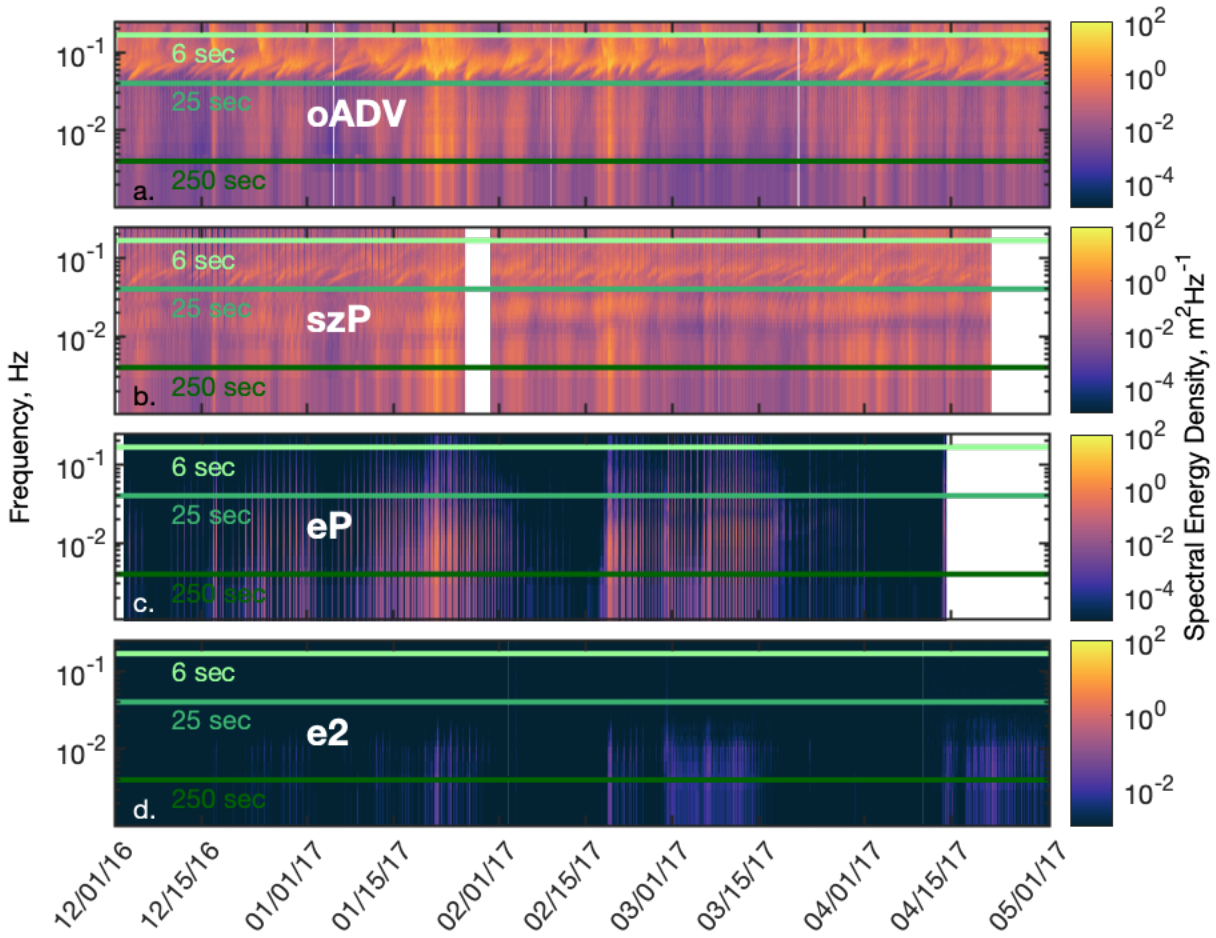

Figure 2.3: Spectrograms of 30-minute segments of wave energy from offshore (a, oADV); to the surfzone (b. szP); into the estuary (c. eP); and upstream (d. e2 ADCP). Horizontal light green line indicates a period of 6 seconds, medium green line is 25 seconds, dark green line is 300 seconds periods for reference. Yellow indicates more energy while dark purple indicates less. Note that the colorbar for e2 (d) is reduced because there was much less energy at e2.

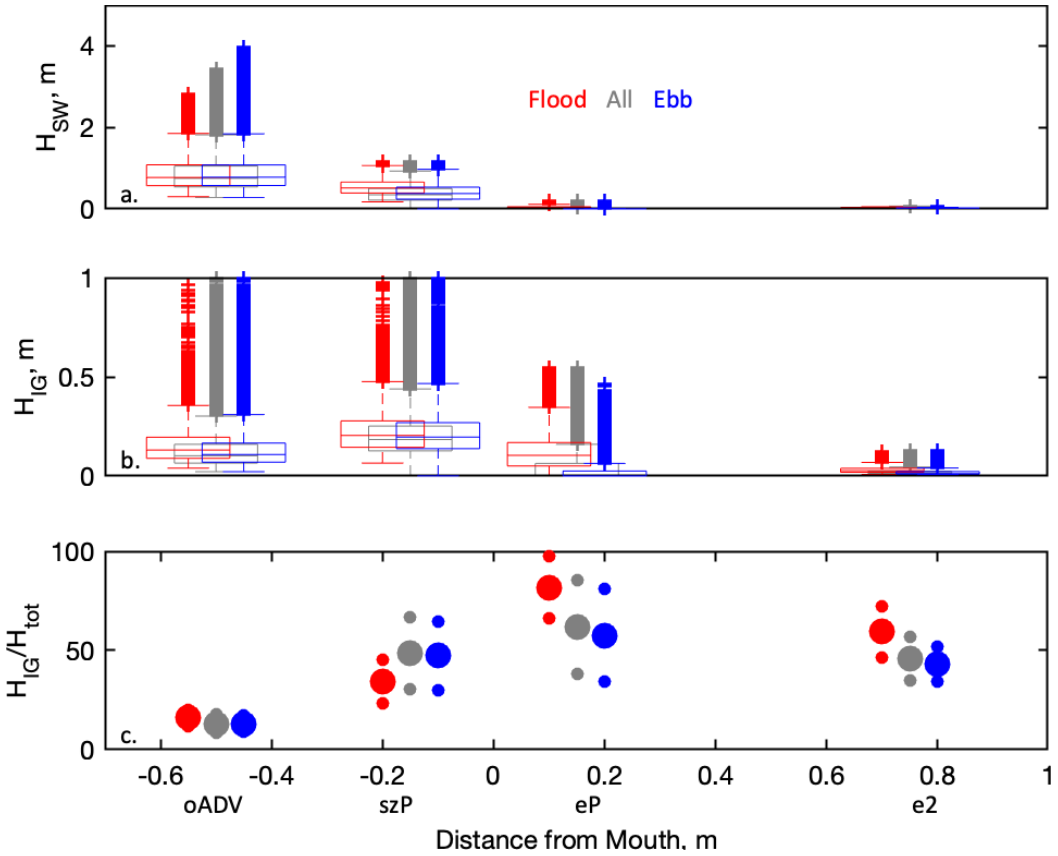

Figure 2.4: Wave Data Summary. Significant wave height box plots of swell (a.) and IG (b.) energy bands measured in 8 m of water (oADV, 0.5 km offshore), the surfzone (szP, 0.15 km offshore), the inlet (eP, 0.15 km upstream), and upstream (LPL1, 0.75 km upstream). Gray indicates all open periods, red indicates flooding periods only, blue indicates ebbing periods only as measured by the velocity direction at the upstream ADCP. The boxes mark the 25th, 50th and 75th percentiles where the outliers, defined by 1.5 times the interquartile range, are marked by + symbols. c.) Percent of IG significant wave height vs total spectrum wave height. The large dots are the mean, the smaller dots indicate +/- one standard deviation. The ADCP pressure sensor error was larger and the sampling interval longer which may have artificially increased the amount of total wave energy resulting in a lower HIG/Htot value.

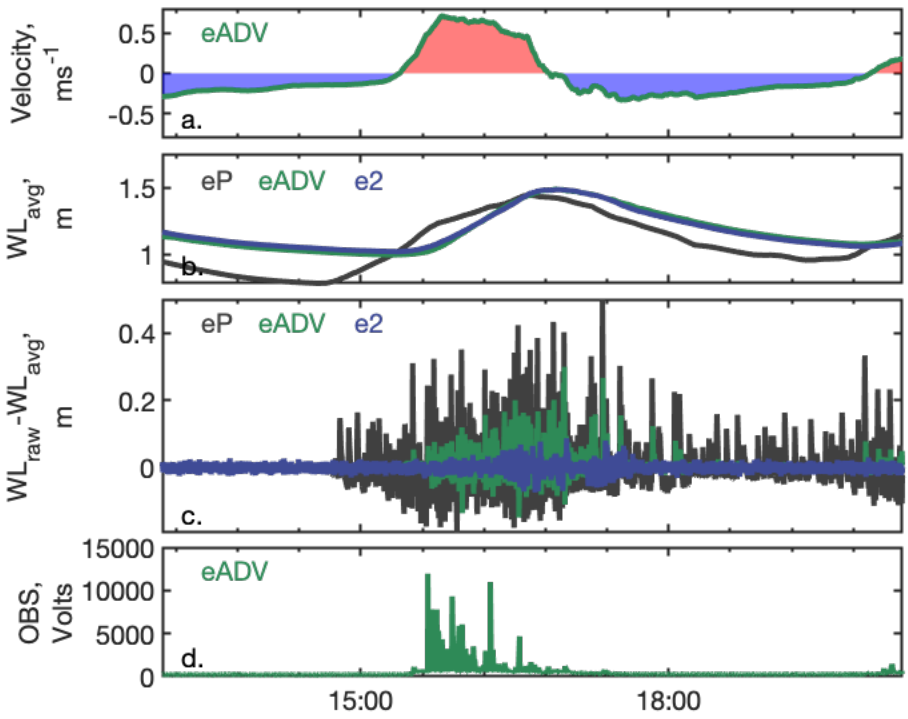

Figure 2.5: Snapshot of wave-current interactions. a.) 30-min average velocity data at ADV ~.4 km upstream (eADV). Blue (red) fill indicates outflowing (inflowing) velocity at eADV. b.) 30-minute averaged water level at eP (gray), eADV (green), and e2 (dark blue). c.) Raw water level minus 30-minute averaged water level at eP, eADV, and e2. eP sampled at 2 Hz; eADV sampled at 8 Hz; e2 sampled at 0.5 Hz. d.) Turbidity from optical back scatter sensor in un-calibrated voltage. Deployment occurred during the low through the lower-high and subsequent low. The sill was about 1.01 m high during this deployment.

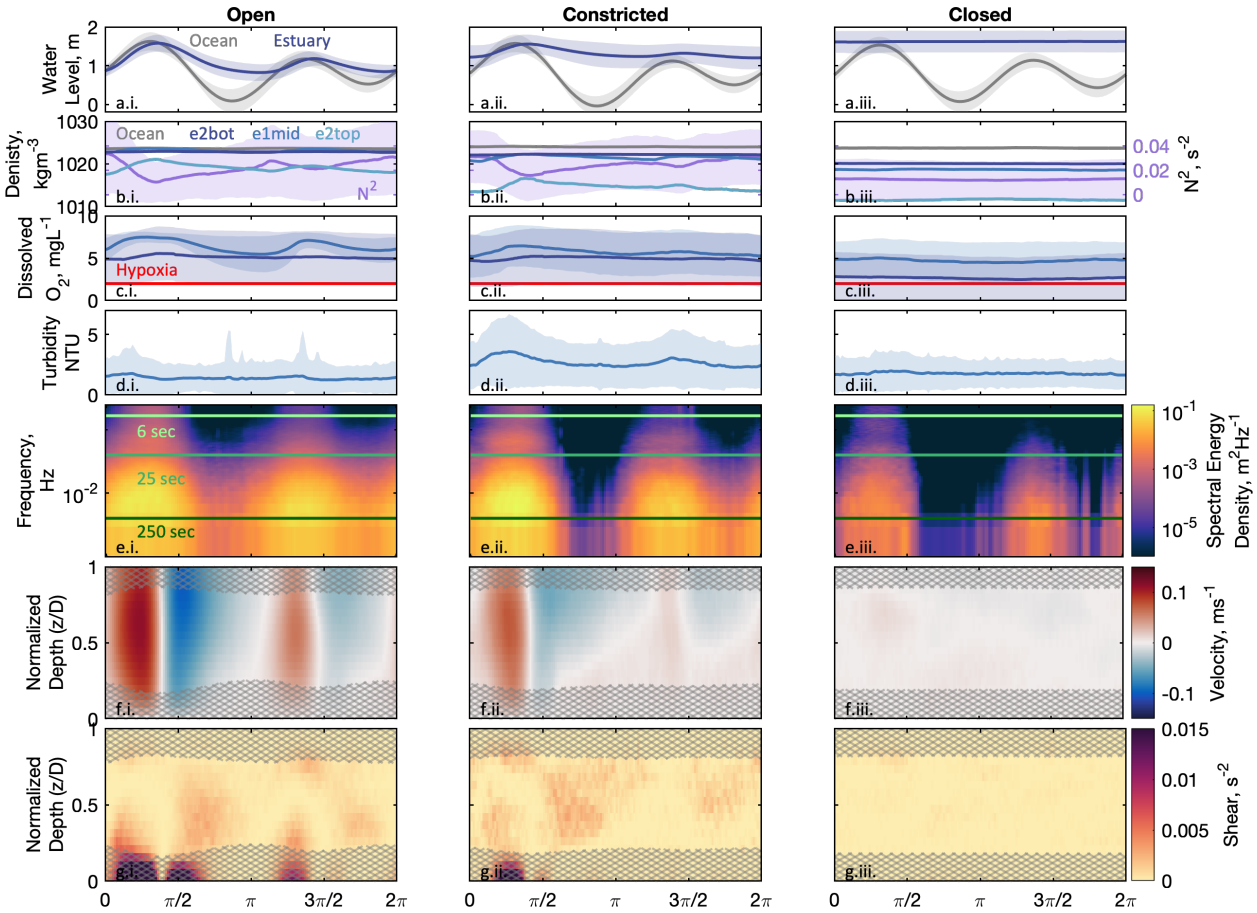

Figure 2.6**:** Tidal phase averages (2xM2) for open periods (i.), constricted periods (ii., defined as one week before closure), and closed periods (iii.). 0 and 2π correspond to the estuary low tides preceding the higher-high. a.) Water level offshore (gray) and in the estuary (blue) in NAVD88. b.) Density offshore (gray), at the e2bot (dark blue), e1mid (medium blue), and at the e2top (light blue). Stratification (purple) based on e2bot and e2top density and water depth (note: number of samples for e2top density and stratification are reduced.). c.) Dissolved oxygen at the e2bot (dark blue) and e1mid (medium blue) where a red line indicates hypoxia. d.) Turbidity at e1mid. Prior to phase averaging, the spikes in the turbidity signal were maxed at 100. Shading on a, b (N^2 only), c, and d indicates +/- one standard deviation of phase average. e.) Wave energy at eP, where yellow indicates more energy. Light green line indicates a period of 6 seconds, medium green line is 25 seconds, dark green line is 300 seconds. f.) Along-stream velocity at e2 in depth-normalized coordinates. Red indicates positive velocities into the lagoon (i.e., flooding), blue indicates negative velocities out of the lagoon (i.e., ebbing). Gray hatching indicates phase averaged region of extrapolated data. g.) Shear throughout the water column calculated from the phase average of velocity differences.

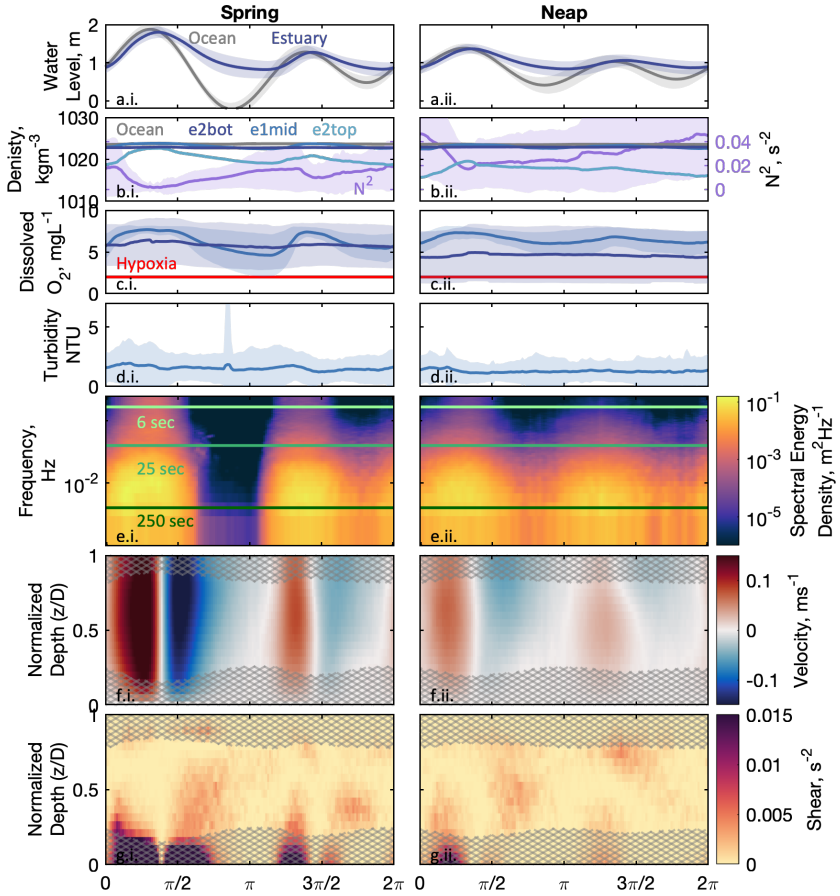

Figure 2.7: Tidal phase averages (2xM2) for for spring (i.) and neap (ii.) periods. Same as Figure 2.6

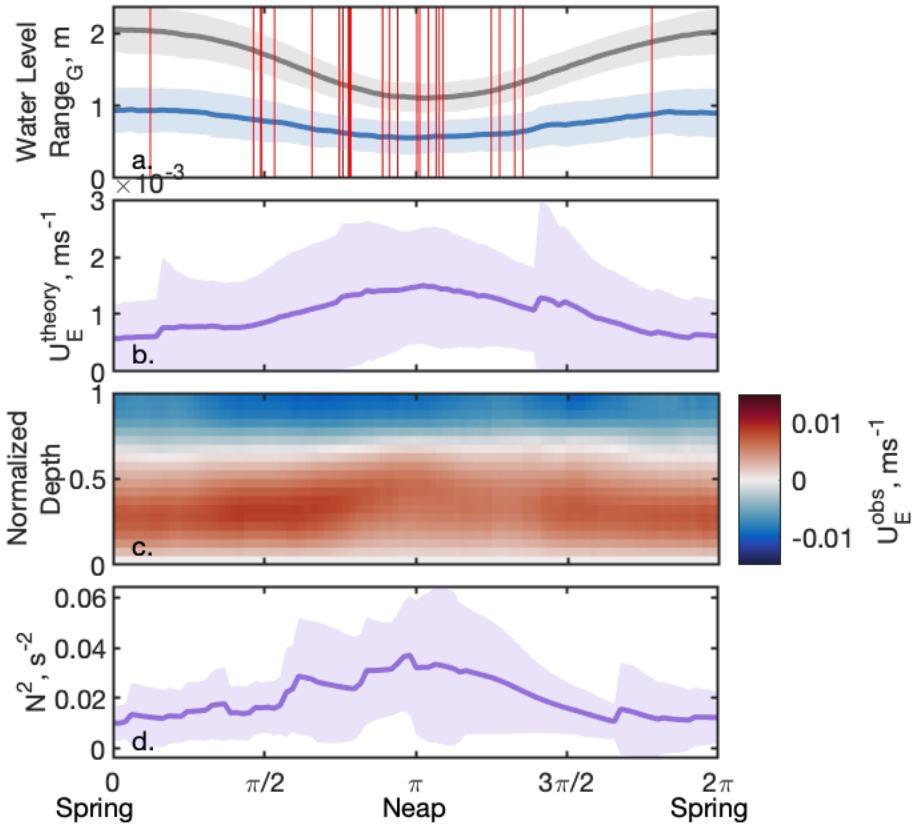

Figure 2.8: Spring/Neap Cycle: Phase-averages over the spring neap cycle (14.77 days) where 0 and 2π are spring tides, and π is a neap tide. a.) Godin-filtered water level range for offshore (gray) and lagoon (blue). Shading indicates +/- one standard deviation. Red lines mark the starting phase for all closures. b.) Theoretical exchange velocity based on Godin-filtered forcing parameters of water level, density difference between upstream, e3mid, and the ocean, o, and depth-averaged velocity magnitudes c.) Exchange velocity (defined as the Godin-filtered velocity minus the EOF mode 1 velocity) phase-averaged in depth-normalized coordinates. d.) Stratification (purple) based on bottom (e2bot) and surface density (e2top) and water depth. ~74 realizations are averaged into a, ~43 realizations are averaged into b, ~62 realizations are averaged into c, and ~9 realizations are averaged into d.

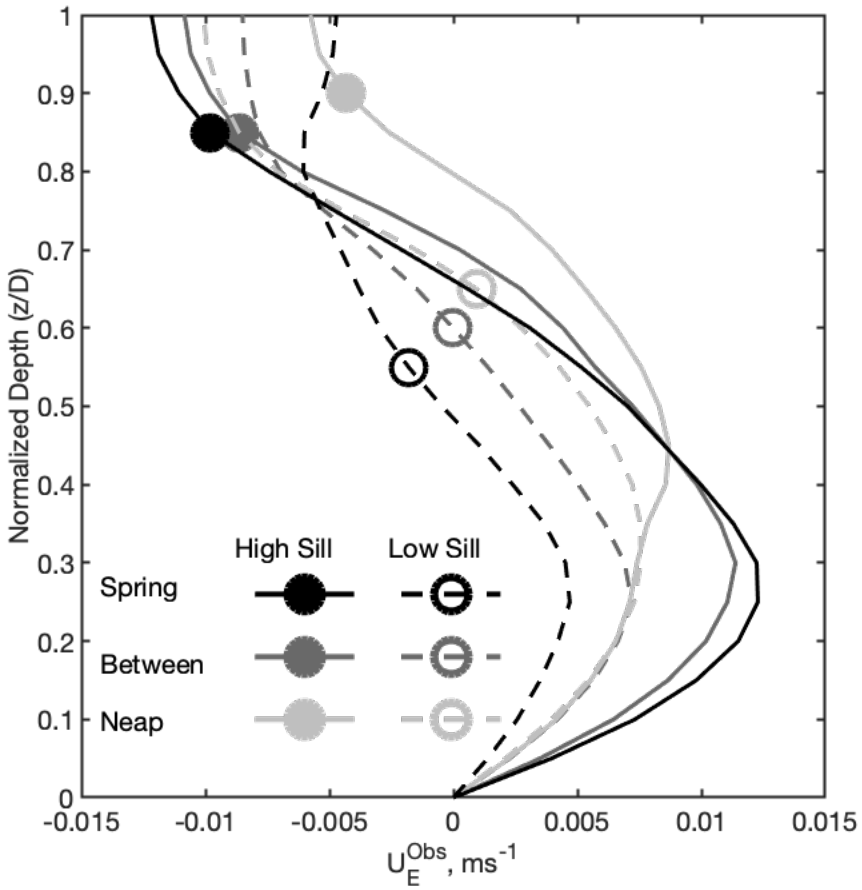

Figure 2.9: Mean exchange velocity profiles for low sill elevation (dashed lines, open circles) and high sill elevation (solid lines, solid circles) for spring tides (black), between spring and neap period (dark gray), and neap tides (light gray). The circles indicate the mean sill height for those averaging periods.

2.6 Tables

Table 2.1: Average number of realizations that go into M2 phase averages in Figures 2.6 and 2.7.

Variable	Open	Constricted	Closed	Spring	Neap
oWL	857	121	275	265	251
eWL	854	121	275	265	249
u_{e2}	686	119	254	203	203
ρ_{e1}	720	116	254	224	212
ρ_{e2bot}	354	84	219	102	104
ρ_{e2top}	203	60	160	46	72
N_{e2}^2	99	47	93	19	36
Dissolved Oxygen_{e2bot}	109	67	198	24	37
Dissolved Oxygen_{e1}	761	116	254	237	224
Turbidity_{e1}	764	116	254	238	226
Waves_{eP}	233	66	133	77	78

2.7 Acknowledgements

Chapter 2, in full, is currently being prepared for submission for publication of the material to Estuaries and Coasts. Harvey, Madeleine E.; Giddings S. N. Pawlak G.; Crooks, J. The dissertation author was the primary investigator and author of this paper.

Chapter 3

Circulation patterns and drivers during the closed state of an Intermittently Closed Estuary

In intermittently closed estuaries, waves and currents drive the transport and accretion of sand and cobbles into the estuary inlet and can build a sill high enough to block exchange between the estuary and ocean. Observations of 28 closures in Los Peñasquitos Lagoon, an intermittently closed estuary in Southern California, generally show that following closures water levels increase due to a combination of urban runoff, precipitation, river flow, and wave overtopping of the sill. Freshwater inputs stratify the estuary, limiting vertical mixing. Combined with closures blocking tidal exchange and thus reducing bottom-boundary layer mixing, the stratification often leads to hypoxic conditions at depth. The stratification during closures can vary but are generally dependent on the amount of incoming freshwater (which varies with season). The circulation patterns vary diurnally and are forced by differential heating and cooling driving convective cells (thermal exchange) that can be weakened by strong diurnal winds. This process is more evident during spring closures (most common) and is weakened during summer closures (rare). During summer closures, reduced stratification seems to lead to reduced circulation and more dominance of other processes besides thermal exchange.

3.1 Introduction

Intermittently closed estuaries are bar-built estuaries (estuaries with a sand bar sill near the mouth) that occasionally close off at the inlet to ocean exchange thereby trapping the estuarine water behind the barrier berm and effectively turning the estuary into a salt-stratified lake. These estuaries occur worldwide but are most commonly found in Mediterranean climates

or small watersheds with large wave action (Cooper, 2001; Dussaillant et al., 2009; McSweeney et al., 2017; Bertin et al., 2019; R. Clark and O'Connor, 2019). In bar-built estuaries, flood tides, waves, and wave-current interactions drive alongshore and cross-shore sediment transport into the inlets forming a sill comprised of sand and cobbles while ebb tides and fluvial events drive transport out of these systems (Ranasinghe et al., 1999; Behrens et al., 2013; Rich and Keller, 2013; Orescanin and Scooler, 2018). The competition between these processes dictate the sill height and the mouth state (open or closed). These systems have been referred to as, amongst other names, intermittently closed estuaries (ICE, Williams, 2014) temporary open/closed estuaries (TOCE,Teske and Wooldridge 2001), intermittently closed/open lakes and lagoons (ICOLLS, Gale et al., 2007) , and seasonally open tidal inlets (Ranasinghe et al., 1999). The duration of inlet closures can range from a part of a day to several years (Hastings and Elwany, 2012; Behrens et al., 2013).

Following a closure, the denser water near the mouth spreads out throughout the estuary through a combination of advancing density currents acting under gravity and the heaving of internal waves and seiches over bathymetrical obstacles (Behrens et al., 2016). The vertical stratification in closed estuaries can be influenced by wind, thermal heating, precipitation, and evaporation (Gale et al., 2006; Williams, 2014; Behrens et al., 2016). Wind can upwell the denser layer inducing a longitudinal density gradient that can drive a horizontal circulation and generate a seiche when it relaxes (Okely and Imberger, 2007; Behrens et al., 2016).

Horizontal density gradients due to differential heating can also drive convective motions, also known as thermal exchange, in coastal regions and lakes with sloping bathymetry. Warm water flows out of shallower regions towards deeper regions along the surface during positive heat fluxes and out along the bottom towards deeper regions during cooling periods

(Imberger and Patterson, 1989; Monismith et al., 1990; Farrow and Patterson 1993). In coastal zones, thermal exchange can be an important mechanism for cross-shore transport (Molina et al., 2014; Ulloa et al., 2018).

Closures can impact the water quality of ICEs. Strong vertical stratification inhibiting vertical mixing combined with a lack of tidal flushing during closures can lead to hypoxia in the bottom waters (Gale et al., 2006; Becker et al., 2009; Cousins et al., 2010) in some ICEs. Hypoxia (dissolved Oxygen concentration < 2 mg/L) can stress organisms and induce fish kills and death of benthic organisms. Nonetheless, many species have adapted to live in these closing environments (Dawson et al., 2001; Teske and Wooldridge, 2001; Bond et al., 2008; Becker et al., 2009; Hughes et al., 2014). In fact, managed breaching, if done incorrectly, can be detrimental for certain species because the entire water column can go anoxic if only the oxygenated surface waters spill out during a breach (Becker et al., 2009).

While some studies have examined the hydrodynamics of these closed systems (Gale et al., 2006; Williams 2014; Behrens et al., 2016), few have examined the variability of closures over multiple closures and multiple years. This paper presents results from extensive field observations from Los Peñasquitos Lagoon (LPL) in Southern California (Figure 3.1). LPL serves as the outlet to a 255 km^2 watershed draining Carmel Valley, Los Peñasquitos Canyon and Carroll Canyon. The lagoon is a designated Natural Marsh Preserve by the state of California and is part of the Torrey Pines State Reserve. LPL is small and shallow (max depth less than 4 m) estuary covering approximately 2 km^2 with extensive marsh habitat (Figure 3.1). The main channel is about 2.5 km long and less than 70 m wide. The lagoon inlet crosses a nourished sand and cobble beach (last major nourishment in 2001, (SANDAG, 2018) (minor nourishments every year during inlet dredging) which accretes in the summer and erodes in the winter (Ludka et al.,

2016). According to historical records and a study of marsh sediments (Cole and Wahl, 2000; Scott et al., 2011), prior to development the lagoon was primarily open with the first closure being recorded during the first railway construction in the late 1880s (Hastings and Elwany 2012). Closures now occur nearly at least once each year, more commonly during the winter and spring months, and last from several days to months. The inlet is managed and generally dredged during the spring (Hastings and Elwany, 2012; Young et al., 2018).

Field observations were initiated in LPL in December 2014 and continued through May 2019 (Figure 3.2). Observations were focused on physical parameters including water level, waves, bathymetry, currents, salinity, temperature, density, and oxygen. Few long data sets in small systems over closure periods exist and thus we are able to provide new insights into the dynamics and variability of small, shallow, bar-built estuaries during closures. After describing our methods, we describe the general stratification patterns and circulation characteristics of the closures during different seasons. We then discuss how the frequency of closures has change over time and what drives some of the seasonal and diurnal variability during the closures. Finally, we discuss how dissolved oxygen is affected by closures.

3.2 Methods

3.2.1 Velocity Measurements

A long-term mooring at e2 (see Figure 3.1) with an upward-looking 1200 kHz acoustic Doppler current profiler (ADCP, RDI Workhorse Monitor) sampling at 0.5 Hz in mode 12 was deployed on a bottom-mounted flat plate measuring velocity in 10-20 cm bins with blanking distances of 0 to 15 cm collecting data in either Beam (December 01, 2014 to February 17, 2015) or Earth coordinates (February 26, 2015 to June 14, 2019). The ADCP was swapped every 2-3 months collecting a nearly continuous record from December 01, 2014 until June 14, 2019. Due

to deployment logistics, the exact location and depth of each deployment varied slightly. They were adjusted to a consistent depth by aligning them to surveyed in pressure sensor sensors at e1 and when the system was closed eP (below).

Individual velocity measurements were ensemble averaged into 10-minute bins. For each deployment, velocities were rotated into the principal axis coordinates (u, v) based on each deployment's maximum variance during open periods. Velocities were transformed into depth-normalized coordinates ($\sigma = z/D$), where D is the instantaneous water depth. Velocities were extracted to the bed (assuming no flow at the bed and interpolating using a shape-preserving piecewise cubic interpolation) and surface (using a quadratic extraction that assumes $\frac{\partial u}{\partial z} = 0$ at the surface). Gray thatched areas on velocity and shear figures indicate extrapolated data.

3.2.2 CTD Measurements

Adjacent to the ADCP at e2, near-surface (mounted just beneath a floating buoy) and near-bottom conductivity, temperature, and depth sensors (CTD, SBE -37 SMP) sampling at 1 minute and 2 minutes (5 minutes after June 2017) respectively, were deployed (Figure 3.2d, light and dark blue). Dissolved oxygen measurements were collected using SBE-63 optical dissolved oxygen sensor at the bed from November 03, 2015 to October 09, 2017 and January 10, 2019 to June 20, 2019 (Figure 3.2e) and at the surface between January 10, 2019 and April 02, 2019. The CTDs periodically experienced significant biofouling and sediment trapping resulting in artificially low salinity measurements. Unrealistic data was removed from all analysis. In some cases, the instrument was not obviously fouled, however data was questionable and is denoted by a dashed line in Figure 3.2d. Surface and bottom density measurements were used to calculate a bulk stratification using the Brunt–Väisälä frequency, $N^2 = -\frac{g}{\rho_o}\frac{\Delta\rho}{\Delta z}$ where ρ_o is the average density.

At e1bot a bottom-mounted CTD-DO was deployed from March 06 2017 to April 03 2017 (gray circle in Figure 1c).

In addition to the moorings, four CTD-DO instruments with turbidity and pH (YSI dataSondes) were deployed on pilings by the Tijuana River National Estuary Research Reserve (TRNERR) System Wide Monitoring Program (SWMP) fixed at approximately 1 m above the bed (i.e., mid-water column) sampling at 15-minute intervals. Two instruments at e1mid and e3mid (upstream and downstream of our ADCP/CTD mooring respectively) were deployed in the main channel (Figure 3.1, Figure 3.2d, medium blue (e1mid) and purple (e3mid)). Due to bridge construction, the e1mid sensor was moved approximately 50 meters downstream October 29, 2015 and was located about 0.75 m higher in the water column from October 29, 2015 to February 27, 2017. The absolute elevation of e1mid was obtained with a Spectra Precision Epoch 50. Water elevations at e1mid were corrected with atmospheric pressure at SIO Pier or Los Peñasquitos when available. During 2 ~1 month gaps in the water elevation time series at e1mid (September 2015 and March 2017) water levels were supplemented with pressure measurements from the ADCP corrected with atmospheric pressure at SIO Pier. All data was interpolated to 10-minute data.

3.2.3 Wave Measurements

During each winter (approximately November through late March/early April) a buried Paroscientific, Inc. pressure sensor was deployed just inside of the inlet (eP) . The sensor was buried approximately 1 m under the sand, although sediment accreted and eroded throughout the deployment period. Sensor locations varied slightly year to year due to a mobile cobble layer and the ease of jetting the sensor into the sand. eP was moved once on March 17, 2017 when accretion exceeded one meter causing the sensor to no longer be in direct wave action. The

pressure sensors sampled at 2 Hz continuously for 59.73 minutes each hour. eP pressure measurements were corrected to account for frequency attenuation effects due to burial (Raubenheimer et al., 1998). A 2 Hz pressure sensor stationed at Scripps Institution of Oceanography, approximately 7.5 km south of the LPL inlet, was used to remove the barometric pressure from eP.

Variance preserving spectra were computed for 30 minute windows every 15 minutes from the pressure signals at eP, Each 30-minute window was divided into 11 segments with 75% overlap. Significant wave heights for the swell and infragravity bands (H_{IG} and H_{SW}) were calculated according to $H = 4 * \sqrt{\int_{f1}^{f2} \text{Energy df}}$ where $f_1 = .167$ Hz, $f_2 = .04$ Hz, (6 to 25 sec periods) for swell energy, and $f_1 = .04$ Hz, $f_2 = .004$ Hz (25 to 250 sec periods) for infragravity wave energy.

3.2.4 Meteorological Measurements

Earth Networks, Inc. provided barometric pressure, cloud cover, precipitation, relative humidity, dew point, air temperature, and wind data from Scripps Institution of Oceanography (SIO) Pier, approximately 7.5 km south from LPL. Incoming solar radiation measurements are from a solar radiometer connected to a Hydroclimate Station on the Scripps Pier (data provided by Douglas J. Alden and Daniel R. Cayan of Climate Atmospheric Science and Physical Oceanography, SIO). Cloud cover data was based on cloud descriptions from Miramar Marine Corps Air Station (National Climatic Data Center ID: USW0093107). Cloud cover was roughly converted to percentage of sky covered such that clear = 0%; scattered = 15%; broken = 50%; overcast = 70%.

3.2.5 Bathymetry

Bathymetric data in the main estuary channel was collected along transects using the bottom ping from a towed downward-looking ADCP. The water depth was corrected for tidal level and converted into absolute elevation by subtracting a concurrently deployed, surveyed pressure sensor, at e1mid. Upstream of the railroad bridge the transects were from January, 2015, January 12, 2016, January 29, 2016, and February 08, 2016. Downstream of the bridge the transects were from February 23, 2017, and March 06, 2016. Additionally, depth measurements using depth from occasional CTD casts were used to supplement depths in the channel. Bathymetric data was objectively mapped with gaussian weights and a 6-m radius of influence in the horizontal. Elevation of the shallower regions near the mouth are collected from drone data converted into elevation with structure-from-motion software (Pix4D).

3.2.6 Additional measurements

River flow rates are from the United States Geological Survey (USGS) Los Peñasquitos Creek Gauge 11023340. Elwany (2011) calculated that the continuous Los Peñasquitos Creek USGS gauge accounts for 85% of the inflow, thus the USGS reported values are multiplied by 118% to approximate the total river inflow.

3.3 Analysis Methods

3.3.1 Heat Budget

A parameterized heat budget of the lagoon was calculated using weather data from Earth Networks, Inc. archived data at Scripps Pier, Miramar cloud cover data (approximated into percentage of sky covered), surface temperature data at e2top (or midwater temperature data at e1mid when surface was unavailable), density data at e1mid, and solar radiation data from Scripps Pier. The shortwave heat flux (Q_{sw}) is the component of the downwelling solar radiation

(Q_{sw}^{d}) able to penetrate into the water based on the albedo, α=0.06, where $Q_{sw} = Q_{sw}^{d}(1-\alpha)$ and always positive. The longwave heat flux (Q_{Lw}) is the net of the emitted longwave radiation (Q_{Lw}^{s}) and the downwelling longwave radiation (Q_{Lw}^{d}) such that $Q_{Lw} = Q_{Lw}^{d}(1-\alpha_L) - Q_{Lw}^{s}$ where $\alpha_L = 0.045$ (Josey et al., 1997). Q_{Lw} was calculated using a parameterization from (Clark et al., 1974). The sensible (Q_H) and latent (Q_E) heat fluxes were calculated using the 3.0a TOGA (Tropical Oceans Global Atmosphere) COARE (Coupled Ocean-Atmosphere Response Experiment) bulk algorithm (Fairall et al., 2003) which incorporates wind speed, barometric pressure surface temperature, air temperature, specific humidity, downward solar heat flux, downward long wave flux, and rain rate. Cool skin, warm layer, and wave corrections were not applied. The net surface heat flux (Q_T) is the combined total of the shortwave, longwave, sensible and latent heat fluxes such that $Q_T = Q_{SW} + Q_{LW} + Q_H + Q_E$. All fluxes were calculated at 30-minute intervals. The Q_{SW} is positive; Q_{LW} and Q_E are negative; Q_H is predominantly negative. When the estuary was closed, the 30-minute change in observed surface temperature (dT/dt) correlated with Q_T ($r = 0.55$, $p < 0.01$). When the midwater temperature was used in the calculation (instead of the surface temperature) the observed change in surface temperature remained significantly correlated with Q_T ($r = 0.53$, $p < 0.01$) indicating it was acceptable to use the midwater temperature in the TOGA COARE bulk algorithm at times when the surface temperature was unavailable. The sum total of the daytime (06:00 – 18:00 PST), nighttime (18:00 – 06:00), and 24-hour (18:00-18:00) total heat fluxes were also calculated using the 30-minute heat fluxes.

3.3.2 Diurnal Phase Averaging

Various parameters were phase-averaged in order to examine consistently repeatable patterns. All variables were interpolated or bin-averaged to 10-minute data prior to phase

averaging. All data was then diurnally-phase averaged. Diurnal phase averages start and end at consecutive midnights.

3.3.3 Exchange Velocity Calculations

10-minute averaged along-stream sigma-coordinate velocities (u) were lowpass (LP) filtered using a 72-hour Butterworth filter (denoted with $u_{72hr\ LP}$) to examine long-term trends. $u_{72hr\ HP}$ refers to 10-minute averaged along-stream velocities minus the 72-hour lowpass filtered velocities ($u_{72hr\ HP} = u - u_{72hr\ LP}$). A band-pass (BP) filter of along-stream velocities using Butterworth filter cutoffs of 6-hr and 72-hours is used ($u_{6:72\mathrm{hr}\ BP} = u_{6hr\ LP} - u_{72hr\ LP}$) to examine diurnal trends with the background state removed.

The running variance of $u_{6:72\mathrm{hr}\ BP}$ over a 1-day window were computed for all sigma levels. The exchange height (σ_E) is defined as the normalized depth level of the maximum of the running variance. The exchange velocity is calculated as the average of the velocity of ~1/5 of the water column below the exchange height minus the average of the velocity of ~1/5 of the water column around the exchange height:

$$u_E = \overline{u_{6:72\mathrm{hr}\ BP}(\sigma_E - .25 : \sigma_E - .10)} - \overline{u_{6:72\mathrm{hr}\ BP}(\sigma_E - .05 : \sigma_E + .10)}$$

with positive u_E indicating out along the surface and in at depth. The daytime exchange is the strength of u_E at 12:00 (noon) and the nighttime exchange is the exchange at 24:00 (midnight).

3.3.4 Frequency analysis

The spectra of each depth-normalized layer of 10-minute along-stream velocity was taken during the closed periods for 3-day windows every 1.5 days. The total amount of diurnal or 24 hour energy is defined as the integrated energy between 20 and 30 hours.

3.4 Results

3.4.1 Closures Description

During the observation period, 28 closures occurred ranging in length from 0.75 to 70 days. 2016 had the largest number (246) of days closed. Over all years, 13 closures lasted more than 7 days. About 9 of the closures naturally breached while the remainder were breached with mechanical aid (dredging with excavators and other machinery) (Figure 3.2). 9 of the closures occurred within 0-3 days of previous closures (often the result of incomplete dredging or breaching or large wave events).

During all closures, the estuary water levels slowly increased (Figure 3.3c), with the exception of the summer closure, due to a combination of urban runoff, precipitation, river flows (Figure 3.3h, purple), and wave overtopping (Figure 3.3h, black). Overtopping was most frequently observed at eP towards the beginning of the closure when the sill was the lowest and during offshore high tides with large offshore waves (Chapter 2). At e1mid, e2bot, and e3mid, the density decreased over the closure duration. The density at e2bot typically decreased less rapidly than at e1mid (downstream) indicating increasing stratification over time. The density at e2top also showed that the surface water either freshened or remained fairly fresh throughout the closure (although this CTD suffered from frequent biofouling and/or questionable data, Figure 3.3f). Oxygen generally decreased over the length of the closure. At e1mid, the midwater became hypoxic (dissolved oxygen content < 2 mg/l) in 15 closures over the course of <1 to 21 days. At e2bot, the bottom water became hypoxic over <1 to 14 days. At e2top, surface oxygen measurements were only available during one closure where the surface waters (at 0.3 meters) decreased in oxygen although not as rapidly as at e2bot. All oxygen measurements had fluctuations with a peak period of 24 hours. At e1mid diurnally-averaged oxygen peaked around 17:05 and at E2Bot the oxygen peaked around 14:50.

The mean profile of u during all closures showed a continuation of a weak estuarine circulation (Chapter 2) with flows downstream at the surface and upstream at depth resulting in an exchange flow of about (0.008 m/s), lower than when the estuary is open (0.015 m/s when open, Chapter 2). Variability at a range of frequencies is present in u, $u_{6:72\mathrm{hr}\ BP}$ (Figure 3.3d), and $u_{72hr\ LP}$ (Figure 3.3e).

3.4.2 Closure Groupings

To characterize different types of circulation, the closures were divided into the following groups by season: Winter/Spring; Summer; and Fall. Winter/Spring includes closures greater than 4 days with start dates been January and May (gray sections in Figure 3.3). Note that closures with very large river flows or incomplete data were not included. There was only one summer closure, the longest in our record. Because it exhibited two rather distinct circulation patterns, summer was subdivided into Summer 1, marked by relatively constant density and a 2-layer flow, pink section in Figure 3.3; and Summer 2, the second half of the summer closure with a gradual decrease in salinity and 3-layer flow, yellow section in Figure 3.3). Fall includes only one fall closure (purple section in Figure 3.3).

3.4.3 Winter/Spring

The Winter/Spring closures were the most abundant accounting for all but 3 closures and 43% of total time closed during the study period. The peak period of temperature fluctuations, wind, velocity, and oxygen during this period was 24 hours. In a diurnal phase average of the winter/spring closure data, DO at e1mid shows a minimum at ~07:15 and a maximum at ~15:45. At e2bot the DO peaked earlier in the day (~14:50) and had a smaller range than e1mid (Figure 3.4a). The diurnal temperatures reach maximums at 16:05, 19:30, and 21:05 for e2top, e1mid, and e2bot, respectively with e2top having the largest daily variability and decreasing variability

with depth as expected. The longitudinal temperature, salinity, and density gradients between e1mid and e3mid show, on average, lower temperature (Figure 3.4b), higher salinity, and higher density at e1mid compared with e3mid (average ΔT = 1.74 C, ΔS = -2.8 psu, and $\Delta\rho$ = -2.73 kg/m^3). The amount of heat flux is generally positive from 08:10 to 16:55 with a maximum at 12:25 (Figure 3.4c). The diurnal wind is generally weak and from the south-southeast at night and stronger from the west (onshore winds) during the day, with onshore winds peaking around 13:20 (Figure 3.4d).

The diurnally phase-averaged 72-hr high-passed along-stream velocities ($u_{72-hr\ HP}$) have a strong 24-hour signal with a peak outflow at $\sigma = 0.75$ around 11:45 and a peak inflow at $\sigma = 0.70$ around 23:10 (Figure 3.4e) with weaker return flows at depth. During the afternoon, when the onshore sea breeze is strong, the outflowing velocity strength decreases and there is a slight inflow near the surface during the day, although much of this signal is in the region of extrapolated data as indicated by the hatching in Figure 3.4e.

In this group, the peak period of u was 24 hours with most of the energy higher in the water column (between $\sigma = 0.5$ and $\sigma = 0.9$, Figure 3.5). During the longer Winter/Spring closures, the σ layer with the largest amount of energy in the 24 hour band generally decreased over time (Figure 3.5). Similarity, the location of maximum variance (the depth σ_E around which u_E is calculated) deepened over the length of most closures. The daytime exchange (u_E) is strongest when the daytime heat flux is high (circles with no outline, Figure 3.6). The daytime heat flux and the exchange decrease with increased wind velocities. The nighttime exchange (triangles with no outline, Figure 3.6) is generally stronger when the nighttime heat flux is larger (more negative) with the exception of when the nighttime winds are strong from the westerly direction.

3.4.4 Summer 1 and Summer 2

The single summer closure was the longest closure during the study period (71 days). The closure accounted for 18% of the closed time during these 4.5 years. The temperature at all locations was the highest of any closure. At e3mid temperatures reached 34.4 C. The correlations between the calculated heat budget and the dT/dt were higher ($r = 0.62$, $p < 0.01$) than the correlations for the entire record. The nighttime cooling during the summer was high resulting in negative 24-hour total fluxes (Figure 3.3a). The river flows were very low (average 0.016 m^3/s during summer compared with 0.174 m^3/s for all closures, potentially below the gauge threshold of the instrumentation, Figure 3.3h). The water levels were much lower than other closures (average 1.42 m in summer; 1.63 m for all closures). The closure had relatively constant densities with much lower than average stratification compared with other that of other closures ($N^2 = .0034$ in summer; 0.022 in all closures) and did not increase over the closure (Figure 3.3f).

The first half (before August 1st 2016) and second half of the summer closure exhibit fairly different circulation patterns and will be defined as Summer 1 and Summer 2 respectively (Figure 3.3; pink and yellow vertical sections, respectively). In Summer 1, the densities at e1mid, e2bot, e2top, and e3mid were all fairly constant while during Summer 2, all densities decreased at a relatively constant rate that was similar at all sensors. Throughout the summer, the water remained oxygenated longer than other closures (Figure 3.3g and 7, pink line).

During Summer 1, the circulation was two-layered with strong bottom inflows (Figure 3.3a). The level of maximum variance (σ_E) was much deeper than other closures (Figure 3.3d). While the peak period was still diurnal, there was less energy than in the Winter/Spring closures and the energy was confined to the lower portion of the water column (between $\sigma = 0.2$ and $\sigma = 0.6$) (Figure 3.5). During Summer 2, the circulation exhibited more of 3-layer flow. The

diurnal energy was slightly larger and slightly higher in the water column than Summer 1, but still lower than other closures.

3.4.5 Fall

There was only one closure during the fall which accounted for 10% of the total closed time during the record. During the closure there was very little nighttime cooling which resulted in mostly positive heat flux totals. While not as low as the summer period, the river flows were small (average 0.029 m^3/s during fall compared with 0.174 m^3/s for all closures). This period also had relatively little stratification develop although the water column went hypoxic longer than the summer closure. Level of maximum variance (σ_E) was generally in the middle of the water column but highly variable. Similarly, the level with the most amount of energy in the 24 hour band was in the middle of the water column. During this period the winds were different than other periods with several Santa Ana wind periods (winds from the east).

3.5 Discussion

3.5.1 Closure Interannual Variability

Over the period of data collection, December 2014 – May 2019, 28 inlet closures occurred in LPL when sand and cobbles accreted in the inlet. The closures occur when sand accretion in the inlet, due to waves, flood tides, and wave-current interactions, exceeds erosion and scour that can be caused by ebb tides and fluvial events (Ranasinghe et al., 1999; Behrens et al., 2013; Rich and Keller, 2013; Orescanin and Scooler, 2018). 9 of the closures occurred than 48 hours after the inlet opening, typically during dredging activities, and thus there were 20 unique closures. The estuary closed primarily during neap tides (Chapter 2) when weak outflowing currents were unable to maintain an open inlet (Behrens et al., 2009). Natural closures (excluding the closes that occurred while dredging and earthwork operations were

happening near the inlet) occurred when the sill elevation (computed from lower-low water level, Harvey et al., 2019) was higher than 1.25 m NAVD88 on average.

In LPL, since the inlet bridge was reconstructed in 2004, the inlet has generally been closed between 0 and 246 days each year, with mean and median closure lengths of 58 and 46 days respectively, with 60 days standard deviation. Most closures occur during the winter and spring months (see Figures 2 and 3). Inlet management typically occurs in the late spring (April – May) although emergency inlet breaches may occur (typically removing a smaller volume of sand) (LPL Foundation et al., 2016).

Closures in the winter and spring (December 1st – May 31st) account for 82% of the total days closed since 2004 (72% of total days closed during this study). Only 5 years have had closures between June 1st and December 1st (7 days in 2007, 8 days in 2010; 3 days in 2012; 19 days in 2013; and 126 days in 2016) (Hastings and Elwany, 2012; Young et al., 2018; Largier et al., 2019). 2016 was anomalous both in terms of total days closed and the length of closure during the summer. The 2015-2016 El Niño brought extremely large waves and slightly below average precipitation to southern California (Barnard et al., 2017; Siler et al., 2017; Young et al., 2018). The large waves and lack of river flows (Figure 3.2f) during the El Niño caused significant accretion to estuarine inlets all along the Southern California Bight (Harvey et al., 2019; Young et al., 2018) and increased inundation of estuaries (Harvey et al., 2019; Goodman et al., 2018). The extreme waves during the El Niño built a large (> 2 m) cobble berm which, combined with the sand accretion in the inlet impeded dredging efforts. The dredging budget was effectively maxed out in the spring and thus the inlet remained closed for the summer.

3.5.2 Frequencies of Variability

During the closures the peak energy period is 24 hours for nearly all levels below $\sigma = 0.2$. An exception is the Winter/Spring, when the peak period in the bottom waters is 12 hours (although there was energy in the 24 band as well). During the Winter/Spring, energy in the 24-hour band was higher than the energy in Summer or Fall periods. During all periods, internal waves motions that have a period of around 1 to a few hours (consistent with the range of phase speeds for baroclinic internal waves acting under the observed stratification and estuary length). The velocities also have peaks in the energy at 12, 8, and 6 hours presumably because the velocity is frontal rather than sinusoidal. The wind and total heat flux also have peak periods of 24 with additional peaks in the energy at 12 hours, 8 hours, and 6 hours likely due to the non-sinusoidal nature of the signals. For the wind, a small peak the windspeed an night during a land breeze (much smaller than the sea breeze strength) may have also contributed to the peak at 12 hours (Masselink and Pattiaratchi, 2001).

3.5.3 Stratification

During the Winter/Spring closures, freshwater inputs due to precipitation, river discharge, and urban runoff (ungauged freshwater runoff from agriculture, urban use, etc.) and higher upstream temperatures generate a canonical circulation structure (downstream at the surface and upstream at depth) consistent with that observed during the open period (Chapter 2; Geyer and MacCready 2013). Whether natural or manmade (White and Greer 2006) the low momentum freshwater entering the system causes the pycnocline to deepen over the length of the Winter/Spring closures. The pycnocline deepening is evident in $u_{6:72hr\ BP}$ (Figure 3.3d) as the gradual deepening of σ_E (maximum vertical location of the 24-hour running variance), the density measurements diverging (Figure 3.3f), and the location of maximum 24-hour integrated energy deepening. During the Fall and Summer closures the stratification is lower causing the σ_E

and the location of maximum 24-hour integrated energy to be deeper in the water column. Due to stratification, any atmospheric forcing, for example, convective motions due to differential heating or cooling, (Imberger and Patterson, 1989; Monismith et al., 1990; Farrow and Patterson, 1993) or wind forcing (Gale et al., 2006; Williams 2014; Behrens et al., 2016) would have affected the waters below the pycnocline less than the waters above.

3.5.4 Thermal Exchange

While in similar systems, a diurnal exchange was generally forced by the sea breeze (Behrens et al., 2016), in LPL u_E generally starts just as wind starts but it is acting in the wrong direction (Figure 3.4e). Additionally, when the sea breeze is strong, direction (Figure 3.6, size of circles), the exchange flows are generally weaker. When the daytime heat flux is strongly positive, the exchange is large (Figure 3.6, circles). Similarly, when the nighttime heat flux is strongly negative and the winds are light, the exchange is large in the negative direction (Figure 3.6, triangles). This pattern is consistent with diurnal exchange forced by differential heating and cooling or thermal exchange (Farrow & Patterson, 1993; Imberger & Patterson, 1989; Molina et al., 2014; Monismith et al., 1990). The outflows (Figure 3.4e, blue) during the day appear to be due the shallower upstream waters heating up more than the deeper waters and flowing out over the deeper waters near the surface. The nighttime inflows (Figure 3.4e, red) appear to be driven by cooling upstream waters inducing a gravity current downslope (Monismith et al., 1990) and being replaced by surface waters in the deeper region. Longitudinal gradients, varying topography (Figure 3.1c), and ADCP blanking distance may minimize the appearance of the near-bottom outflows during the night (Figure 3.4e) With the exception of days with strong winds (which also affect the heat flux), the nightly exchange is generally larger during more negative heat fluxes.

The exchange is deeper (Figure 3.3d) and weaker (see black outlines on Figure 3.6) during the Summer and Fall. The reduced and deeper stratification likely determines the exchange depth. Moreover, the reduced stratification allows wind to affect more of the water column during these periods, thus counteracting any thermally driven exchange more strongly. For example during the Summer 1 period when stratification is reduced currents near the surface (at the upper-most ADCP bin) are directed by wind (Figure 3.7). Unfortunately, due to the ADCP's region of side-lobe interference near the surface, we are unable to resolve the wind affected surface layer when stratification is stronger. Additionally, the warmer conditions during Summer and Fall periods lead to a larger longitudinal gradient of temperature (the daily average temperature between e3mid and e1mid are $\Delta T = 4.1°C;\ 4.5°C;\ 3.0°C$; for Summer 1, Summer 2, Fall, and Winter/Spring respectively) which may restrict the thermal exchange circulation cell further upstream.

3.5.5 Dissolved Oxygen Dynamics

The dissolved oxygen content generally (with the exception of the summer and fall closure) decreased over time during closures (Figure 3.3f and Figure 3.8). With a 6-hour low pass filter applied, winter/Spring closures became hypoxic between 1.5 and 24 days at e2bot and 5 and 14 days at e1bot (note: not all closures included oxygen sensor deployments). In the raw data, the waters became hypoxic faster but for shorter duration. At e2bot the oxygen on average decreased at a rate of ~0.4 mg/L/day (Figure 3.8). During our one closure with surface oxygen measurements at e1top, the near-surface water (~.35 m from surface) dissolved oxygen also depleted suggesting that there may be strong stratification near the surface or that the entire water column experiences deoxygenation. The Summer and Fall closures were significantly less stratified than other closures (likely due to the lack of precipitation, riverflow, and runoff) which

may have allowed the bottom waters to remain oxygenated through vertical mixing (Gale et al., 2006). It is possible the temporal variability of chemical or biological factors including species present or nutrient loads played a role in the variability of oxygen however no biological (ie. Chlorophyll fluorescence, species abundance, species diversity) or chemical measurements (ie. Nitrate or Phosphate concentrations) were performed.

3.5.6 Ecological and Management Implications

The amount of dissolved oxygen in the water column and spatial variability of oxygen can have a large impact on the ability of species to survive closures. Motile species can migrate to areas with more oxygen or remain in the more oxygenated surface waters, while sessile species must either have adaptation methods or may die. It is hypothesized that overtopping may be a source of potential oxygen delivery. During a large overtopping event on March 23, 2017 (Figure 3.9a) cooler, denser water propagated upstream to e1bo t(Figure 3.9b). At the arrival of the gravity current the dissolved oxygen content increased approximately 0.2 mgL^{-1} (Figure 3.9c). More species might be able to survive near the inlet if the sill is relatively low and overtopping is occurring.

While there is some debate on the management of these systems, it is interesting to note that while this estuary naturally closed, it would have likely been opened during periods of large precipitation and runoff and closed during periods of less precipitation of rainfall (like the summer or fall). As such, it would have been closed when stratification was less likely to develop, and it is possible the water column would have remained more oxygenated.

3.6 Summary and Conclusions

In intermittently closed estuaries, closures occur when sediment accretes in the inlet blocking off the estuary from the ocean effectively forming a salt stratified lake. Following

closures, water levels increase in the estuary due to a combination of river flows, overtopping (Figure 3.3h), precipitation, and urban runoff. During the Winter/Spring closures, when river discharge is higher, the pycnocline deepens as low momentum freshwater enters the system. We found that the stratification and circulation patterns during closures can vary dramatically between closures but that the patterns are relatively consistent amongst seasons where the amount of incoming freshwater dictates the strength and depth of stratification. While circulation patterns occur at high frequencies (such as internal waves and potentially internal seiches), the dominant energy is in diurnal velocity oscillations. The diurnal circulation is attributed to differential heating and cooling driving thermal exchange circulation cells that can be weakened by diurnal winds which drive circulation cells in the opposite sense. During closures, dissolved oxygen near the bottom typically declines rapidly. Near the inlet, overtopping may be an important mechanism for introducing oxygenated water into the system. The dissolved oxygen decline is generally dependent on stratification although it is likely that biological and chemical processes additionally impact oxygen availability.

3.7 Figures

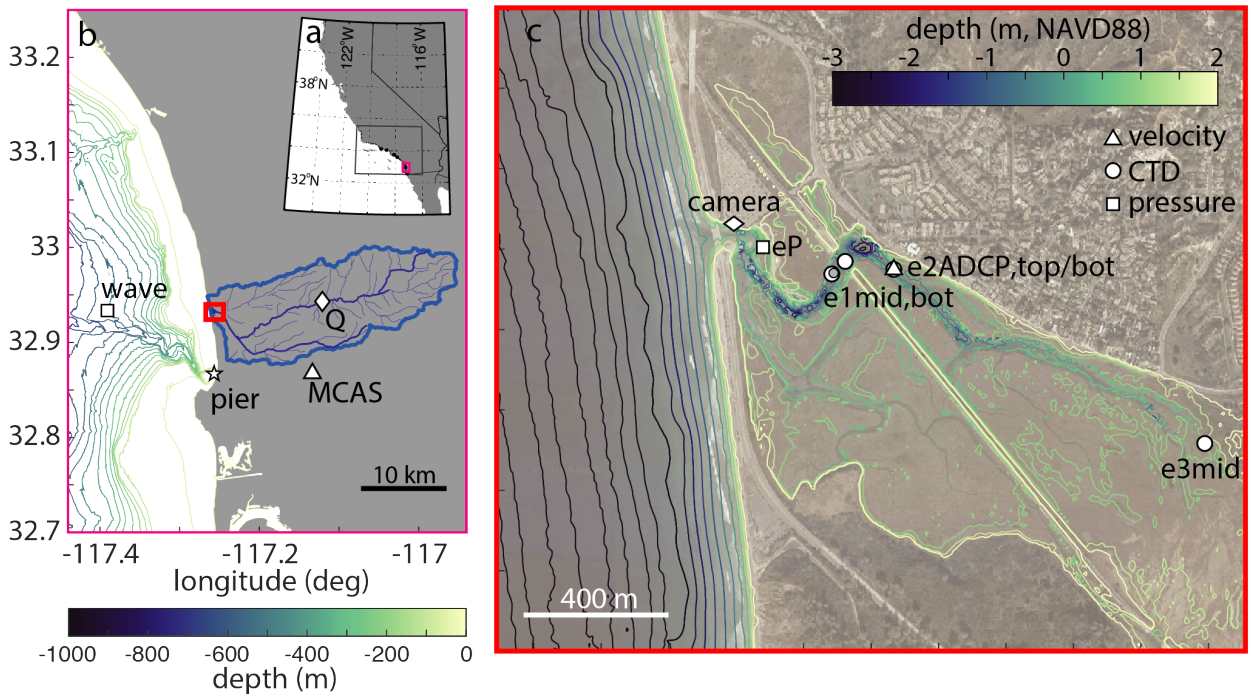

Figure 3.1: Location of Los Peñasquitos Lagoon and instruments deployed. a.) California coastline with San Diego delineated. b.) San Diego coastline with watershed of Los Peñasquitos Lagoon and offshore bathymetry. USGS river gauge noted as Q; SIO Pier denoted as pier; CDIP Buoy 100 denoted as wave; Mirimar air station denoted as MCAS. c.) Image of Los Peñasquitos Lagoon with instrument locations (white for nearly continuous measurements, gray for short-term deployments) overlain on marsh topography and bathymetry in teal (light colors are higher elevation). Estuary bathymetry was collected from a combination of UAV measurements and towed ADCP measurements, while those offshore are from the 1/3 arc-second San Diego Coastal DEM model from NOAA and all are referenced to NAVD88.

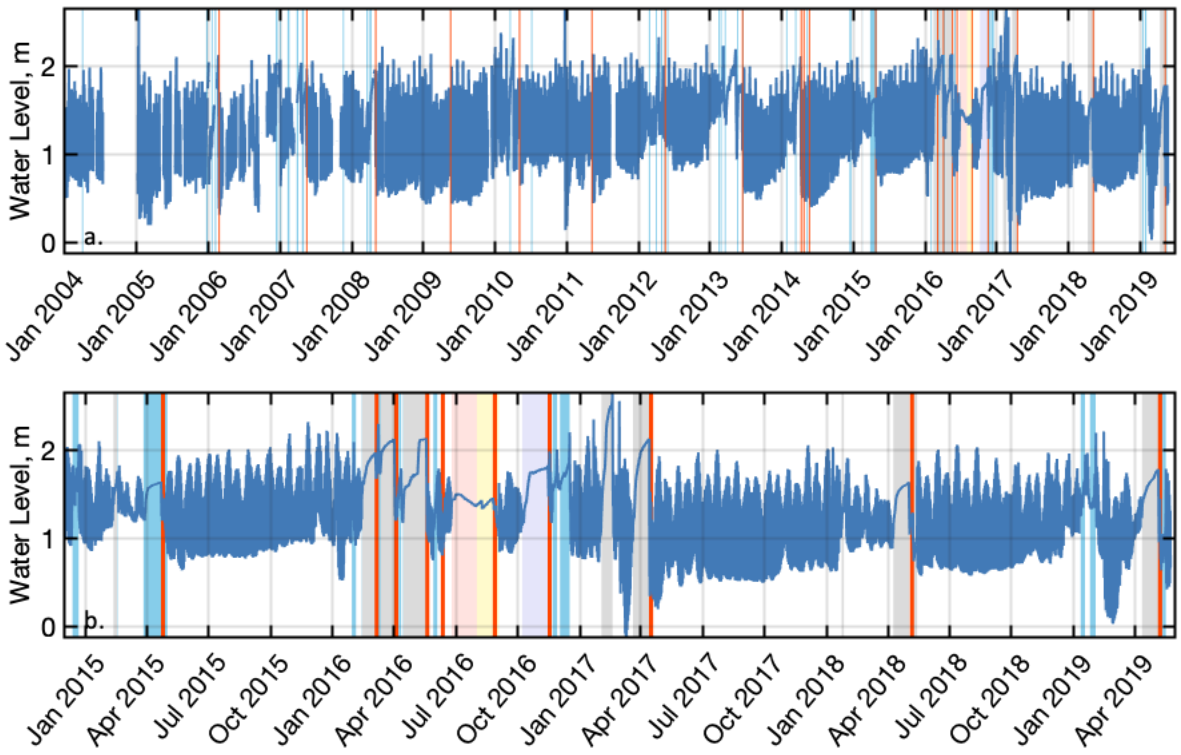

Figure 3.2: Timeseries of water levels, closures, and dredging in Los Peñasquitos Lagoon closures are delineated in blue, gray, pink, yellow, and purple. Mechanical inlet openings are delimitated as red bars. Gray, pink, yellow, and purple closures are explained in 3.4.2 and Figure 3.3. a.) Water levels between January 01 2004 and July 01 2019 b.) Water levels between December 01, 2014 and June 01 2019.

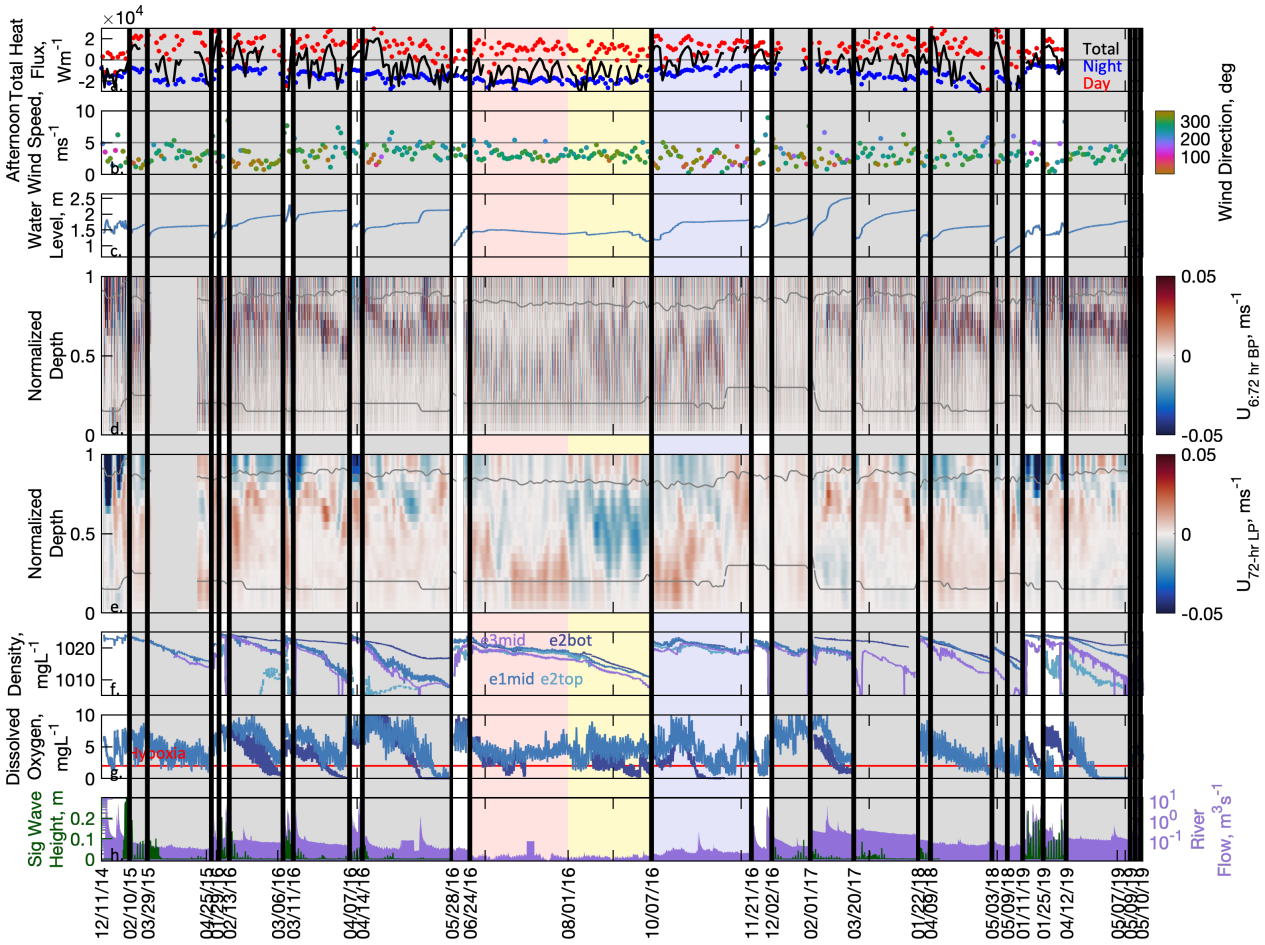

Figure 3.3: Time Series of Closures. All 28 closures are concatenated on this Figure 3.where individual closures are separated by thick vertical black lines. Longer closures are grouped and colored by similarities and seasons: Winter/Spring (gray); Summer 1 (pink); Summer 2 (Yellow) Fall (Purple) Winter/Spring includes closures greater than 4 days with start dates been January and May. Note that closures with very large river flows or incomplete data were not included. a.) Total heat flux over day (0600-1800, red), night (1800-0600, blue), and total (1800-1800, black). b.) Mean wind speed and direction of afternoon winds (1200-1800). The sea breeze is from 270 degrees (green). c.) Water levels d.) 6:72-hr band-pass filtered along-stream velocities ($u_{6:72\mathrm{hr}\ BP}$). Gray lines indicate locations of interpolated data to the surface or bottom. e.) 72-hr low-passed filtered velocities ($u_{72\mathrm{hr}\ LP}$). f.) Density at e2bot (dark blue), e1mid (medium blue), e2top (light blue), and e3mid (purple). g.) Oxygen at e2bot (dark blue) and e1mid (medium blue) sensors with hypoxia (2mg/L) indicated in red. e.) Significant wave height at eP (black). River flow (purple, USGS gauge 11023340).

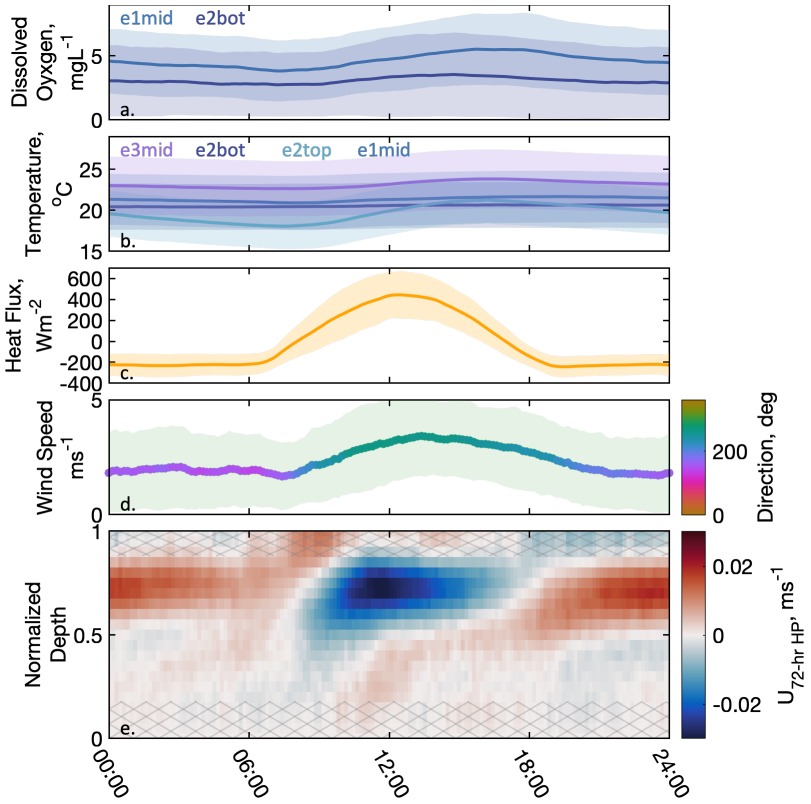

Figure 3.4: Diurnal phase-averages of Winter/Spring closures (gray sections in Figure 3.2 and 3). a.) Dissolved Oxygen at e1mid (medium blue) and e2bot (dark blue). b.) Temperature at e2bot (dark blue), e1mid (medium blue), e2top (light blue), and e3mid (purple) locations. c.) Total heat flux. d.) Wind speed and direction (color). Shading on a-d indicate 1 standard deviation of the phase average. For direction, green indicates an onshore wind (sea breeze). e.) 72-hour high pass filtered velocities calculated as the 10-minute averaged along-stream velocities minus 72-hour low pass filtered velocities. Gray hashing indicates regions of interpolated data to surface or bottom.

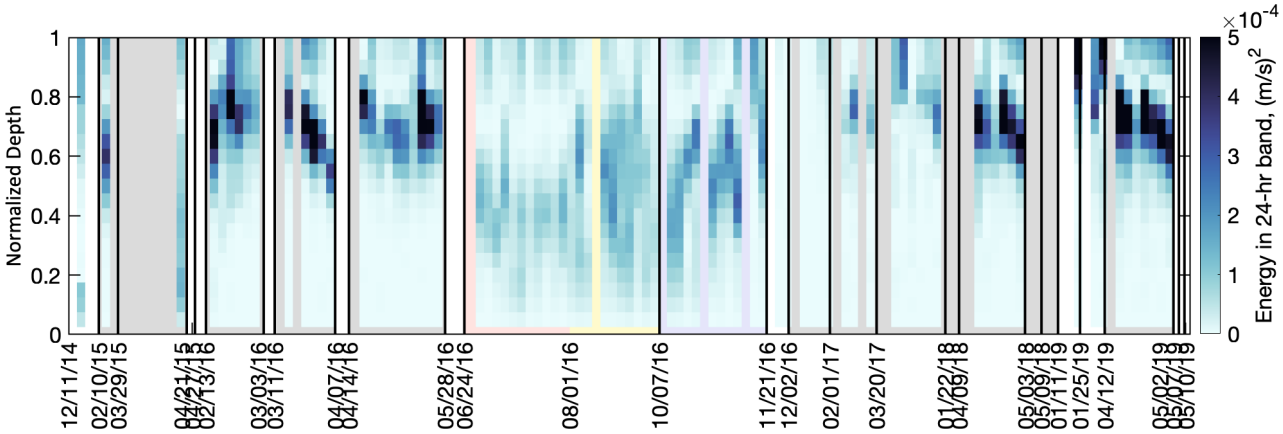

Figure 3.5: Integrated energy in the 24-hour band (20-30 hours) of spectral energy density of 10-minute averaged along stream velocities, u over each closure and over depth. Spectra are calculated using a 3-day window calculated every 1.5 days for all depth-normalized levels. Darker colors indicate more energy in the band.

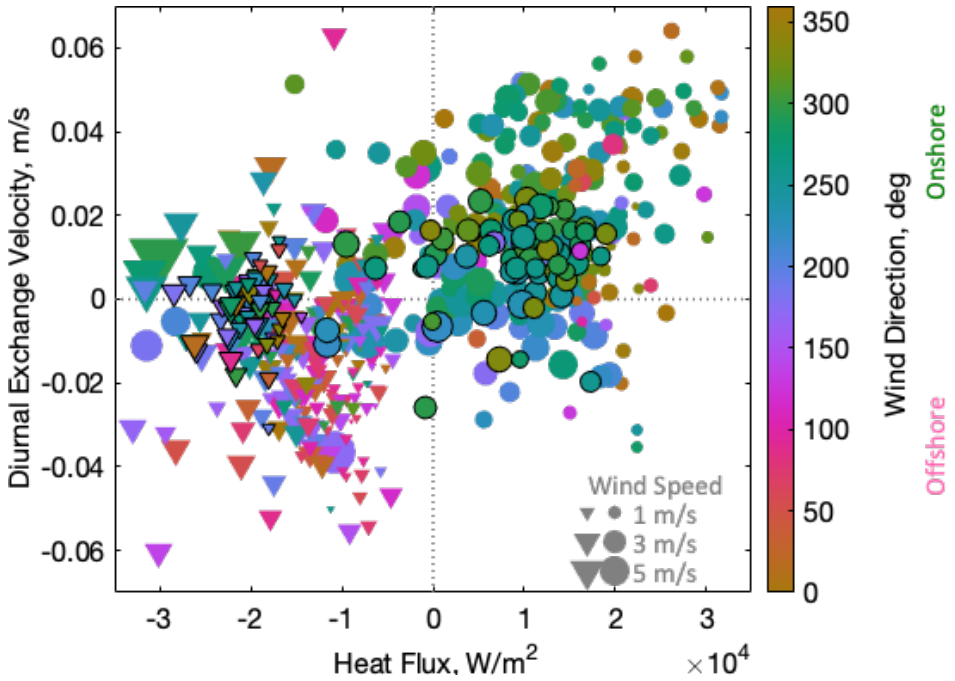

Figure 3.6: Exchange velocity vs. 30-minute integrated heat flux over day or night. Dots indicate daytime values; triangles indicate nighttime values. The symbol size is scaled by the wind speed (small = low wind) as indicated on the legend; while the color is based on the wind direction where greens are onshore and pinks are offshore directed winds. Symbols outlined with thin black lines indicate summer and fall values (pink, yellow, and purple shading on Figure 3.3). Exchange velocities are calculated around the level of maximum variance (as described in Section 3.3.2.3). Positive exchange velocity indicates inflow at depth, outflow at the surface. The heat flux is the cumulative day (or night) heat flux over 12 hours. Note that an exchange flow driven by heating alone would be positive (i.e., upper-right quadrant), whereas an exchange flow driven by cooling would be negative (i.e., lower-left quadrant). On the other hand, strong onshore (offshore) winds would act in the direction of a negative (positive) exchange flow.

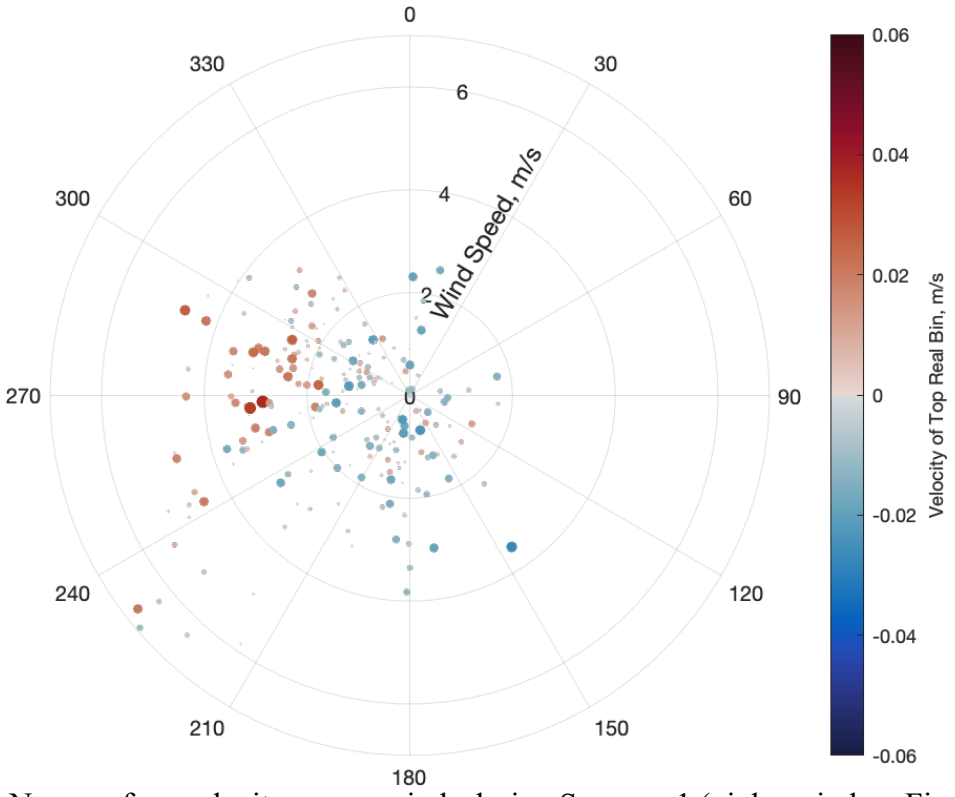

Figure 3.7: Near-surface velocity versus winds during Summer 1 (pink period on Figure 3.3). Velocity of the nearest surface ADCP bin (not extrapolated) (color and size of dot) is plotted on a wind rose. The theta-axis is wind direction with wind speed increasing along the radial axis. Velocities into the estuary (onshore) are indicated by 270 degrees.

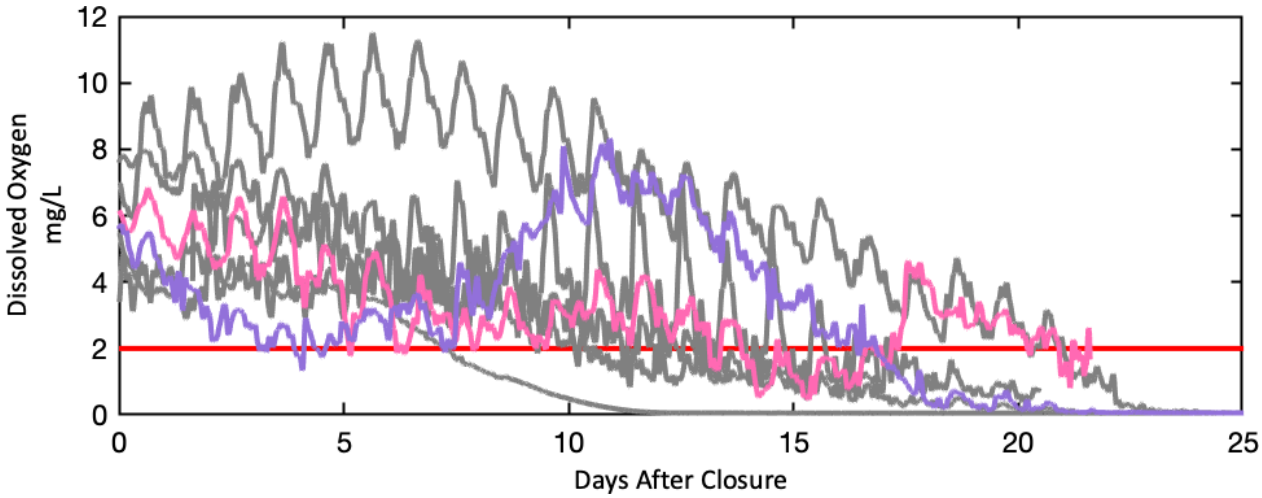

Figure 3.8: Dissolved Oxygen Depletion. 2-hour lowpass filtered dissolved oxygen at e2bot over all closures. 0 indicates midnight the day of closure. Gray, pink, and purple indicates Winter/Spring, Summer, or Fall, respectively.

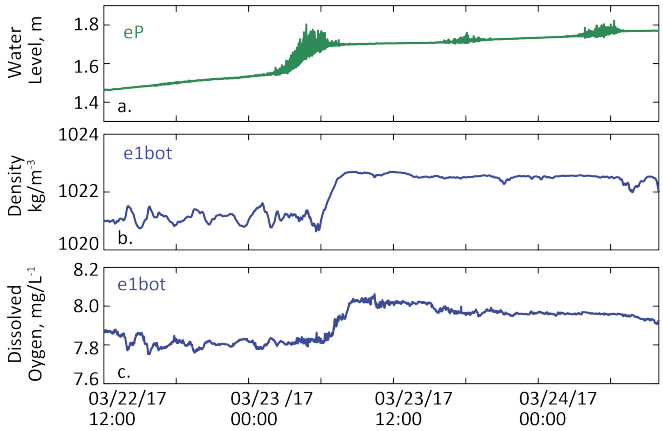

Figure 3.9: Wave overtopping event during March/April 2017 closure. a.) Water level at eP b.) density at e1bot approximately 500 m upstream c.) Dissolved oxygen at e1bot.

3.8 Acknowledgements

Chapter 3, in full, is currently being prepared for submission for publication of the material to Estuaries and Coasts. Harvey, Madeleine E.; Giddings S. N. Pawlak G.; Crooks, J. The dissertation author was the primary investigator and author of this paper.

Chapter 4

Advantages and disadvantages of deploying a distributed temperature sensing system in the inlet of an intermittently closed estuary

To complement longer-term hydrodynamic studies of Los Peñasquitos Lagoon, an intermittently closed estuary in Southern California, two distributed temperature sensing (DTS) cables were used to examine high temporal and spatial resolution temperature changes. While T-S relationships in many estuaries are not robust such that concurrent salinity measurements are necessary, we set out to test what additional dynamics such high resolution measurements could provide. The cables were deployed in March and April 2017 along with co-located thermistors, conductivity sensors, dissolved oxygen sensors, and current profilers. The DTS system uses the relationship between the frequency shift of backscattered light sent through a fiber-optic cable and the temperature of the cable to determine the temperature of the surrounding fluid in 1 meter increments. Over the deployment period, the estuarine inlet was open to the ocean for two weeks and closed for two weeks. During the open period, the salt wedge propagation can be measured through its strong cooler temperature. During the closed period, the system warms due to a net positive heat budget and the DTS captures a large sill overtopping event which abruptly cools the inlet area and delivers oxygen to the bottom waters. The DTS system is a novel tool that allows us to observe the along-channel and cross-channel bottom water temperature fluctuations and frontal propagation in the estuary at unprecedented temporal and spatial resolution. Nonetheless, challenges including cable placement, accuracy of cable location and depth, and cable burial

revealed some fundamental issues with deciphering the underlying physical processes driving estuarine inlet circulation with a DTS system.

4.1 Introduction

Low-inflow, bar-built estuaries (BBE) are generally small, shallow systems with narrow tidal inlets (cross-sectional area on the order of 100 m^2 or less) (Ranasinghe & Pattiaratchi, 2003) that experience rapid morphological changes and occasional closures. They are common on wave-dominant coasts with low and/or seasonal rainfall and microtidal (Cooper, 2001; Davidson et al., 2009) or mesotidal (Behrens et al., 2013; Rich & Keller, 2013) range. BBEs can be found on coasts worldwide including: California (Clark & O'Connor, 2019; Largier et al., 2019), Spain (Moreno et al., 2010), Portugal (Bertin et al., 2019; Dodet et al., 2013), Australia (Gale et al., 2007; Ranasinghe & Pattiaratchi, 1999; Roy et al., 2001), South Africa (Clark & O'Connor, 2019; J. Largier et al., 2019), and Chile (Dussaillant et al., 2009). In BBEs, flood tides, waves, and wave-current interactions drive alongshore and cross-shore sediment transport into the inlets forming a sill comprised of sand and cobbles while ebb tides and fluvial events drive transport out of these systems mesotidal (Gale et al., 2007; Ranasinghe & Pattiaratchi, 1999b; Roy et al., 2001).

The sill height and location can have profound impacts on the circulation, inundation, stratification, and dissolved oxygen in the system (Behrens et al., 2016; Cousins et al., 2010; Gale et al., 2006; J. L. Largier & Taljaard, 1991; Williams & Stacey, 2016). In these systems, when the profiles of the flooding and ebbing tides are dependent on the sill (Chapter 2) with the profiles being more depth uniform when the sill is low and more sheared when the sill higher. During a flood tide when the sill is high, ocean water may enter the system more like a density current (Blanton et al., 2000; J. L. Largier & Taljaard, 1991). During an ebbing tide, the ocean

drops below the sill elevation, effectively cutting off ocean forcing and outflowing velocities are controlled by hydraulics and friction (Williams & Stacey, 2016).

When discharge is low enough and waves are strong enough, the sill can eventually grow high enough to completely close the estuary from oceanic exchange. Following closures, estuarine water levels increase due to a combination of urban runoff, precipitation, river flow, and occasional overtopping of oceanic water over the sill at the mouth. The freshwater inputs can stratify the system and the resulting stratification can facilitate the development of hypoxic bottom water conditions (Chapter 3, (Clark & O'Connor, 2019; Cousins et al., 2010; Gale et al., 2006)). The vertical stratification and circulation in closed estuaries can be influenced by wind, thermal heating, precipitation, and evaporation (Behrens et al., 2016; Gale et al., 2006; WIlliams, 2014). Overtopping of the sill can both build the sill higher (Baldock et al., 2008) and deliver ocean water into the closed system. Overtopping delivers oceanic waters carrying salt and zooplankton (Kemp & Froneman, 2004) into the system.

While several studies have looked at the circulation and wave action near tidal inlets, no study has observed the circulation of the inlet area undergoing large morphological changes in high spatial and temporal resolution. To provide a better understanding of the circulation, we use a fiber-optic Distributed Temperature Sensing (DTS) cable to examine the evolution and variability of the bottom water temperature and to assess the DTS capabilities in such a dynamic environment. The DTS uses the relationship between temperature and light scattering to determine the temperature around a point in the cable. A coherent light pulse is sent down a fiber optic cable and the backscattered Stokes and Anti-Stokes Raman spectra are continuously measured to determine the temperature along the length of the cable (Hausner et al., 2011; Selker et al., 2006; Tyler et al., 2009). The DTS has been deployed in a variety of environmental

applications (Shanafield et al., 2018) including over an atoll looking at the intrusion of internal waves onto a reef flat (Reid et al., 2019), on the inner shelf examining frontal structure (Connolly & Kirincich, 2019) and shoaling internal waves (Lucas & Pinkel, 2018), and in lakes measuring their heat balance (van Emmerik et al., 2013; Vercauteren et al., 2011).

In this study we use a DTS to observe and examine the evolution and variability of the bottom water temperature in Los Peñasquitos Lagoon (LPL) for 2 weeks before an inlet closure, through a closure, and the two weeks following a closure. Here we both assess the deployment and observational challenges of using a DTS system in such a complex estuarine environment as well as highlight some of the scientific results as well as hypotheses that such a high spatial and temporal resolution temperature provides. In the following sections we first discuss the experimental set up including how the DTS was deployed and how we analyzed the data, we then discuss some results from the DTS during open and closed periods. Finally, we discuss some advantages and challenges of deploying a DTS in an estuarine inlet.

4.1.1 Experimental Set-Up

4.1.1.1 Los Peñasquitos Lagoon

Measurements were conducted in Los Peñasquitos Lagoon (LPL) a small, shallow, bar-built estuary in Southern California. LPL is located in a Mediterranean climate with little precipitation during the summer and episodic inputs during the winter. Inlet closures occur nearly every year for days to months with most closures happening during the winter and spring months. The inlet is managed and generally dredged during the spring (Chapter 3, Hastings & Elwany, 2012; Young et al., 2018). Analyses of the tidal, fortnightly, seasonal, interannual during open periods (Chapter 2) and closed periods (Chapter 3) have in earlier chapters.

4.1.1.2 Bathymetry

Bathymetry surveys near the inlet were conducted on 02 March 2017, 13 March 2017, 27 March 2017, and 05 April 2017 using an upside-down, boogie-board mounted 1200 kHz RDI ADCP during high-tides. While small bathymetry changes could be seen for each subsequent survey, all 4 were objectively mapped together. The bathymetry was converted into NAVD88 by referencing the water level at a nearby surveyed-in pressure sensor (eP). High resolution photographs of the inlet area were taken at low-tide with an eBee fixed wing drone. A digital elevation map of the exposed mudflats and surrounding marshlands was constructed using structure-from-motion photogrammetry using Pix4D Mapper Pro. 17 reference points were used to constrain the resulting digital surface elevation model.

4.1.1.3 The DTS System

4.1.1.3.1 DTS Instrumentation Set-Up, Averaging, and Calibration

A high resolution Silixa XT-DTS system (the source and receiver of fiber optic signals) with 2 Mini LT Flat Drop Cables was deployed in LPL from 04 March to 06 April 2017 (subsequently referred to as the DTS or DTS cables). The Silixa XT-DTS was connected to shore power and located near the inlet next to two calibration baths. The cables (~900m and ~1100m) ran from the instrument, into each of the calibration baths, along a shallow berm near the inlet, and into the thalweg ~140 m from the highway bridge. Each cable had two fiber optic cores that were connected to the Silixa XT-DTS instrument on one end and spliced together in a turnaround on the other end to create a double-ended duplexed system (Hausner et al., 2011). The turn-around was waterproofed in a Tyco Gator Splice box and affixed to a pole on the marsh above the higher-high water line. As a single light pulse produced 2 synchronous backscattered signals of water temperature at each location along the cable (due to the turnaround creating a double-ended duplexed) the two temperatures for each location were averaged together. For the majority

of the experiment, both ends of the fiber optic filament were connected to the instrument and the light pulse was sent down each direction alternatively. For the first 5 days (until March 7, 2017), only one end was connected to the instrument but both sides still backscattered the light signal.

Bottom temperatures along each cable were measured approximately every minute at 0.25 m spatial resolution and were averaged to 10 minutes with 1 m spatial resolution for most analyses. For the high-frequency analysis, the data was averaged to 2 minutes.

For calibration purposes, 2 SBE 56s and a 10-m section of each cable were placed into each of the two temperature-controlled baths (one ambient temperature ~19.2 ^{o}C with a standard deviation of 0.9 ^{o}C, one warm ~26.8^{o}C with a standard deviation of 1.1^{o}C). A 10-m section of each cable was also coiled near the cable end with a SBE 56 attached for validation. Co-located SBE 56 thermistors were placed at 296 m, and 541 m along the shorter cable at 526 m, 744 m along the longer cable. All SBE56s used sampled at 1 Hz. The thalweg cable at 541 m had an approximately 0.1^{o}C root mean squared error (RMSE) compared with the co-located SBE 56 (Figure 4.2).

4.1.1.3.2 Location of the DTS

After crossing the shallow shoal near the inlet, the shorter cable ran ~400 m upstream in (or near) the thalweg. The shorter cable missed deeper portions in some areas with large scour holes. The shorter cable then zigzagged back downstream over the channel and flats for ~80 m longitudinally with cross-channel sections about every ~30 m. After crossing the shallow shoal near the inlet, the longer cable section ran in a zigzagged fashion upstream for ~350 m with cross-channel sections every ~40m along the bend to ~15 meters in the straighter section before the bridge. The cables were marked with along-cable distances (meter marks or marking) every meter. These markings were used to help determine where along the physical cable the return

signal (recorded by the Silixa XT) corresponded to. The meter marks were validated against the return signal by noting the marking of where the cables entered the baths as those constant temperature locations were easily identified in the return signal. Additionally, the meter mark of the turn-around point was known as its return signal was easily identified as the temperature about the turn-around point was nearly symmetric.

The cables were deployed from a small inflatable pontoon boat with the shorter thalweg cable deployed first and the longer zigzagging cable deployed on top. As the cable was deployed, small weights were affixed to the cable approximately every 30 m to prevent the cable from moving in the currents. The GPS location the weight and corresponding meter mark was noted. Floating lines were attached to the weights with the intention to use the lines to determine if the cable was moving with currents, however biofouling on the lines caused them to sink. The GPS locations of the weights was primarily used to determine the location of the cable that traveled up the thalweg.

When the cable zigzagged across the channel, the meter mark where the cable was tied off to sand anchors was noted. The high resolution imagery and structure-from-motion derived elevations from drone flight on March 8th was used to determine the elevation and horizontal location of all exposed cable sections. The along-cable distance from each sand anchor (and known meter mark) for all exposed sections was determined using the drone data. When the cable submerged for a zigzag crossing the meter marks were interpolated between the last shallow location known from the drone data to the deepest location. The coldest mean temperature during the closed period (March 22 and April 4th) for each cable crossing span was assumed to be located at the deepest cross section location (known from the bathymetry survey).

Wherever the cables ran across the channel, at least one weight was attached near the deeper location to prevent the cable from moving significantly in the current.

Knowing exactly where the cable was in X, Y, and Z space was necessary to understand if it the cable was exposed or underwater and to analyze the results relative to the estuary bathymetry. Sources of error for the location of which meter mark corresponds to what depth include the GPS accuracy, the vertical resolution of the drone and ADCP measurements, the mapping between the returned data and the cable meter mark, and the assumption that the cable is lying straight on the bed between the March 8th exposed endpoints. These errors combine to lead to location errors of as high as 3 m in the horizontal and 1.5 m in the vertical. If the water level was below the determined elevation (from the above description), the cable was assumed to be exposed. Additionally, known exposed sections of cable exhibited higher temperature variance than those underwater. Thus, if the moving variance for about 2.5 m sections of the pre-spatially interpolated data (10 minutes, 0.25 m spatial resolution) was larger than 0.05^{o}C, the cable was assumed to be exposed. The exposed data was removed from the subsequent analysis. Similarly, a known section of buried cable had higher variance, thus variance was also used to estimate cable burial. Unfortunately, only areas with excessive burial were easily identified by this method while areas with small amounts of burial may have been missed. While this data was not removed from the subsequent analysis, the deeper areas of the cross-sections that we focus on for these analyses did not appear to have significant burial affects.

4.1.1.4 Moorings

In addition to the DTS, 6 additional moorings were deployed during this time period. However, in this chapter we will only discuss results from 3 additional moorings at e1, e2, and Tchain (Figure 4.1c). Mooring e1 consisted of bottom CTD-DO (e1bot) and a surface CTD

(e1top). Unfortunately, the long-term instrument at e1mid was hit with debris during the large discharge event prior to the study and thus was not deployed. A thermistor chain (TChain) with 6 vertical SBE56s was deployed downstream of e1. As throughout the longer-term measurements discussed in Chapters 2 and 3, mooring e2 had, a surface CTD, bottom CTD-DO, a bottom thermistor, and a 1200 kHz acoustic Doppler current profiler (ADCP, RDI Workhorse Monitor) sampling at 0.5 Hz in mode 12 was deployed on a bottom-mounted flat plate measuring velocity in 15 cm bins with blanking distances of 15 cm collecting data Earth coordinates. Individual velocity measurements were ensemble averaged into 10-minute bins. Velocities were rotated into the principal axis coordinates (u, v) based on each deployment's maximum variance during open periods. Velocities were transformed into depth-normalized coordinates ($\sigma = z/D$), where D is the instantaneous water depth. Velocities were extracted to the bed and surface (assuming no flow at the bed, σ= 0, and no shear, $\frac{\partial u}{\partial z}$ = 0 at the surface, σ = 1).

As in prior winter/springs, Two buried Paroscientific, Inc. pressure sensors were deployed just offshore (in the surfzone, szP) and just inside of the inlet (eP). Sensors were buried approximately 1 m under the sand, although sediment accreted and eroded throughout the deployment period. The lagoon sensor was moved once on March 17, 2017 when accretion exceeded one meter causing the sensor to no longer be in direct wave action. The pressure sensors sampled at 2 Hz continuously for 59.73 minutes each hour. szP and eP pressure measurements were corrected to account for frequency attenuation effects due to burial (Raubenheimer et al., 1998). szP and eP variance preserving spectra were computed for 30 minute windows every 15 minutes.

4.1.1.5 Meteorological Measurements and Heat Budget

A parameterized lagoon heat budget was calculated using meteorological data and surface temperature data at the TChain. Earth Networks, Inc. provided barometric pressure, cloud cover, precipitation, relative humidity, dew point, air temperature, and wind data from Scripps Institution of Oceanography (SIO) Pier approximately 7.5 km south. Incoming solar radiation measurements are from a solar radiometer connected to a Hydroclimate Station on the Scripps Pier (data provided by Douglas J. Alden and Daniel R. Cayan of Climate Atmospheric Science and Physical Oceanography, SIO). Cloud cover data was based on cloud descriptions from Miramar Marine Corps Air Station (National Climatic Data Center ID: USW0093107). Cloud cover was converted to percentage of sky covered such that clear = 0%; scattered = 15%; broken = 50%; overcast = 70%.

The shortwave heat flux (Q_{sw}) is the component of the downwelling solar radiation(Q_{sw}^{d}) able to penetrate into the water based on the albedo, α=0.06, where $Q_{sw} = Q_{sw}^{d}(1-\alpha)$. The longwave heat flux (Q_{Lw}) is net of the emitted longwave radiation (Q_{Lw}^{s}) and the downwelling longwave radiation (Q_{Lw}^{d}) such that $Q_{Lw} = Q_{Lw}^{d}(1-\alpha_L) - Q_{Lw}^{s}$ where $\alpha_L = 0.045$ (Josey et al. 1997). Q_{Lw} was calculated using a parameterization from (Clark et al. 1974). The sensible (Q_H) and latent (Q_E) heat fluxes were calculated using the 3.0a TOGA (Tropical Oceans Global Atmosphere) COARE (Coupled Ocean-Atmosphere Response Experiment) bulk algorithm (Fairall et al. 2003). Cool skin, warm layer, and wave corrections were not applied. The net surface heat flux (Q_T) is the combined total of the shortwave, longwave, sensible and latent heat fluxes such that $Q_T = Q_{SW} + Q_{LW} + Q_H + Q_E$. Q_{SW} is positive; Q_{LW} and Q_E are negative; Q_H is predominantly negative. When the estuary was closed, the 30-minute change in surface temperature (dT/dt) correlated with Q_T (r =0.53 , $p < 0.01$).

4.2 Results

4.2.1 Overview of Observation Period

During the observation period of March 04, 2017 to April 06, 2017 the lagoon mouth was open for 16 days and closed for 17 days (Figure 4.4). The largest river flow event since December 2010 occurred immediately prior to the deployment period (February 27, 2017 to March 01, 2017) which scoured the sill near the mouth to the lowest level since at least December 2014 (the start of the Chapter 1 observations). Throughout the study period, the river discharge gradually decreased with the exception of three small storms. The closure (while gradual) occurred on March 20, 2017. A storm with high waves and precipitation occurred on March 23, 2017. The storm caused the closed estuarine water level to rise to ~0.3 meters over two days due to a combination of precipitation, river flow, and overtopping (Figure 4.4 d and e).

When the estuary was open, the depth-averaged tidal velocities peaked at ~0.25 m/s during the spring tide and decreased as the system started to close. (Figure 4.4 a). After closure, small velocity oscillations (~0.05 m/s) occurred. When the estuary was open, the surface and bottom salinities fluctuated with the tide. During the open period, the bottom water gradually became more saline as freshwater was flushed from the system following the large river discharge event. Unfortunately, several salinity sensors malfunctioned during the study period and thus we do not have trustworthy surface salinity measurements while the estuary was closed. A salinity sensor upstream (e3) showed that salinity in the mid-to-upper water column decreased through the closed period, likely in response to continual, albeit small, input of freshwater. Periodic CTD casts showed strong stratification with freshwater near the surface and saltier water at depth (Figure 4.4 b and inset). Following the closure, fluctuations of the dissolved oxygen have a diurnally frequency, and the mean dissolved oxygen content slowly decreases

(Chapter 3, Figure 4.4 c). Temperature was generally warmer in the lagoon than in the ocean, as measured at Scripps Pier (Figure 4.4 f).

4.2.2 Open Period Temperatures

When the system is open, during a flooding tide, colder ocean water propagates up-estuary (purple, Figure 4.5 b-d) cooling the inlet area, and water levels increase inundating the shoal regions (Figure 4.5 e-f). The shoals are inundated for a larger period of time during the larger tides due to the higher water levels (Figure 4.6). An M2 phase-average during the open period of a cable crossing shows that the bottom water temperature in the channel during the low tide (~1π, Figure 4.7) is generally ~1.0 ºC degrees warmer than the high tide (~0π and ~2π, Figure 4.7). The temperature gradient during the flood tide (~1.5π, Figure 4.7) is significantly stronger than during the ebb tide (~0.5π, Figure 4.7) suggesting that mixing occurs over the course of a tidal cycle. The sharpness of the phase-averaged flood tide temperature signal suggests it may be propagating into the system as a salt wedge.

The arrival of the salt wedge is evident in the nightly flood tide data as the rapid arrival of cooler (~15.0 ºC) water in the deepest channel section (Figure 4.8). Unfortunately, the arrival of the daytime flood tide is complicated by diurnal heating making the flood tide frontal propagation difficult to extract. The arrival of the flood tide at each cross section is determined by the fastest rate of cooling of a 100-minute running mean of the thalweg location (where the thalweg was determined by the coolest location during the closed period). The resultant frontal speed (Figure 4.9) at each location is taken to be the along-thalweg distance between the deepest location at the previous cable crossing and the deepest location at the given crossing divided by the difference in arrival times. Negative velocities indicate that the front appeared to arrive at a

crossing before arriving at the previous downstream crossing (Figure 4.8). It is possible this is because water traveling up the thalweg gets trapped in large scour holes.

In the lateral direction (across the channel and shoals), the salt wedge does not consistently arrive in the deepest section first. In fact, the cool ocean water generally appears to arrive in shallower locations on either side of the channel prior to the thalweg (Figure 4.10). The northern shoal is narrower than the southern shoal so the arrival on the southern shoal is much more obvious with cool water arriving in the shallower regions of the shoal before the deeper region. One complicating factor is that the channel crossings do not run perpendicular to the thalweg but cut across at an angle. Nonetheless, the front arrival at the shallower regions first is robust when all cables are taken into account.

4.2.3 Closed Period Temperatures

Over the entire deployment, the temperature range at a given estuary cross section is over 10^{o}C (Figure 4.6) with the coldest waters occurring when the system is open during a nighttime flooding tide and the warmest waters over the shoals during the closures. Following closures, the water levels rise and inundate the shoals. When the system was closed, both the channel and the shoals warmed substantially due to a net positive surface heat flux. Following the large overtopping event on March 23, 2017, the system heated 4.4 ^{o}C in the deepest location of the thalweg and 5.5 ^{o}C on average over the shoals. The bottom water temperature heats and cools throughout the day as expected with the surface heat fluxes (~.035 ^{o}C in the thalweg and ~2.8 ^{o}C on the shoals).

When the system is closed, a higher frequency analysis of 2 minute data shows that both on the mudflats and into deeper water higher frequency temperature fluctuations on the order of ~6 hours occur (Figure 4.11).

4.2.4 Overtopping during a Closure

During the DTS closure, overtopping of the sill occurred ~17 times with one overtopping event being significantly larger and resulting in a ~20 cm increase in stagnant water level (Figure 3.8). During the overtopping event 0.075 cm IG waves prorogated to PT2. The ocean water was able to propagate up through the DTS cable array resulting in a temperature decrease down to between 1 and 2^{o}C with the minimum temperature generally increasing with distance upstream. The overtopping event brought more oxygenated, higher density water upstream to the bottom CTD at mooring e1bot (Figure 3.8). The density maximum of 1023 kg/m^3 indicates that the ocean water substantially mixed with the lagoon water or the density current pushed already mixed deep lagoon water up to the CTD location. The speed of the overtopping density current during closure (Figure 4.12) was nearly half of the speed of the flood tide frontal propagation during the open state (Figure 4.8).

4.3 Discussion

4.3.1 Advantages of using a DTS cable in a dynamic inlet

The DTS system provides a coherent spatial and temporal picture of the variability of bottom water temperature. In a tidal inlet, this is a valuable asset for understanding how quickly tidal fronts are able to propagate, their lateral structure, and how they mix with estuarine waters. Other than the DTS instrument, only models currently can provide such a wealth of synchronous spatial data. The advantage of this instrument over traditional moorings is that you are able to see where in the lateral direction the tidal front arrives first, the time lag between the arrival in the thalweg, the banks, and the shoals.

In this study, we were able to track the flood tide salt wedge speed as it propagated upstream. This was accomplished using the estimated thalweg location at each consecutive DTS

cross-section, rather than the along-channel DTS cable as its placement did not accurately track the thalweg. The frontal speed (Figure 4.8) varied as it propagated upstream. Negative speeds we attribute to bathymetric effects, in particular a large scour hole at that location made it appear as if the front arrived further upstream first. In reality, our data across the section indicates that here the front passed first over a shallower region before progressing to the next cross section. The salt wedge frontal speed can be compared to the velocities in the shallowest ADCP bin (Figure 4.8 purple line), the bulk frontal velocity (if just the first and last crossing were considered, Figure 4.8 pink line), and the speed of a corresponding gravity current,$u_{gc} = \sqrt{g'h}$ where g', the reduced gravity, is calculated using the density difference observed at the bottom CTD at mooring e1bot, before and after the passing of the flood tide and h is the depth of the bottom water layer which is assumed to be ~1 m. It appears that the frontal propagation speed is similar to that of the ADCP currents, and faster than that of an estimated gravity current, suggesting that the front being advected with the flooding tidal currents. Interestingly, if we examine the speed over an overtopping event during the closure (gravity current without advection) we see the speed of the propagating cooler, denser water is about half that of the tidal front and similar to, but slightly faster, than the estimated speed of a gravity current (speed observed = 0.029 m/s; gravity current = 0.018 m/s).

Another significant advantage of the DTS, is that we can see how the tidal fronts propagate in the lateral direction. We consistently see the arrival of the propagating flood tide front in the shallower cross-sectional regions before the deeper regions (Figure 4.10) This is even more obvious during the propagating overtopping event (Figure 4.14). Interestingly, this seems to counteract the theory that the tide propagates in the deepest region faster or if the tides is moving around a bend, it would arrive at the inside edge before the outside edge (Kranenburg et

al., 2019). These observations raise interesting questions about the 3D spatial complexity of a propagating gravity current acting over complex bathymetry which will be important to investigate in further studies and numerical models. Without the DTS, it is likely these features would not have been observed.

4.3.2 Challenges of using a DTS cable in a dynamic inlet

Perhaps the most obvious negative aspect of a DTS cable within a tidal inlet is that it does not measure salinity. While temperature can provide useful information, especially when the ocean water and estuarine waters have large temperature gradients, measuring salinity is paramount in estuaries as salinity often dominates density and T-S relationships in estuaries are often rather complex and not predictive. To compound this issue, unfortunately, in this experiment, several of our CTD salinity measurements malfunctioned precluding additional analysis. Thus, for example, our frontal tracking could only be done at night when diurnal heating did not confound the frontal propagation signal.

Another significant challenge of the DTS cable is knowing exactly where the cable is in X, Y, and Z space. The cable, while weighted and staked down clearly still moved with the tidal currents. In bathymetrically complicated areas such as a tidal inlet, the bed can slope steeply and thus a 1 meter error in the horizontal cable location can result in a significantly incorrect depth estimate. While we used our data to deduce a method for knowing whether or not the cable is exposed (based on the assumption that we know what the cable elevation is and using the temperature variance), this method does not work for mudflats where the bed slope is low and pooling waters or small rivers may exist. Moreover, as the intertidal regions are flooding, the first few data points before the cable is sufficiently submerged often showed temperatures near air or mudflat temperatures (purple, Figure 4.5). While this data may be real and we may be

measuring a very thin layer of water, it is also possible, the algorithm for identifying cable exposure is not working because the variances are low, and the bathymetry or cable location is off by a few centimeters (or more).

Another large problem is knowing if the cable is buried. In dynamic environments like tidal inlets, significant sediment accretion and erosion can occur over the course of a tidal cycle. This can bury the cable which means we are reading porewater temperatures rather than water column temperatures. While we can often back out if it buried more than 20 cm due to a lack of variance in the temperature signal, knowing if it was buried by only a few centimeters was not possible.

An additional complicating factor is that the cable's response to black body radiation as well as bed sediment temperatures was unknown. The cable was darker than the surrounding mudflats meaning it likely heated up more than the water column when exposed to solar radiation. Additionally, we must assume the bottom water is the temperature of the top of the mudflat but our measurements would be distorted if the mudflat is cooler or warmer, or if groundwater was percolating up through the bottom.

4.4 Summary

The DTS system is a novel technology that uses the relationship of temperature and the scattering of light to provide a coherent spatial and temporal picture of the variability of bottom water temperature. The DTS enables the user to identify patterns and structures in the temperature landscape that traditional moorings would not be able to capture. Nonetheless, interpreting the cable data presents unique challenges, the primary of which is cable location (in the horizontal, vertical, and in reference to the location of the sediment bed and water surface). Additionally, concurrent salinity, velocity, and pressure measurements are required to understand

the physical processes as temperature alone in a tidal inlet may pose more questions than it answers. With these challenges, additional methodology would be needed before deploying this cable in a tidal inlet in the future. Nevertheless, the preliminary results suggest some interesting propagation features of tidal inlet salt-wedge fronts worth investigating in the future.

4.5 Figures

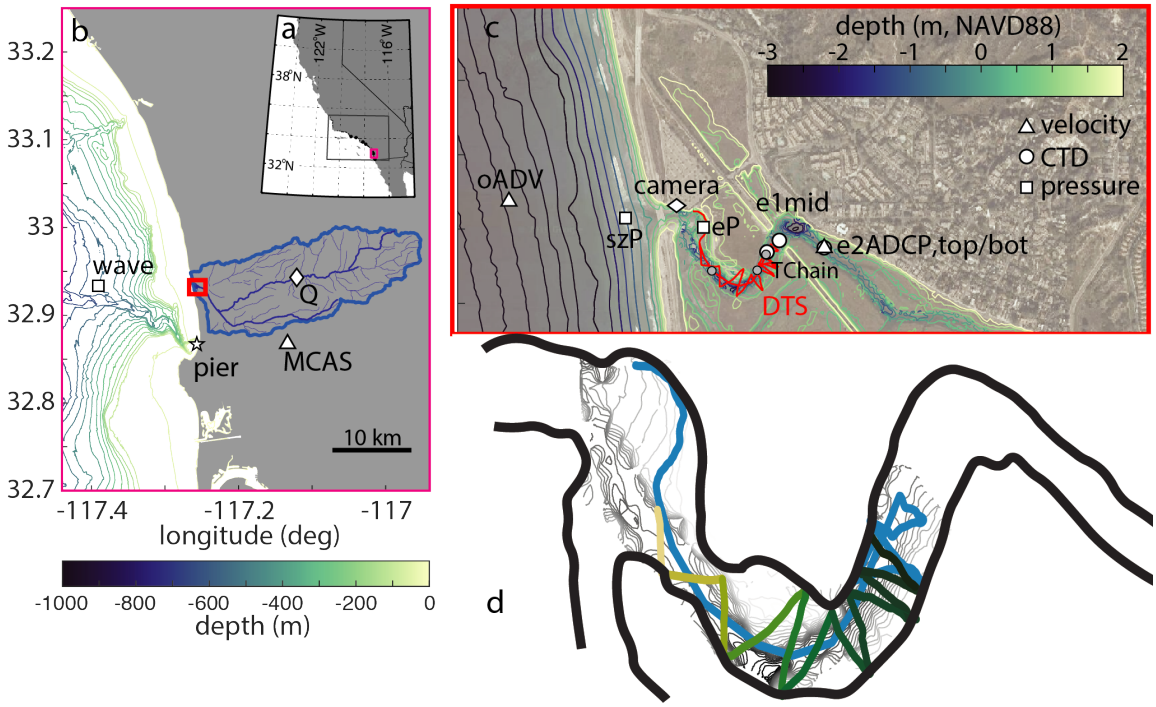

Figure 4.1: Location of Los Peñasquitos Lagoon and instruments deployed. a.) California coastline with San Diego delineated. b.) San Diego coastline with watershed of Los Peñasquitos Lagoon and offshore bathymetry. c.) Image of Los Peñasquitos Lagoon with instrument locations (white for nearly continuous measurements, gray for short-term mooring deployments, red for location of DTS) overlain on marsh topography and bathymetry in teal (light colors are higher elevation). Estuary bathymetry was collected from a combination of UAV measurements and towed ADCP measurements, while those offshore are from the 1/3 arc-second San Diego Coastal DEM model from NOAA and all are referenced to NAVD88. d.) Zoom of the bathymetry in the inlet and location of DTS. Shorter, thalweg cable in blue. Longer, zigzag cable in green. Colors of cross-sections consistent with Figures 5.8, 5.9 and 5.12. Cross sections numbered sequentially in upstream direction (crossing #1 is light green, #12 is upstream).

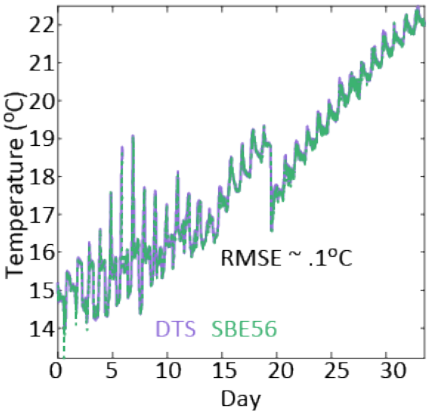

Figure 4.2: Temperature of DTS from the thalweg cable 541 m from Silixa XT instrument (purple) and co-located SBE56 (green) over the full deployment. The DTS at this location had approximately 0.1°C root mean squared error (RMSE).

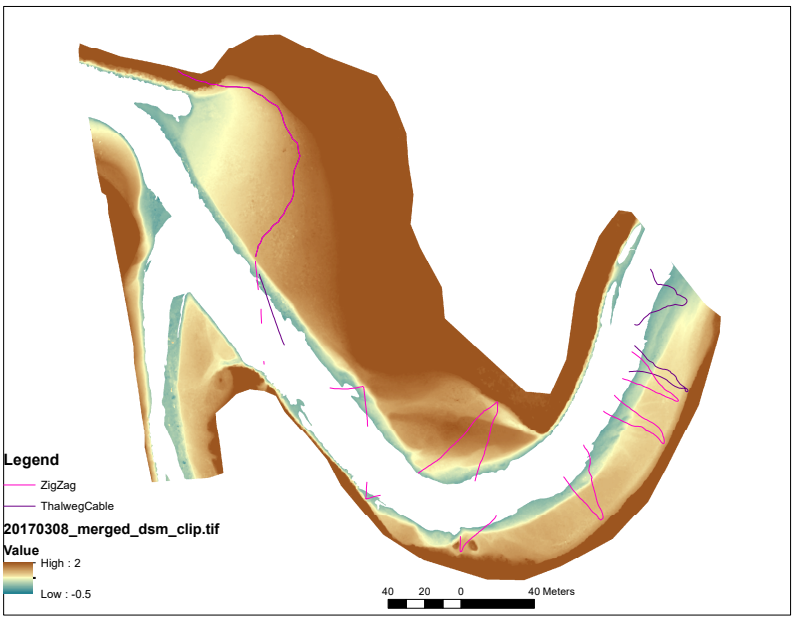

Figure 4.3: A digital elevation map of the exposed mudflats and surrounding marshlands on March 8th 2017 was constructed using structure-from-motion photogrammetry using Pix4D Mapper Pro on imagery conducted from a fixed-wing drone. The cable is visible when exposed or in shallow, clear water in the high resolution drone photographs allowing accurate placement of intertidal cable lengths in x, y, z space within the error bounds of the photogrammetric elevation map (pink is longer zigzag, cross-section, cable; purple is the shorter, mostly thalweg, cable).

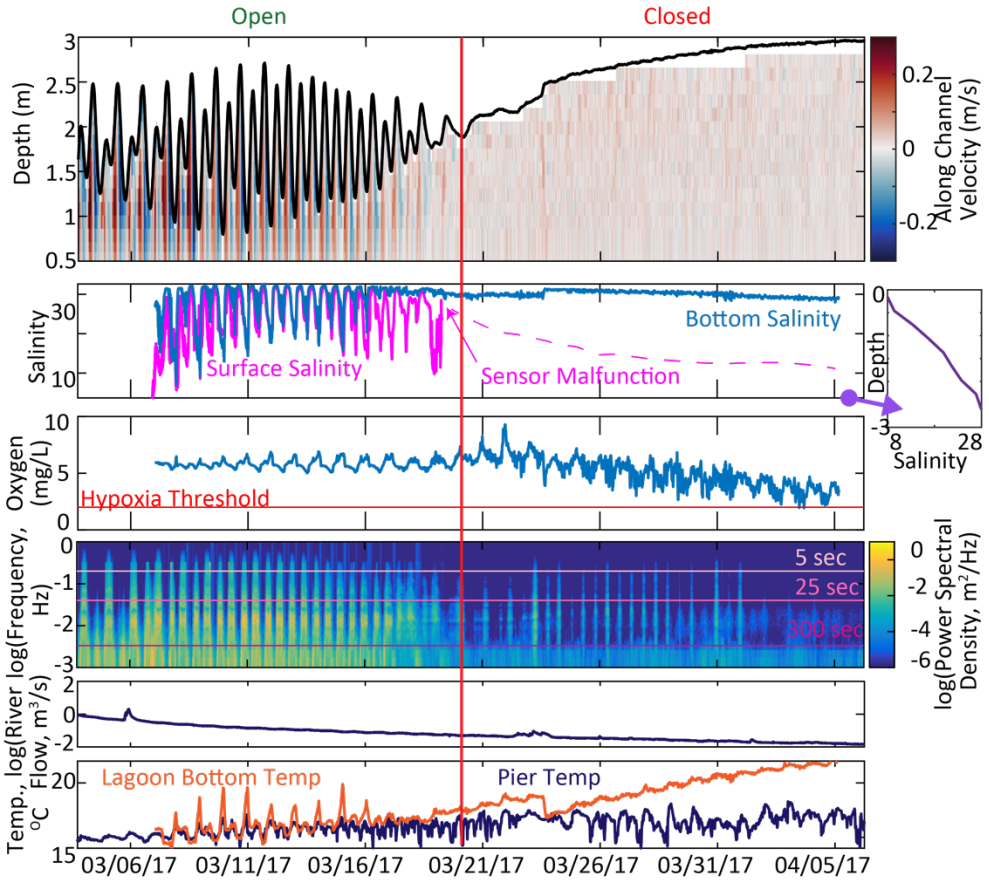

Figure 4.4: Environmental conditions during the DTS deployment. The cable was deployed for 16 days during an open period and 16 days during a closed period. The vertical red line indicates the date of complete closure. a.) Depth and water velocities at e2. Blue (red) indicates outflowing (inflowing) currents. b.) Salinity at Mooring e1. Bottom water (e1bot) salinity at the bottom is in blue; surface salinity (e1top) is in pink. Note that unfortunately the salinity sensor malfunctioned just prior to estuary closure and the dashed line shows an estimate of the surface salinity trajectory based on passed closures and individual occasional vertical CTD casts. An individual CTD cast from 06 April 2017 is shown to the right of b showing strong vertical stratification with surface salinity values as low as 8. c.) Dissolved oxygen content at e1bot. d.) Power spectral energy density at eP. eP senor was relocated into the channel on March 17, 2017 after significant accretion at the original location. e. River discharge ($\log_{10}$) measured at USGS Poway stream gauge. F.) Temperature at Scripps Pier (navy) and lagoon bottom water (orange).

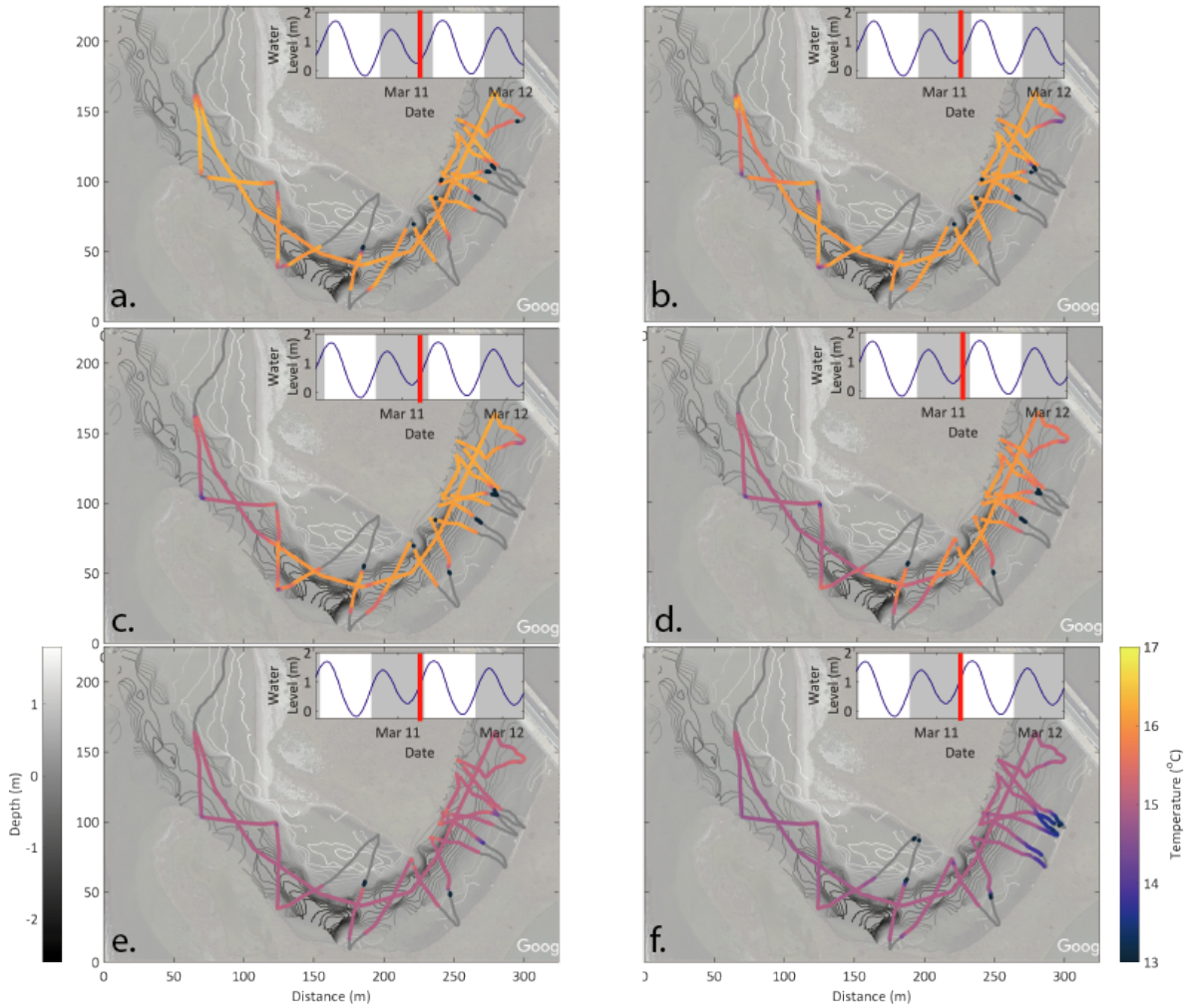

Figure 4.5: Snapshots of bottom temperature measured with the DTS during a nighttime flooding tide on March 11, 2017. Images every 30 minutes of bottom water temperature where yellow is warmer waters, purple is cooler waters. Bathymetry is contoured in gray (light gray indicates shallow water; dark gray indicates deeper water). Inset shows water level (blue line) and the day/night periods (night is gray; day is white) which each time stamp marked with a red vertical line.

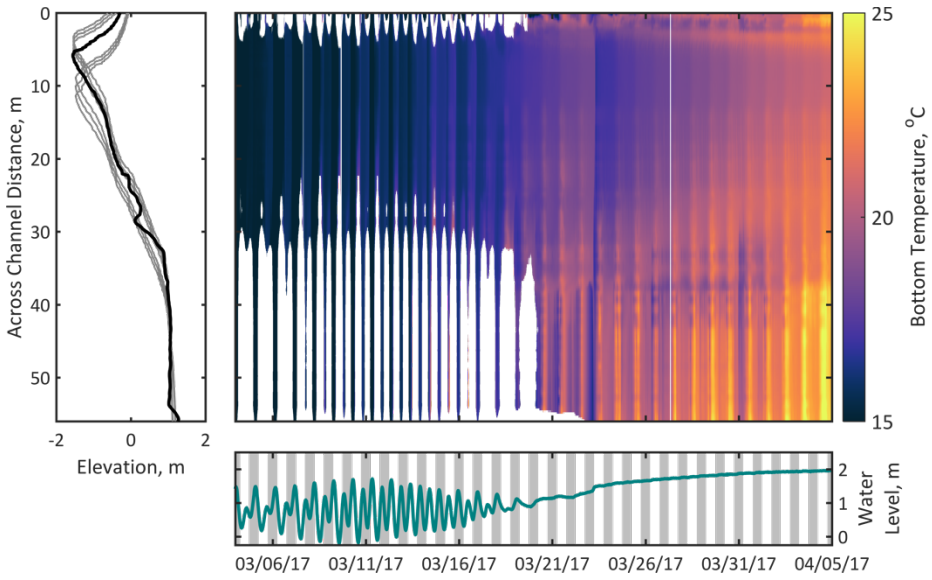

Figure 4.6: Temperature at DTS cross section #9 for entire deployment. Left panel shows bed elevation along the transect (black is the best approximation of bathymetry; gray lines indicate potential bathymetry error derived from applying a horizontal offset of 3 meters in different directions). The north side of the channel is distance = 0; the south side is distance = 60. Bottom panel shows water level (green) and time of day (gray is night; white is day) over time. Central panel shows bottom temperature across the channel (y-direction) over time (x-direction). White areas show periods when the cable is exposed. Purple is cooler water; yellow is warmer water.

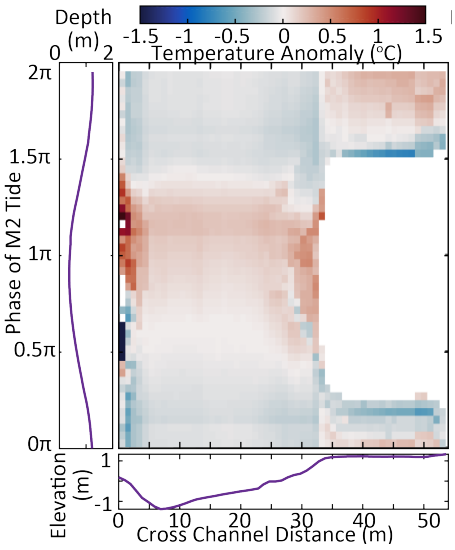

Figure 4.7: M2 phase-average of bottom water temperature at cross section #9 during the open period. Left panel indicates the phase-averaged water level with high tides on the top and bottom (~0π and ~2π) and low tide in the center (~1π). Ebbing tide is between ~0π and ~1π. Flooding tide is between ~1π and ~2π. Bottom panel is bed elevation with the north side of the channel on the left and south side of the channel on right. Middle panel shows temperature anomaly over the tidal phase (y) and cross-sectional location (x). Temperature for each location along the cross-section is phase-averaged and the time average temperature for each location along the cross section is removed to form a phase averaged temperature anomaly. Red indicates warmer than average temperatures for each cross-distance location. Blue indicates cooler than average temperature.

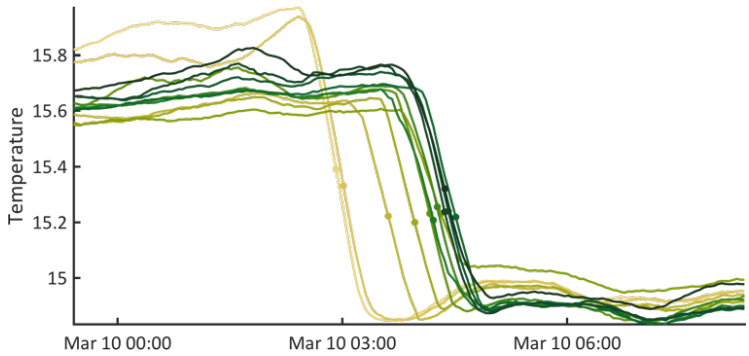

Figure 4.8: Arrival of flooding salt-wedge front at the deepest point of each cable cross-section on March 10, 2017. Temperature at the deepest location of each cross-section over time. Light (dark) green is the cross section furthest downstream (upstream) such that the color shade darkens with distance upstream. The front arrival time (for analysis purposes), or time of the maximum temperature change, is shown by colored dots for each cross-section.

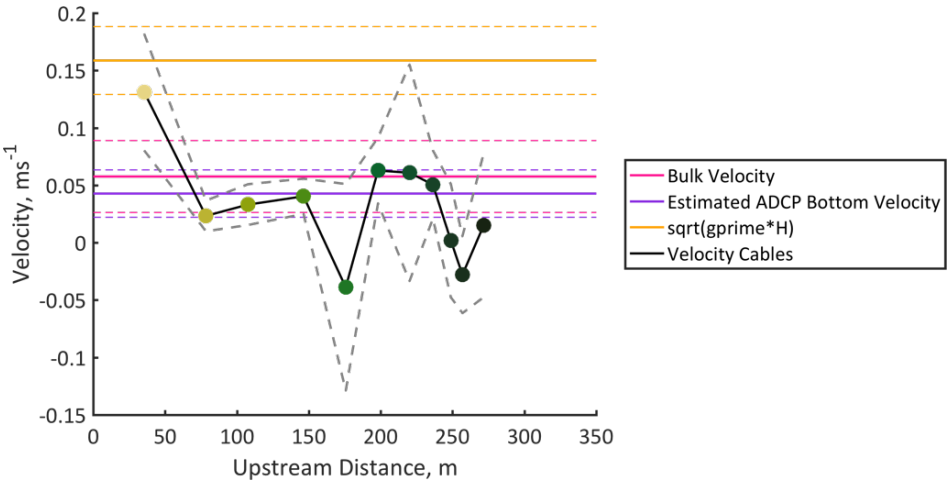

Figure 4.9: Flooding front speed calculated based on cross-section spacing and the cool water arrival times between each adjacent cross-section (Figure 4.8, dots). As in Figure 4.8, darker green colors are further upstream (see x axis). Bulk velocity (pink) is based on the difference between the arrival time and distance of the most upstream and most downstream crossings. Purple shows the velocity from the ADCP when the cool water reaches e2. Yellow is an estimated gravity current speed.

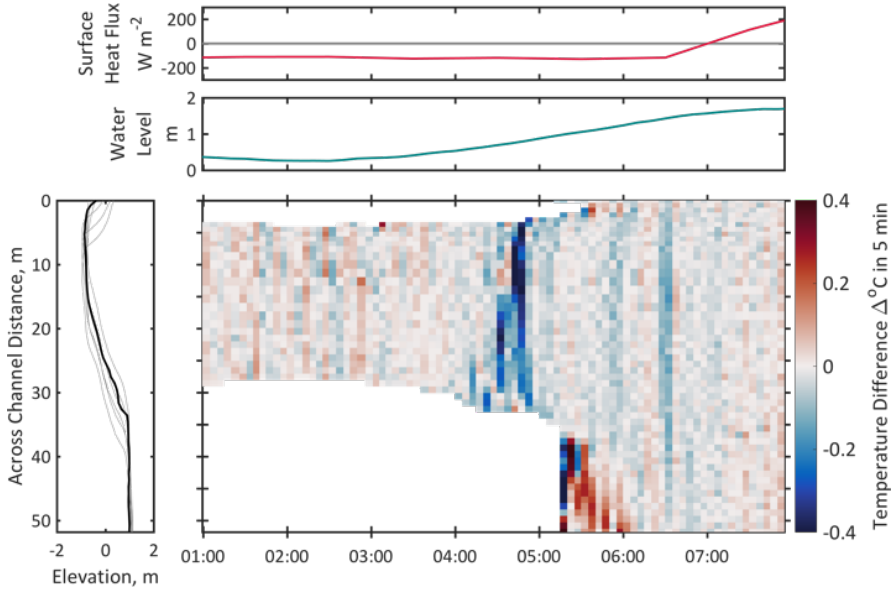

Figure 4.10: Temperature change at DTS cross section #11 during an open period, flooding tide (March 11 2017) over 7 hours. Left panel shows bed elevation along the transect (black is the best approximation of bathymetry; gray lines indicate potential bathymetry error derived from applying a horizontal offset of 3 meters in different directions). The north side of the channel is distance = 0; the south side is distance = 60. Top panel shows surface heat flux (red) calculated using the bulk heat budget described in Section 5.3.5. Second panel shows water level (green). Middle-right panel shows the time difference of bottom temperature over 5 minutes for each cross section location (y-direction) over time (x-direction). Blue (red) indicates the water at a given time and location is cooling (warming). The cooling appears earlier in time on the channel slope than in the thalweg.

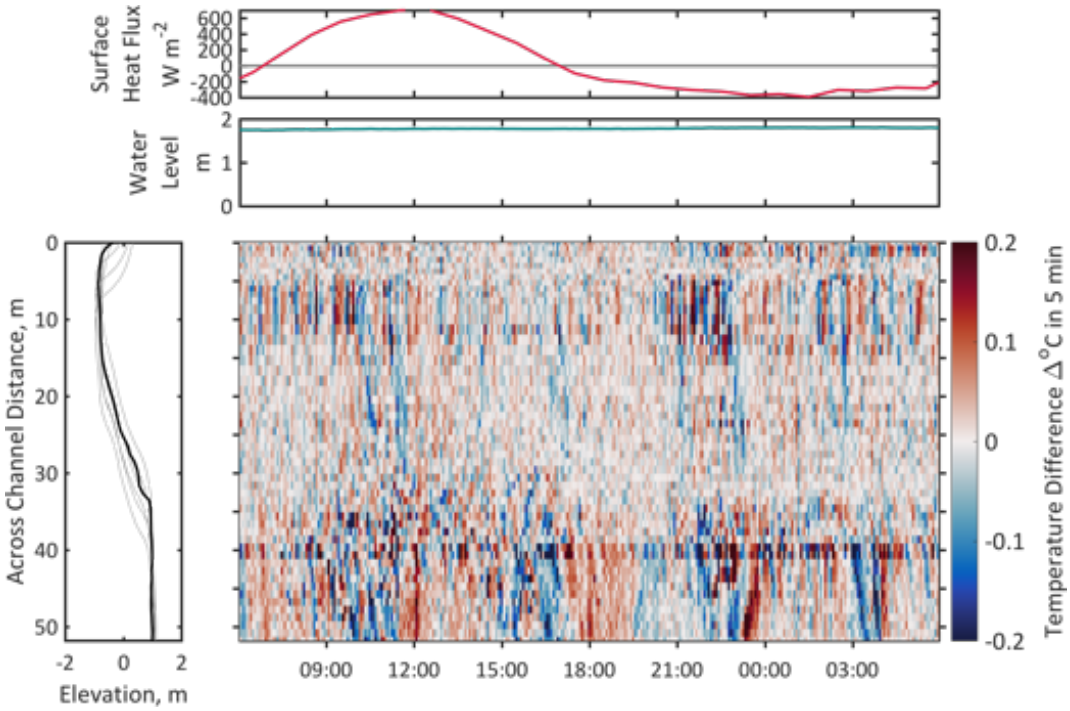

Figure 4.11: Temperature change at DTS cross section #11 during the closed period (March 29 2017) over 24 hours. Left panel shows bed elevation along the transect (black is the best approximation of bathymetry; gray lines indicate potential bathymetry error derived from applying a horizontal offset of 3 meters in different directions). The north side of the channel is distance = 0; the south side is distance = 60. Top panel shows surface heat flux (red) calculated using bulk heat budget. Second panel shows water level (green). Middle panel shows bottom temperature difference over 5 minutes for each cross section location (y-direction) over time (x-direction). Blue (red) indicates the water at a given time and location is becoming cooler (warmer).

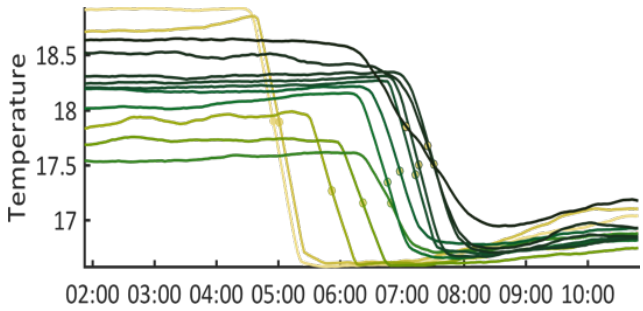

Figure 4.12: Flooding front arrival at the deepest point of each cross section location along the cable during overtopping event on March 23rd, 2017 (similar to Figure 4.8, but during closed conditions).

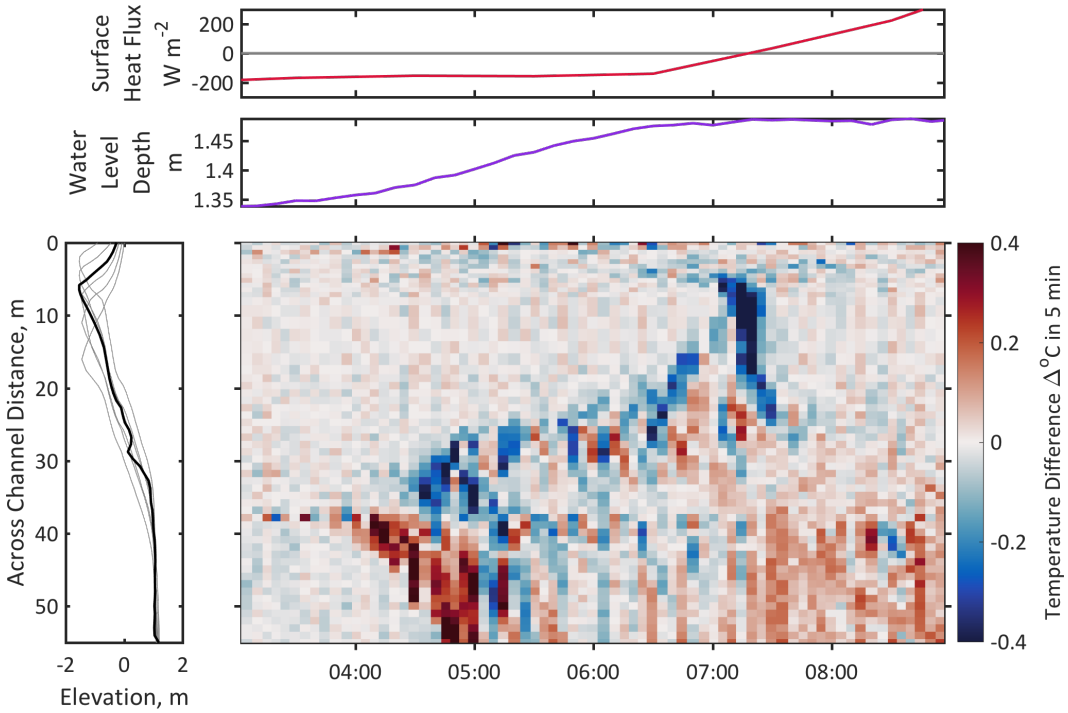

Figure 4.13: Temperature change at DTS cross section #10 during an overtopping event during the closed period (March 23 2017) over 6 hours. Similar to Figure 4.10.

4.6 Acknowledgements

Chapter 4, in part is currently being prepared for submission for publication of the material. Harvey, Madeleine E.; Giddings S. N. Pawlak G.; Crooks, J; Davis, K. The dissertation author was the primary investigator and author of this material.

Chapter 5

Effects of Elevated Sea Levels and Waves on Southern California Estuaries during the 2015-2016 El Niño

The 2015-2016 El Niño provided insight into how low-inflow estuaries might respond to future climate regimes, including high sea levels and more intense waves. High waves and water levels coupled with low rainfall along the Southern California coastline provided the opportunity to examine how extreme ocean forcing impacts estuaries independently from fluvial events. From November 2015 to April 2016, water levels were measured in 13 Southern California estuaries, including both intermittently closed and perennially open estuaries with varying watershed size, urban development, and management practices. Elevated ocean water levels caused raised water levels and prolonged inundation in all of the estuaries studied. Water levels inside perennially open estuaries mirrored ocean water levels, while those inside intermittently closed estuaries (ICEs) exhibited enhanced higher-high water levels during large waves and tides were truncated at low tides due to a wave-built sand sill at the mouth, resulting in elevated detided water levels. ICEs closed when sufficient wave-driven sand accretion formed a barrier berm across the mouth separating the estuary from the ocean, the height of which can be estimated using estuarine lower-low water levels. During the 2015-2016 El Niño, a greater number of Southern California ICEs closed than during a typical year and ICEs that close annually experienced longer than normal closures. Overall, sill accretion and wave exposure were important contributing factors to individual estuarine response to ocean conditions. Understanding how estuaries respond to increased sea levels and waves and the factors that influence closures will help managers develop appropriate adaptation strategies.

5.1 Introduction

Estuaries and associated wetlands provide extensive ecosystem functions and services, including biodiversity support, carbon sequestration, water quality improvement, and flooding abatement (Zedler and Kercher 2005; Takekawa et al. 2011; Holmquist et al. 2018). Under climate change, it is important to understand how such systems will respond and adapt. In particular, the balance between wetland resiliency to local sea-level rise and their role in mitigating the effects of sea-level rise is not well-understood (Shepard et al. 2011). This is especially true in traditionally under-researched systems such as low-inflow estuaries. Low-inflow estuaries are found worldwide (e.g., Australia, South Africa, Portugal, Spain, Morocco, Chile, Mexico, and the United States; Largier 2010) and receive smaller and more episodic freshwater inputs than their "classical" counterparts found in wetter climates with larger watersheds (Largier et al. 1997; Ranasinghe and Pattiaratchi 2003; Behrens et al. 2013; Rich and Keller 2013; Williams and Stacey 2016).

In Southern California, all estuaries are low-inflow estuaries and are threatened by both continued urbanization and climate change. More than 100 estuaries line the highly urbanized Southern California coastline (Figure 5.1 and Doughty et al. 2018), all with varying degrees of physical modifications, including the damming and channelizing of river inflows; the construction of breakwaters and jetties at inlets; the dredging of channels, inlets, and harbors; the construction of roads splitting systems; and the direct filling of wetlands (e.g., Pratt 2014; Los Peñasquitos Lagoon Foundation et al. 2016). Despite these threats, these systems are extremely important to the regional economy and ecology (Zedler and Kercher 2005; California Natural Resources Agency 2010).

In general, low-inflow estuaries along coasts with strong wave conditions are bar-built estuaries affected by the presence of a wave-built bar/sill, and subject to mouth closure. In bar-

built estuaries, low-tide water levels are typically perched above ocean water levels even when the mouth is open, due to hydraulic or frictional control exerted by the shallow sill found in the mouth or immediately landward (i.e., the flood tide shoal). Water drains slowly from the estuary until the ocean water level rises again above the sill elevation (e.g., Williams and Stacey 2016). While waves can transport and deposit sediment in the estuary mouth, strong tidal exchange and/or river discharge scours the inlet channel and exports sediment from the mouth. With low or intermittent river outflow and/or small watersheds and tidal areas, wave-driven sediment accumulation can exceed tidal/fluvial erosion leading to the formation of a sill or barrier berm at the estuary mouth that separates the estuary from the ocean (e.g., Largier et al. 1992; Elwany et al. 1998; Morris & Turner 2010; Behrens et al 2011; Behrens et al. 2013; Rich & Keller 2013; Orescanin & Scooler 2018). A common feature globally, estuaries that close intermittently have been referred to by many names (Tagliapietra et al. 2009), including intermittently closed and open lakes and lagoons (ICOLL, Roy et al. 2001), temporarily opening and closing estuaries (TOCE, Whitfield 1992), intermittently open estuaries (IOE, Jacobs et al. 2010), intermittently open/closed estuaries (IOCE, McSweeney et al. 2017), as well as intermittently closed estuaries (ICE, Williams & Stacey 2016), the latter we use here.

In developed regions such as Southern California, many ICEs fail to re-open naturally due to adjacent beach nourishment (Ludka et al. 2018), reduced tidal prism, structurally impeded inlet migration, and altered fluvial inputs (Hastings and Elwany 2012). This results in environmental concerns, including flooding of low-lying development, undesirable water quality and impacts to fish and other marine organisms that require management attention (Largier et al 2019). Many Southern California ICEs are managed to maintain an open state through dredging, building hard structures to prevent sedimentation and enhance scour, or some combination of

methods that functionally convert these ICEs to perennially open estuaries (POEs). As communities and coastal managers develop plans for addressing sea-level rise and restoration programs (e.g., San Elijo Lagoon Conservancy and AECOM 2016; Los Peñasquitos Lagoon Foundation et al. 2017; Southern California Wetlands Recovery Project 2018; Largier et al. 2019), there remain several critical questions as to how these systems will respond to rising sea levels and a changing climate, including if marsh accretion rates will keep pace with sea level and how elevation and formation of barrier berms will change. Recent work has begun to address these questions (Doughty et al. 2018; Thorne et al. 2018), but many issues such as future flooding and water quality depend on whether ICE closures will become more prevalent in the future and how communities and managers will respond.

The 2015-2016 El Niño provided an opportunity to assess how low-inflow estuaries might respond to climate change, as El Niño conditions mimic climate-change effects including sea-level rise and intensified wave events (e.g., Bromirski et al. 2003; Ludka et al. 2016; Barnard et al. 2017; Cayan et al. 2008; Cai et al. 2014). During the 2015-2016 winter, ocean water levels were persistently above average (Young et al. 2018) due to a combination of large-scale atmospheric forcing, thermal expansion effects, storm surge, and large wave events (e.g.., Enfield and Allen 1980; Chelton and Davis 1982). The sea level anomaly at the La Jolla tide gauge during the 2015-2016 El Niño was comparable to the amount of sea-level rise likely to occur by 2030 (Griggs et al. 2017), although other estimates suggest that these sea-level rise conditions may occur sooner (e.g., Sweet et al. 2017). Anomalously large waves recorded during the 2015-2016 winter along the Southern California coast (Flick 2016; Ludka et al. 2016; Barnard et al. 2017; Young et al. 2018) is consistent with prior El Niño events (Bromirski et al. 2003). Young et al. (2018) described that, although modeling suggests that storm tracks are

projected to shift pole-ward resulting in decreased waves in sheltered regions of the Southern California Bight (e.g., Graham et al. 2013; Erikson et al. 2016), there is nonetheless likely to be an increase in extreme water level events due to rising seas alone in Southern California (Tebaldi et al. 2012; Sweet and Park 2014). At the same time as sea levels were high and wave events were more intense than normal, precipitation was near or below average in Southern California for the 2015-2016 winter (e.g., Lee et al. 2017; Siler et al. 2017). The combination of high ocean water levels, large waves, and low rainfall totals provided an opportunity to examine how climate-change-like anomalous ocean forcing impacts estuaries independently from fluvial events.

Previous work by Young et al. (2018) and Barnard et al. (2017) focused on how the anomalous 2015-2016 El Niño ocean water levels impacted coastal erosion. Young et al. (2018) specifically addressed morphology of cliffs, beaches, and estuary mouths; finding that estuary inlets accreted over the course of the winter, but they did not examine the effects on estuarine water levels. At the same time, Goodman et al (2018) has reported on anomalous marsh flooding during the 2015-2016 El Niño without explaining how ocean forcing accounts for in-estuary conditions. Here we use regional observations from the 2015-2016 El Niño in Southern California as an opportunity to address the effect of elevated sea level and large waves on ICEs globally by identifying processes that link observed climate-change-like ocean conditions to in-estuary impacts.

We present data from 13 estuaries in Southern California in 2015-2016 to examine how anomalous ocean forcing (elevated sea level and extreme wave events) affects low-inflow estuaries. We compare the response of POEs and ICEs and examine the drivers of ICE closures. In addition to general hypotheses (e.g., water-level anomalies in estuaries simply track ocean

water-level anomalies), we address hypotheses proposed by managers/scientists at management meetings, e.g., that the presence of a sill will affect estuarine water level responses to ocean forcing, and thus open ICEs will respond differently than POEs.

5.2 Methods

5.2.1 Estuaries Studied

Measurements were conducted in 13 estuaries (Figure 5.1) of varying mouth morphology, size, marsh cover, and wave exposure along the Southern California Bight. Of these systems, six estuaries are classified as intermittently closed estuaries (ICEs): Mugu Lagoon, Malibu Lagoon, Santa Margarita Estuary, San Dieguito Lagoon, Los Peñasquitos Lagoon, and Tijuana River Estuary. Seven systems are classified as perennially open (POE). Six of those are open and/or exist as a result of mouth management including dredging and/or stabilization, Colorado Lagoon, Los Cerritos, Alamitos Bay, Seal Beach, Newport Bay, and Agua Hedionda, while one, San Diego Bay, is a naturally occurring POE (although managed through dredging and jetties). In our definition of ICE versus POE, it is important to note that most of the estuaries included here were ICEs prior to development; thus, here POE refers to estuaries whose mouths have been structurally altered (jetties, groins, revetments, etc.) to be perennially open. Some systems straddle these definitions, such as San Dieguito Lagoon where maintenance dredging in addition to engineered structures ensure the estuary remains open, in spite of significant sediment transport near its mouth and ongoing risk of closure. Nevertheless, because of large morphological changes at the mouth and the clear influence of a sill, we include San Dieguito Lagoon with ICEs. The estuaries in this study are relatively small systems (6-830 hectares, Table 5.1) with the exception of San Diego Bay (~5,000 hectares). Generally, ICEs have a higher percentage of marsh cover than POEs (Appendix A).

5.2.2 Representative Estuaries

We chose to examine how estuarine water levels were influenced by ocean conditions in four select estuaries (2 ICEs and 2 POEs) before comparing the estuary types more broadly. Tijuana River Estuary (TRE) and Los Peñasquitos Lagoon (LPL) were chosen as representative ICEs, and Newport Bay (NB) and San Diego Bay (SDB) were chosen as representative POEs. The representative sites were chosen because they do not straddle the definition of mouth state and because they have the most complete data records. Water level data for SDB, TRE, and LPL are in absolute height relative to a fixed datum (Section 3.2.1) and date back to 2005 enabling us to put the 2015-2016 winter season in a long-term context. In LPL, additional morphodynamic measurements allowed us to relate ICE water level measurements to inlet morphology changes.

5.2.3 Data Collection Techniques

5.2.3.1 Water Level Data

Coastal water level measurements (6-minute interval) were extracted from the La Jolla, Los Angeles, and Santa Monica National Oceanic and Atmospheric Administration (NOAA) tide gauges (tidesandcurrents.noaa.gov; Station IDs: 9410230, 9410660, and 9410840). Estuarine water levels were measured by various institutions as part of ongoing monitoring programs across the region, with sampling intervals ranging from 2 seconds to 30 minutes. Loggers included Teledyne RD-Instruments ADCPs (acoustic Doppler current profilers), Hobo pressure loggers, Sea-Bird CTDs (conductivity, temperature, depth), YSI 6600, EXO2 multiparameter sondes, Design Analysis Associates Inc. WaterLOG Microwave sensor, and RBR pressure loggers. Pressure sensor data were corrected for fluctuations in barometric pressure (Section 3.2.3) and converted into water depth. All available data provided by agencies during the primary study period, November 1, 2015 to April 1, 2016 were used. Additionally, to provide historical context, data collected from October 1, 2004 to December 1, 2018 in LPL, TRE, and

SDB were analyzed. Data from LPL and TRE were collected as part of the Tijuana River National Estuarine Research Reserve system-wide monitoring program (Station IDs: LPLNW and TJRBRWQ, respectively). SDB data were from a NOAA tide gauge (tidesandcurrents.noaa.gov; Station ID: 9410170). Specific estuary data collection sampling schemes, quality control choices, instruments, and locations are outlined in Appendix A.

Absolute height (relative to a fixed geodetic datum, NAVD88, m) of loggers was only known at six locations (Mugu Lagoon, Seal Beach, San Dieguito Lagoon, LPL, SDB, and TRE), where the sensor elevations were surveyed during the study period. Therefore, to provide a consistent relative datum (NAVD88, m), the mean of the higher-high estuary water levels during open inlet phases, using all available data from September 1, 2015 to May 1, 2016, were adjusted to match the mean of the higher-high water levels at the nearest NOAA tide gauge over the same period for as the available lagoon data. The tidal phasing differences between the estuary and tide gauge were preserved. Only the higher-high tide was matched because it was least likely to be affected by frictional effects (e.g., Williams and Stacey 2016). Additionally, the height of high tide in the estuary has been shown to be approximately the height of the high tide in the estuary in a similar system (Hubbard 1996). This adjustment relies on the assumption that because these estuaries are short relative to tidal excursion there is minimal set-up or tidal dampening for the average higher-high water levels (Friedrichs 2010). The calculated vertical offsets from the adjustment were tested by employing the same adjustment for the six surveyed loggers with known absolute elevation, resulting in 0.04 m, 0.01 m, 0.08 m, 0.02 m, 0.02 m, and 0.06 m offsets (Mugu, Seal Beach, San Dieguito Lagoon, LPL, TRE, and SDB respectively). Note that these errors are consistently positive (albeit very small, all < 0.08 m), suggesting a small mean estuary water-level setup relative to ocean water levels. Nevertheless, these offsets

are near the vertical error of the Spectra Precision Epoch 50 or Leica RX1200 real time kinematic network rover (RTK GPS) surveying equipment used (approximately 0.05 m although values vary with distances to base stations) and small compared to the range of average water levels for the different estuaries (Table 5.1) as well as the setup that can be experienced in small estuaries (Williams and Stacey 2016), indicating this method is appropriate for converting all water level data into the NAVD88 datum within the measurement errors.

Water levels were subsampled to 15 minutes (subsequently referred to as tidal water levels) and higher-high water levels as well as lower-low water levels were extracted. A Godin low-pass filter was used to remove tidal, diurnal and other high-frequency variability (Walters and Heston 1982; Thomson and Emery 2014). These subtidal, low-pass, filtered water levels will subsequently be referred to as "detided" water levels, so as to not provide confusion with the use of "subtidal" common in estuarine ecology, however it is important to note that only frequencies below M2 remain. In Mugu and Malibu Lagoons, the sensors were deployed above local lower-low water and were dry during the low tides. For these time periods, the low-pass filtering biased the detided estuary water level high. In the subsequent analyses, higher-high water levels are a metric to address flooding and inundation, lower-low water levels are used to assess perching at sills, and detided water levels are used to address the mean state.

Pearson's correlation coefficients (r) were computed for various parameters and assumed to be statistically significant if p was less than or equal to 0.05 (95% confidence limits). P-value calculations use effective degrees of freedom (N_{eff}) based on integral time scales (Emery and Thompson, 2004).

5.2.3.2 Wave Data

Offshore wave statistics were provided from the Coastal Data Information Program (CDIP) buoy network. Nearshore wave statistics including significant wave height and peak wave direction were extracted from the CDIP Monitoring and Prediction (MOP) System model output (O'Reilly and Guza 1993; O'Reilly et al. 2016; cdip.ucsd.edu 2017). MOP uses a numerical wave model to propagate deep-water buoy observations to the 10-m isobath approximately every 100 m in the alongshore. All hindcast data were reported hourly. The nearest MOP line to either the given NOAA tidal gauge or center of the estuary mouth was used for each respective site as labeled in Appendix A.

5.2.3.3 Atmospheric Data

Barometric data were from either the nearest NOAA tide gauge or pressure sensor deployed at the estuary as specified in Appendix A. Precipitation data were from airport stations. Weather stations are marked on Figure 5.1.

5.2.3.4 Inlet State in ICEs and Sill Elevation Measurements in Los Peñasquitos Lagoon

Mouth state (open or closed) in the ICEs was determined by examining water level records. Closures are characterized by periods without tidally varying water levels. When available, satellite imagery data from Planet.com and/or mouth imagery were used to verify mouth state.

High-resolution topo-bathymetry transects were conducted at LPL using a Spectra Precision Promark 700 GNSS real time kinematic network rover (RTK GPS) and Scripps Orbit and Permanent Array Center (SOPAC) base station (SIO5) corrections. Eleven inlet elevation surveys were conducted between November 1, 2015 and April 1, 2016. Surveys were performed manually at lower-low tides following radial transects around the curving lagoon inlet. Measurements were not collected if the water level was greater than 1 m, or if the seafloor

substrate or tidal currents inhibited data collection. Two surveys were conducted, one on the seaward side of the road embankment and the bridge that defines the inlet, and the other on the landward side of the road embankment and bridge. Surveys were objectively mapped into 8-meter cells using inverse difference weighted interpolation. The sill elevation was defined as either the average height of the seaward side or the landward side of the road embankment (see section 5.2, Figure 5.6). To determine sill changes over shorter time periods, we extracted the estuary lower-low water level as a proxy for sill height and validated it against our topo-bathymetric surveys. Imagery from time-lapse cameras installed near the mouth was used to qualitatively assess the sill migration and accretion over time.

5.3 Results

5.3.1 Ocean Conditions During 2015-2016 El Niño

Water levels off the coast of Southern California were persistently above average throughout the strong 2015-2016 El Niño (Figure 5.2a, Supplementary Figure 5.1). The maximum monthly average ocean water levels were 0.20 m, 0.20 m, and 0.21 m above the predicted levels for La Jolla, Los Angeles, and Santa Monica respectively (La Jolla in Figure 5.2a). Marked wave events occurred on several occasions through the winter (Figure 5.3) with the largest waves predominantly from the northwest; thus, the southern estuaries were more exposed to wave forcing due to the coastline geometry and the effect of islands within the Southern California Bight (Figure 5.1).

Maximum detided ocean water levels during the study period occurred during extreme wave events and were 0.31 m, 0.30 m, and 0.31 m above the NOAA predicted detided water levels for La Jolla, Los Angeles, and Santa Monica respectively (Figure 5.2a). Winter coastal water levels were positively correlated with the Godin filtered significant wave heights (r= 0.39,

0.33, 0.28; p = 0.04, 0.06, 0.13 with 1.2, 1.3, 1.1 day lag of waves behind water levels) and negatively correlated with the barometric pressure (r= -0.72, -0.67, -0.73; p < 0.01, <0.01, <0.01 with 0.0, 0.2, 0.2 day lag of barometric pressure behind water levels).

At the San Diego Airport there were 3 precipitation events with 2 day rainfall totals over 10 mm (Figure 5.2d), below the average of 5.8 precipitation events per year from 1939-2018, consistent with other precipitation gauges in coastal Southern California. The total precipitation at San Diego Airport during the winter of 2015-2016 was about 21 percent below average (40th percentile of the winter historical rainfall totals from 1939 to 2018) (ncdc.noaa.gov, Station ID: USW00023188). This lower than average mean rainfall and rainfall events is consistent with rainfall patterns throughout Southern California during the 2015-2016 winter (e.g., Lee et al. 2017; Siler et al. 2017).

5.3.2 Estuary water levels

5.3.2.1 Representative POEs: San Diego Bay and Newport Bay

During the 2015-2016 winter, the tidal water levels in SDB and NB (Figure 5.3a) were strongly correlated with the ocean water levels (r > 0.99, p< 0.01 and r > 0.99, p< 0.01) for both SDB and NB; Table 5.1). The detided water levels (Figure 5.3b) were also strongly correlated with ocean detided water levels for SDB and NB (r=0.98, p < 0.01 and r =0.98, p< 0.01, respectively). The strong, significant correlations between ocean and estuarine water levels in SDB during the 2015-2016 winter were consistent with those found in a historical comparison of tidal (r > 0.99, p< 0.01) and detided (r=0.94, p< 0.01) water level data from 2005 to 2018 (Figure 5.4 c-d).

5.3.2.2 Representative ICEs: Tijuana River Estuary and Los Peñasquitos Lagoon

In both TRE and LPL, sills comprised of sand and cobbles grew over the 2015-2016 winter and restricted flow or closed the respective inlets for brief periods of time (Figure 5.6 and discussed further in Sections 4.3 and 4.4). During the open states, hydraulic and frictional control at the sills contribute to truncated lower-low water levels (see Figure 5.3a for LPL, red line relative to grey) and to elongated ebbs (Figure 5.3a and Figure 5.4a). The sills resulted in reduced maximum tidal ranges (1.55 m and 1.37 m, for TRE and LPL respectively) compared with ocean ranges (2.56 m at La Jolla) and contributed to lower, yet significant, correlations between ocean and estuarine water levels when the estuary mouth was open ($r=0.77$, $p< 0.01$, and $r=0.64$, $p< 0.01$; Table 5.1). As a result of the lower-low tide truncation and perching, detided water levels in TRE and LPL (Figure 5.3b) were not strongly correlated with detided ocean water levels during the winter observation period, even when restricting the analysis to only open periods ($r =0.57$, $p=0.09$; $r=-0.26$, $p=0.50$ for all periods; $r=0.64$, $p=0.09$, $r=0.62$, $p=0.06$ for open periods for TRE and LPL, respectively; Table 5.1). During large wave events, entrance sills accreted causing truncated (i.e., higher) tidal low-water levels, resulting in elevated detided water levels and thus a decoupled and not statistically significant (at the 95% confidence level) response to ocean water levels (Figure 5.4b). These trends were consistent with those found in a historical analysis of water level data in TRE and LPL (2005-2018, see Figure 5.4b and 4c). In both systems the open-period tidal water levels were less correlated than those in SDB ($r=0.74$, $p< 0.01$; $r=0.38$, $p< 0.01$, for TRE and LPL, respectively) and the detided water levels were not correlated ($r=0.48$, $p=0.06$; $r=0.09$, $p=0.39$, for TRE and LPL, respectively).

5.3.2.3 Comparison of Water levels in ICEs and POEs

Results from all 13 estuaries are consistent with observations from the representative estuaries: tidal water levels in the POEs are more strongly correlated ($0.92<r<1.00$; $p< 0.01$) with the ocean water levels than the ICEs ($-0.03<r<0.86$; $0.0<p<0.89$ for all periods; $0.16<r<0.87$; $p< 0.01$ for open periods) (Table 5.1 and Figure 5.4a). Subtidal water levels for the observation period were highest in the ICEs that closed; followed by the ICEs that remained open for the study period, with the POEs maintaining the lowest mean water levels (Figure 5.3b, Table 5.1). In Mugu and Malibu, the sensors were dry at the low tides causing the average water levels to be biased high. During open periods, most of the ICE detided water levels had a higher variance than POE detided water levels (Table 5.1, Figure 5.3b). Moreover, most ICE detided water levels were not significantly correlated (at the 95% confidence level) with ocean water levels (Table 5.1, Figure 5.4b) suggesting that detided ICE water levels had a decoupled response due to elevated tidal low-water during large wave events and high ocean water levels.

Higher-high water level deviations from the ocean (estuary higher-high water minus ocean higher-high water level) are plotted against significant wave heights at the closest MOP lines to the estuary mouths to assess additional water level setup or setdown within the estuaries when the mouths are open (Figure 5.5, similar to Williams and Stacey 2016, Figure 5.5e). In the POEs, there is no significant relationship between wave height and higher-high water level deviation from the ocean ($r = -0.13$, $p =0.49$), while in the ICEs, there is a clear relationship ($r = 0.52$, $p =0.002$). It is important to note that Figure 5.5 includes the higher-high water correction to NAVD88 explained in Section 3.2.1. Therefore the absolute elevation differences may be offset upwards along the y-axis relative to Figure 5.5 (upwards because of the persistent positive mean higher-high water level difference found for all sensors with known absolute elevation). However, it is important to note that repeating Figure 5.5 with absolute

elevation (for those estuaries for which it exists), the higher-high water level differences remain negative during low wave conditions, although vertical survey errors and varying distance upstream of the sensor locations complicate these results.

5.3.3 Inlet Closures in ICEs

During complete inlet closures, water levels in ICEs increased because the sill blocked outflows while inflows from freshwater upstream continued (Figure 5.7). In addition, in some circumstances, wave overtopping contributed to increased water levels behind the sill which we can deduce from time-lapse imagery and high frequency pressure measurements (not shown). During the observation period, Malibu Lagoon was closed for 30 days and naturally reopened; LPL was closed for 36 days, naturally reopened once, but closed again and was mechanically breached three times; TRE was closed for 13 days (starting at the end of the study period) and was mechanically breached; Santa Margarita Estuary was closed for 44 days and naturally reopened (Figure 5.3b).

5.3.4 Sill Elevation Changes over Time in Los Peñasquitos Lagoon

For the LPL mouth, we have morphology data which show that LPL experienced 0.5 to 2 meters of accretion (Figure 5.6) in the inlet region over the course of the winter season, in addition to nearly 1 m of erosion of a man-made embankment protecting the estuary marsh further upstream. Although measurements were not taken at a high-enough frequency to capture changes on the time scales of tides or storms, time-lapse imagery and in-person observations show that the channel migrated between hardened structures and that the sill migrated within the inlet area (Figure 5.6a and 6b) and changed elevation throughout the study period. Importantly, imagery indicates that inlet accretion occurred episodically and typically coincided with periods of large offshore waves (consistent with Behrens et al. 2013).

From the morphological data, we can track the elevation of the beach constricting flow through the mouth seaward of the road embankment as well as the elevation of the flood-tide shoal landward of the road embankment (described in Section 3.2.4 and indicated on Figure 5.6). These data show that the average elevation of the controlling sill, whether on the landward (estuary) or seaward (beach) side of the road embankment, was well represented by day-to-day changes in the lower-low water level. Before the closure, the elevation landward of the road embankment (dark blue in Figures 5 and 6) best matched this metric (with the exception of a survey immediately following a large flushing event). However, during the closure, the elevation seaward of the road embankment (light blue in Figures 6 and 7) more closely matched the lower-low water level. Overall, the average sill elevation measured by the topo-bathymetric surveys (taken at the appropriate location) matched the estuary lower-low water level with statistical significance (Figure 5.7b; $r=0.92$, RMSE = 0.16 m, $p<0.05$).

5.4 Discussion

5.4.1 El Niño and Implications to Future Conditions

During the 2015-2016 El Niño, elevated ocean water levels (Figure 5.2a), large wave events (Figure 5.2b), and low precipitation (Figure 5.2d) along the Southern California coast provided the opportunity to understand how low-inflow estuaries respond to oceanic forcing. The coastal water levels were weakly correlated with the low-pass filtered significant wave heights (Figure 5.2b) and more strongly correlated with the barometric pressure (Figure 5.2c). The high correlation with barometric pressure was likely due to a combination of the effects of storm surge, waves, and changes to local offshore winds and currents caused by local storms. High coastal California water levels caused elevated estuarine water levels resulting in an increased frequency of inundation of tidal wetlands during the El Niño (Goodman et al. 2018). As extreme

coastal water level events are likely to increase in the future (Tebaldi et al. 2012; Sweet and Park 2014), as discussed in the introduction, it is expected that low-inflow estuaries will also experience more extreme water level events in the future. The analyses provided here may provide some insights into how these estuaries in Southern California, and low-inflow estuaries around the world (Largier et al. 1996) might respond to future conditions.

5.4.2 Morphodynamics in ICEs

Significant morphological changes near the mouth were observed in most of the ICEs during the observation period. In LPL we found that significant accretion occurred and that we could use lower-low water levels to approximate sill elevation changes over time. As such, we can use the lower-low water level to examine the interactions between sill height and ocean events. Through comparisons with imagery, site visits, and surveys, we found that (with the exception of one survey following an unusually large flushing event), when the system was open or constricted, the lower-low water level more closely matched the average height of the landward, estuary area (dark blue in Figures 5 and 6), while during the closure, the average height of the seaward, beach area (light blue in Figures 5 and 6) more closely matched the lower-low water level. This is attributed to the sill location moving westward past the constriction caused by the manmade berm and bridge. The lower-low water levels at the other studied ICEs (and available imagery) show that morphological changes occurred in most of the ICEs studied.

Enhanced sill accretions and more frequent and persistent closures were observed in ICEs in Southern California during the 2015-2016 El Niño season. Los Peñasquitos Lagoon closed for more days than it had in the past 25 years (Young et al. 2018 which builds off a historical record of closure frequency in Hastings and Elwany 2012). Additionally. the Tijuana River Estuary, which closed for the first time since the previous large El Niño in 1982-1983 (Ludka et al. 2016;

Young et al. 2018). The anomalous closures can be attributed to the anomalously large wave conditions coupled with anomalously low precipitation (as expected from e.g., Behrens et al. 2013; Rich and Keller 2013). In both LPL and TRE, multi-year water level records indicate that sill heights (applying the lower-low water metric) generally increased during large wave events and decreased during significant flushing events. Additionally, years with larger wave events had higher estuarine water levels, higher sills, and more closure days (Supplementary Figure, 2). Unfortunately, sparse data and periodic dredging precluded further analysis. In the four southern ICEs, the sill heights increased during the largest wave events of the study period. Large waves and the alongshore migration of beach nourishment sand (Ludka et al. 2018) are likely responsible for the 2016 closure at TRE. Both TRE and LPL were artificially breached during the 2015-2016 El Niño; had the systems not been breached, the water levels in the systems would have been elevated for an even longer period.

5.4.3 Comparison of ICEs and POEs

Comparative analyses of different low-inflow estuaries are relatively rare with the exception of a few recent studies (e.g., McSweeney et al. 2017; Goodman et al. 2018; Clark and O'Connor 2019) and are complicated by system-specific dynamics and human alterations. Comparing water levels across a range of estuaries experiencing similar oceanic and upstream forcing over the same timeframe has allowed us to further our understanding of how ICEs and POEs respond to ocean water level events. The detided water levels in POEs mirrored ocean water levels both in mean water level and variance while the detided water levels in ICEs were higher on average and had a higher variance than ocean water levels. The mean water levels in the ICEs were higher because the sill height at the ICE mouths dictates the lower-low water level and thus elevates the detided and average water levels in these systems. The higher variance of

the ICE detided water levels is caused by the sill blocking off low tides and reducing the range of tidal water levels within the estuary. This results in extreme water level events and spring-neap variability being more pronounced (relative to the mean water level) in the detided water levels in the ICEs than they are in POEs. The sill height changing over time further increases the variability of the tidal and detided water levels. Overall, ICEs have a more decoupled response to high ocean water levels than POEs, a result that our data suggests is largely due to mouth morphology, and to a lesser extent, geometry, including system size, depth, and marsh area (Friedrichs 2010). Assessing and decoupling contributions from the different components of the total water level (e.g., waves versus barometric pressure versus longer term elevated ocean water level effects versus river flow events) were difficult. Historical data from LPL and TRE indicate that flooding plays an important role in the water level in ICEs as water levels were high during large river flow events (Supplementary Figure 5.2).

Discerning the effects of marsh extent and mouth morphology with this limited dataset is challenging because in Southern California, ICEs are generally more natural systems with higher percentages of marsh while POEs are generally more heavily managed and channelized (Appendix A). The overall trends seen in Figure 5.3b are consistent with the hypothesis that the percentage of marsh extent impacts water levels inside of these estuaries. However, in a direct comparison between estuaries with similar percentages of marsh habitat (e.g., Seal Beach and Mugu), it appears that mouth morphology (i.e., the presence/absence and size of a sill) plays a more important role in setting the mean estuarine water levels.

Data from the El Niño shows that, detided water levels in ICEs increase more than detided water levels in POEs during large wave events (Figure 5.3). Historical data at LPL, TRE, and SDB indicate that higher water levels in ICEs occurred more commonly during periods of

large waves than during periods of high ocean water level anomalies suggesting wave-driven sill accretion (e.g., Ranasinghe et al. 1999; Behrens et al. 2013; Rich and Keller 2013) and wave setup (e.g., Malhadas et al. 2009; Williams and Stacey 2016) play an important role in ICE water levels (Supplemental Figure 5.2). The sill height generally accretes during large wave events, truncating the lower tides, which causes the detided water levels to increase. The difference between the higher-high water levels in the estuaries and the ocean show that a larger water level set-up (as high as 0.2 m, but typically much smaller) occurs in ICEs than in POEs during high wave events (Figure 5.5, similar to Williams and Stacey 2016, Figure 5e). This is also consistent with the offset error estimates (Section 3.2.1) being consistently being positive (albeit very small, all < 0.08 m), suggesting that time mean ICE higher-high water levels were slightly elevated compared with ocean higher-high water levels. Moreover, ICEs exhibit an estuarine setdown during low wave conditions, likely due to tidal amplitude attenuation in these highly frictional estuaries (Friedrichs 2010). Finally, ICEs show a positive, statistically significant linear relationship between estuarine setup and wave height, where higher-high water level in the estuary increases by 0.07 m above that of the ocean for every 1 m increase in wave height ($r = .52$, $p = 0.002$), while POEs do not (Figure 5.5).

The geographical location of ICE and POEs complicates the assessment that ICEs have more enhanced detided water levels and setup than POEs during large wave events because the geometry of the Southern California Bight (Cao et al. 2018) dictates the amount of wave energy (MOP wave roses, Figure 5.1) and the peak wave direction at the estuary mouth. Nearly all POEs are to the north, where the waves at their mouths were smaller during this study due to regional shadowing. The only POE exposed to large waves is Agua Hedionda where a shorter dataset unfortunately limits the number of large wave events to only one (only 1 event where $H_{sig} > 2$ m

for more than 1 hour). However, it is worthwhile to note that Agua Hedionda experienced some inlet accretion over this study period, likely resulting from its exposure to larger waves. Due to the geometry and the offshore islands of the Southern California Bight (Figure 5.1), geographic location and wave shadowing play a large role in the wave conditions seen at the estuary mouths and the water level response within the estuaries to offshore events.

5.4.4 Low-Inflow Estuary Management Implications

Managers of low-inflow estuaries (whether ICEs or POEs) want to understand how sea level rise might affect their systems (Thorne et al. 2017) to develop effective resiliency and restoration strategies (Southern California Wetlands Recovery Project 2018). The effects of sea-level rise on marshes and wetlands (e.g., changes in accretion, migration, species composition, etc.) are currently a focus of several studies (e.g., Thorne et al. 2016).

Tidal prism is an important metric for many managers because it can help maintain open inlets (Hastings and Elwany, 2012) and is important for marsh habitat. As sea levels rise, it is expected that POE water levels will increase proportionately because POE water levels mirror ocean water level fluctuations. Assuming that the bed elevations of POEs remain constant (through continued dredging and jetties), with higher sea levels, tidal prisms will increase (Holleman and Stacey 2014). In ICEs however, the effect of sea-level rise on tidal prism is complicated by mouth morphodynamics and sill height elevation changes. Therefore, continued observations of sill heights in a variety of systems may provide additional understanding to how ICEs respond to changing conditions.

Managers of these systems are also interested in how the frequency of inundation and closures will change with future conditions. During the 2015-2016 El Niño, tidal marshes in estuaries all along the west coast experienced increased inundation (Goodman et al. 2018), a

trend that is likely to continue with increased sea levels in both POEs and ICEs. During open conditions, the higher detided water levels in ICEs lead to a range of absolute elevations being inundated for longer than POEs which may impact the species that are able to thrive at those elevations (e.g., Janousek et al. 2016; van Belzen et al. 2017). Sustained high water in NB resulted in die-off of high marsh habitat that has been used previously as nesting habitat for several sensitive bird species (Dick Zembal, personal observations). If closures become more frequent, as they did during the El Niño conditions, the ICEs will experience an increased frequency of inundation of freshwater on saline habitats, hypoxic conditions (e.g., Gale et al. 2006; Cousins et al. 2010), prolonged periods of inundation at a fixed elevation, and would pose a greater risk to upstream flooding. More frequent inlet closures cause a shift from more saline marsh vegetation to more freshwater vegetation as the surface layer over the marsh is fairly fresh due to urban runoff (Los Peñasquitos Lagoon Foundation 2017). Additionally, reduced tidal prism would cause physiologically stressful conditions and a reduction of incoming marine propagules leading to changes in species composition and an overall reduction in diversity of plants and animals (Teske and Wooldridge 2001; Phillips et al. 2002; Raposa 2002; Saad et al. 2002). In Southern California, mouth closures in TRE and LPL resulted in hypoxia and subsequent fish kills within days (Crooks, personal observations). The risk for upstream flooding and inundation - including nearby infrastructure - increases during closures as the estuaries slowly fill due to urban runoff, precipitation, riverflows, and wave overtopping (Largier et al. 2019).

Low-inflow estuaries in Southern California, and around the world, are all managed by different entities with varying priorities, stakeholders, and economic and ecological values (e.g., Zedler and Kercher 2005; Adams 2014; Pratt 2014; McSweeney et al. 2017). As different

management entities develop resiliency or restoration plans (e.g., Thorne et al. 2017) for their respective systems, they will likely take sea-level rise into account. This study demonstrates that water level response (and therefore appropriate management strategies) will vary by system. In more perennially open systems, it is expected that the water levels near the mouth will continue to match ocean water levels with upstream water levels depending on the geometry, bathymetry, and armoring in the system (e.g., Holleman and Stacey 2014). Although, even in some of the POEs (e.g., Agua Hedionda) inlet accretion occurs over longer time scales and could result in the water levels having a more similar response to those in ICEs. In ICE systems, the detided water level response to increased sea levels will likely be non-linearly amplified; however, more unknowns particularly with regard to wave climate, sill accretion, marsh response, and changes in tidal prism suggests resiliency plans may need to account for an array of possible futures. As these ICE systems are generally more natural, the ecological consequences of increased water levels may be greater. Managers must weigh the tradeoffs between allowing for extreme water levels and more frequent closures and the cost and impacts of management and dredging (Largier et al. 2019). The plans would also benefit from being adaptable to evolving predictions and interannual variability. For example, if water levels increase and there is a decrease in large wave events it is possible that an increased tidal prism would lead to less frequent closures. Additionally, inlet maintenance permitting agencies may wish to allow estuary managers to recognize that elevated sill height and large forecasted waves may lead to an inlet closure and provide more permitting options that enable managers to use this knowledge to schedule maintenance and dredging activity in advance.

5.5 Summary

Anomalous conditions associated with the 2015-2016 El Niño along the Southern

California coastline including elevated ocean water levels, high waves, and low precipitation, provided the opportunity to understand how low-inflow estuaries respond to oceanic forcing and insights into how they might respond to changing ocean conditions. From November 2015 to April 2016, water levels were continuously measured in 13 estuaries in Southern California providing a unique dataset. Water levels from such a wide range of systems experiencing similar forcing conditions are rarely measured simultaneously. Of the 13 systems measured, 6 were ICEs and 7 were POEs. Generally, the water levels in the POEs (tidal and detided) were more closely correlated with ocean water levels. ICE water levels exhibited weaker correlations to ocean water levels due to a sill resulting in a decoupled detided response. ICEs also exhibited a relationship between high waves and higher-high-water levels, with low wave conditions exhibiting decreased higher-high water within ICEs compared to offshore, likely due to frictional damping, and high wave conditions exhibiting increased higher-high water within ICEs compared to offshore. While estuary-specific dynamics and human modifications complicated comparisons across estuaries, our analyses suggest that large wave heights were one of the most important factors driving the ICE response which appears closely linked to changes in mouth morphology, specifically sill accretion. Results suggest that ICEs worldwide may be more susceptible to altered water levels as well as morphological changes resulting from sea-level rise and higher wave heights. A metric for sill height provides a starting point for expanded analyses and estuarine comparison, yet additional work is needed.

5.6 Tables

Table 5.1: Estuary inlet and water level (WL) summary statistics. Infrastructure at mouth, variance in low-passed water levels, standard deviation of low passed water level, average low-passed water level elevation, r and root-mean-squared error (RSME) values for measured estuaries water level vs. measured ocean water level (at nearest tide gauge) for all estuaries, and for the open-only state for ICEs that closed during this observational period. Gray shading indicates ICEs. Bold indicates statistically significant where $p<0.05$.

				Subtidal						Tidal			
						Estuary WL vs. Offshore WL				Estuary WL vs. Offshore WL			
Estuary	**Mouth State**	**Distance Upstream of Mouth**	**Estuary Size, hectares**	**WL Variance**	**Average WL Elevation**	**r**	**RMSE**	**r_{Open}**	**RMSE Open**	**r**	**RMSE**	**r_{Open}**	**RMSE Open**
Mugu	Unarmored	900 m	830	0.006 m^2	1.22 m	**0.83**	0.28	~	~	**0.86**	0.19	~	~
Malibu	Unarmored	450 m	14	0.12 m^2	1.94 m	**0.73**	0.83	-0.25	0.49	-0.03	1.06	**0.87**	0.71
Los Cerritos	Jetty	4310 m	44	0.006 m^2	0.81 m	**0.85**	0.06	~	~	**1.00**	0.06	~	~
Colorado Lagoon	Jetty	4700 m	6	0.006 m^2	0.95 m	**0.94**	0.06	~	~	**0.93**	0.19	~	~
Alamitos Bay	Jetty	4300 m	236	0.010 m^2	0.87 m	**0.89**	0.05	~	~	**0.97**	0.13	~	~
Seal Beach	Jetty	3300 m	406	0.005 m^2	1.01 m	**0.94**	0.04	~	~	**1.00**	0.03	~	~
Newport Back Bay (NB)	Jetty	6000 m	655	0.008 m^2	0.91 m	**0.98**	0.03	~	~	**1.00**	0.04	~	~
Santa Margarita Lagoon	Unarmored	1100 m	116	0.062 m^2	1.47 m	-0.03	0.67	0.27	0.44	0.04	0.83	**0.16**	**-0.73**
Agua Hedionda	Jetty	750 m	140	0.003 m^2	0.88 m	**0.76**	0.07	~	~	**0.92**	0.20	~	~
San Dieguito	Unarmored	750 m	56	0.013 m^2	1.09 m	0.55	0.24	~	~	**0.73**	0.40	~	~
Los Peñasquitos (LPL)	Unarmored	750 m	96	0.119 m^2	1.44 m	-0.26	0.68	0.64	0.33	0.23	0.80	**0.64**	**0.04**
San Diego Bay (SDB)	Jetty	9900m	6050	.008 m^2	0.83 m	**0.98**	0.05	~	~	**1.00**	0.06	~	~
Tijuana Estuary (TRE)	Unarmored	900 m	224	0.011 m^2	1.11m	0.57	0.26	0.62	0.25	**0.76**	0.40	**0.77**	**0.35**

5.7 Figures

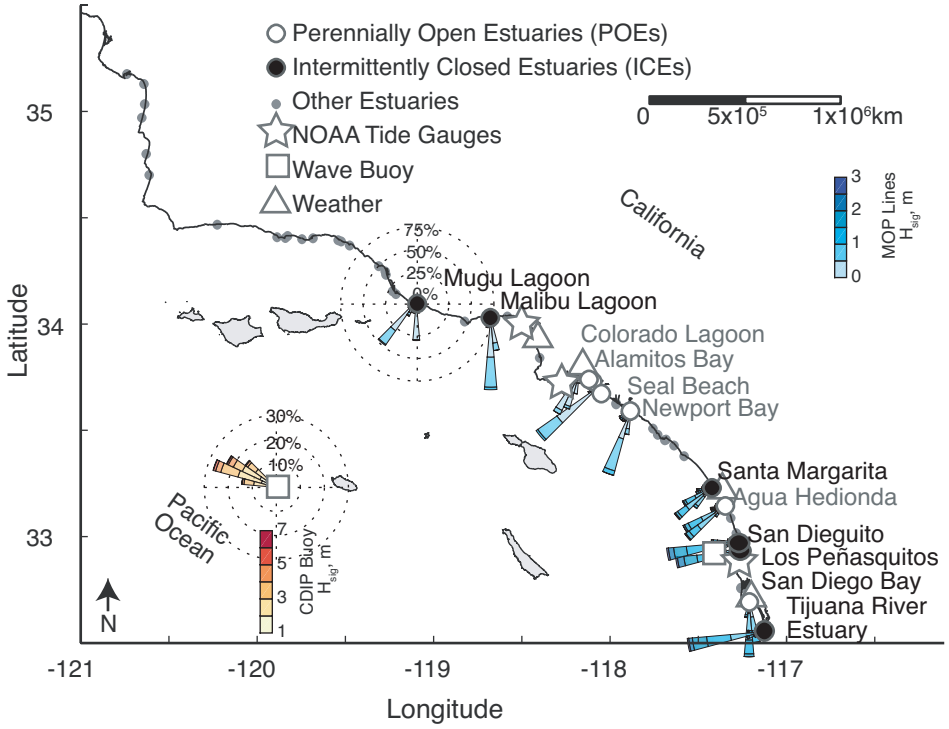

Figure 5.1: Observation locations. Southern California coastline with estuaries (circles), tide gauges (stars), weather stations (triangles), and wave buoys (squares). Estuaries included in this study are labeled and split into perennially open (large open circles) and intermittently closed (large filled circles). Wave roses are shown at each estuary entrance (blues) and at the offshore wave buoy (oranges). Estuary wave data were from MOP hindcast data (cdip.ucsd.edu, O'Reilly et al., 2016). Offshore data from CDIP San Nicholas Island observational buoy (cdip.ucsd.edu, Station ID 067). Colors indicate percent occurrence of waves at each station from Nov 01, 2015 to April 01, 2016 within each wave height and direction band.

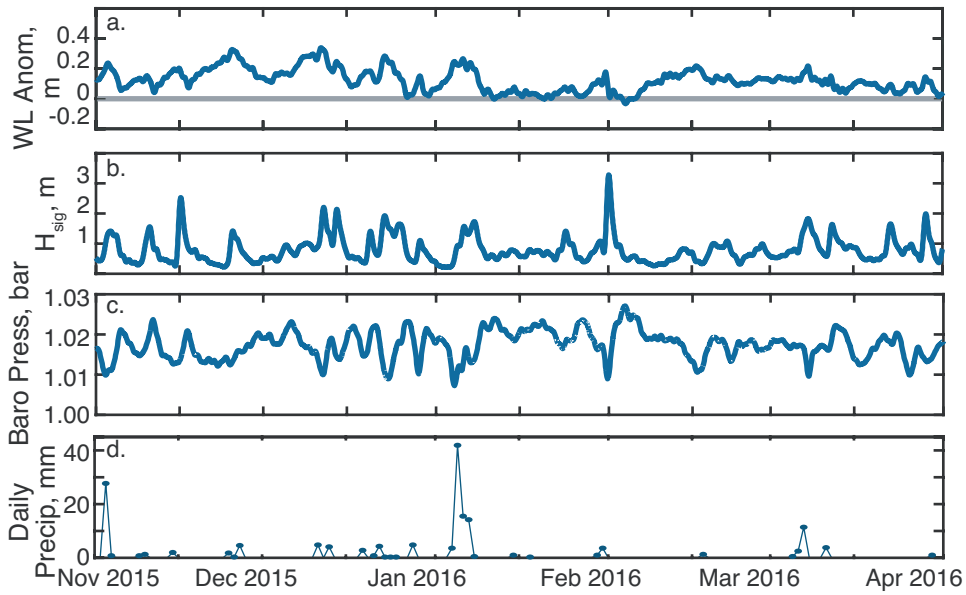

Figure 5.2: Regional conditions in southern California a.) 24-hour low-pass water level anomaly (observed minus predicted) at the La Jolla tide gauge (tidesandcurrents.noaa.gov Station ID: 9410230). b.) 24-hour low-pass filtered significant wave height from the MOP hindcast line closest to the La Jolla tide gauge (cdip.ucsd.edu Station ID: D0589) c.) 24-hour low-pass barometric pressure at the La Jolla tide gauges d.) Daily precipitation from San Diego Airport (ncdc.noaa.gov Station ID: USW00023188).

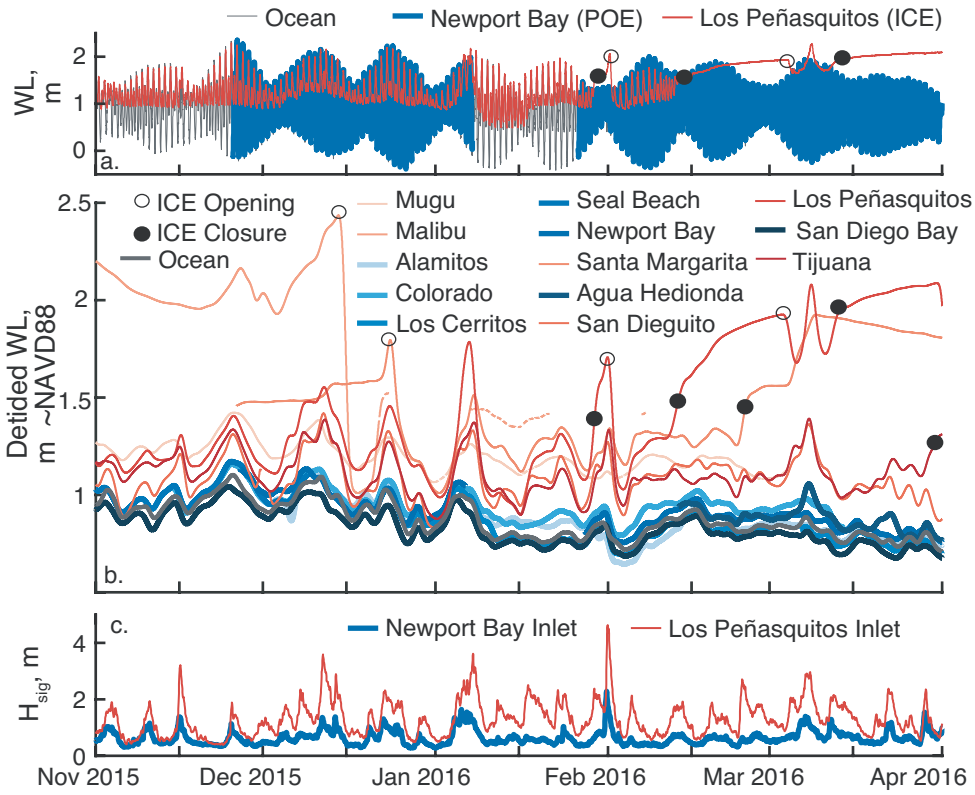

Figure 5.3: Water levels and ocean waves a.) Tidal water levels in Los Peñasquitos Lagoon (red thin), Newport Bay (blue thick), and offshore in the coastal ocean (grey thin). b.) Detided water level for all 13 estuaries during the observational period. Red, thin lines indicate intermittently closed estuaries (ICEs) while blue, thick lines indicate perennially open estuaries (POEs) and the thick gray line indicates ocean water level. Estuary lines are shaded from North (lightest) to South (darkest). Dots on a and b indicate mouth state changes to closed (filled) or open (open). c.) MOP hindcast of significant wave height at Los Peñasquitos Lagoon (red thin) and Newport Bay (blue thick) mouths.

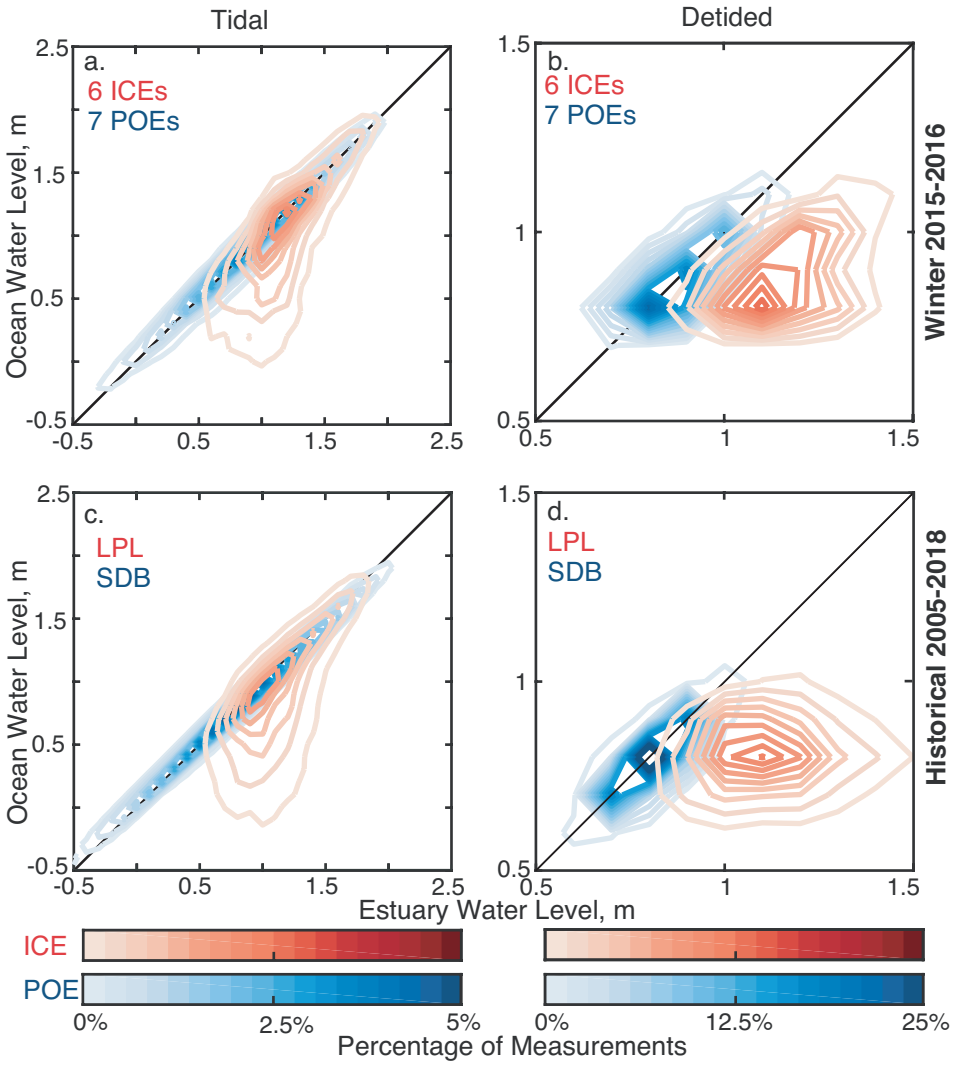

Figure 5.4: 2-Dimensional histograms of ocean water level vs estuary water level for open-mouth periods. (a) Histograms based on tidal water levels for 6 ICEs and for 7 POEs, using all available 2015-2016 winter data; (b) As in a, but for detided water level data; (c) Histograms based on tidal water levels for LPL and for SDB, using all available data from 2005 to 2018; (d) As in c, but for detided water level data. ICEs are indicated in red and POEs in blue where the colored contours (colorbars at the bottom) indicate percentage occurrence for each ocean and estuary water level value.

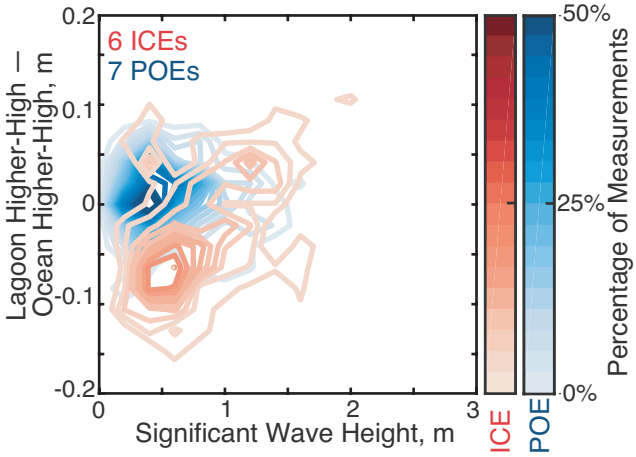

Figure 5.5: 2-Dimensional histogram of estuary higher-high water level minus ocean higher-high water level vs. significant wave heights at the closest MOP lines to the estuary mouths. ICE data are only for times when the mouth is open. A positive (negative) value on the y axis would indicate a setup (setdown) inside of the estuary relative to the ocean if the absolute elevations were exact. ICEs are indicated in red and POEs in blue where the colorbars and contours indicate the percentage occurrences at each wave height and water level for all available ICE and POE data during open periods in 2015-16

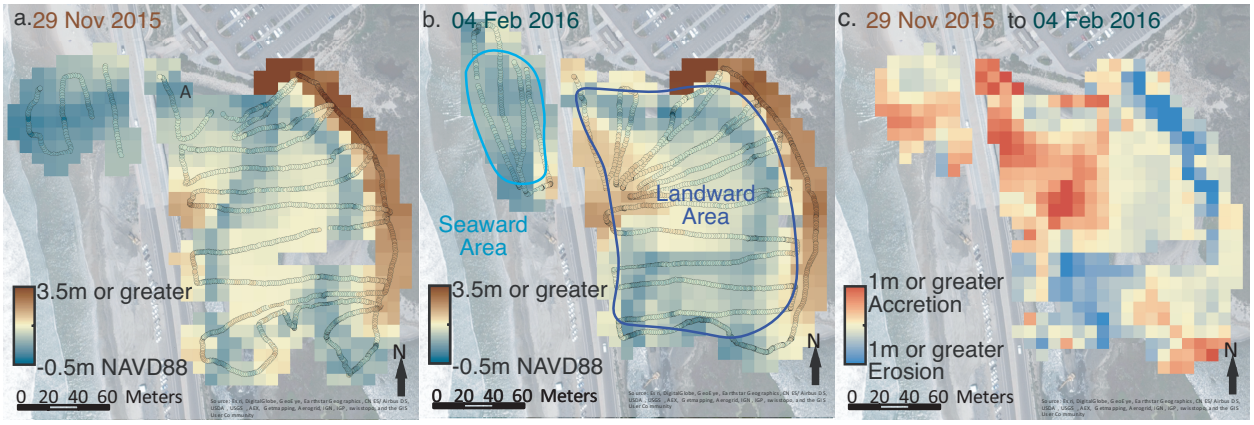

Figure 5.6: Los Peñasquitos Lagoon topo-bathymetry surveys on (a) 29 Nov 2015 and (b) 4 Feb 2016 – circles indicate measurement locations; data gridded into 8-meter cells using inverse difference weighted interpolation. Lines on b delineate the two averaging areas for estimating sill height: seaward, "beach area" (cyan) and landward, "estuary area" (dark blue) – see Figure 5.7. (c) Difference between surveys where red is deposition (accretion) and blue is erosion.

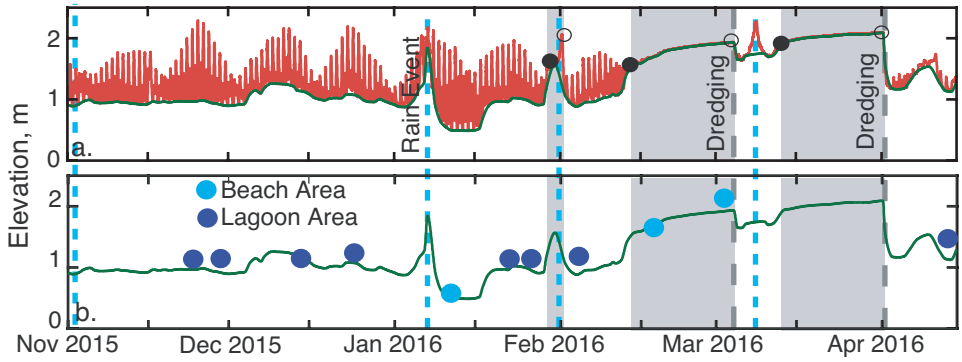

Figure 5.7: a.) Tidal water level of Los Peñasquitos Lagoon (red) and lower-low water level (dark green). Major precipitation events (light blue, dashed) and mouth dredging events (gray, dashed) are marked with vertical lines. Dots indicate mouth state changes to closed (filled) or open (open). Gray shading indicates closed periods. b.) Lower-low water level (as in a) and average elevation of beach (light blue) and estuary (dark blue) areas as demarcated in Figure 5.5.

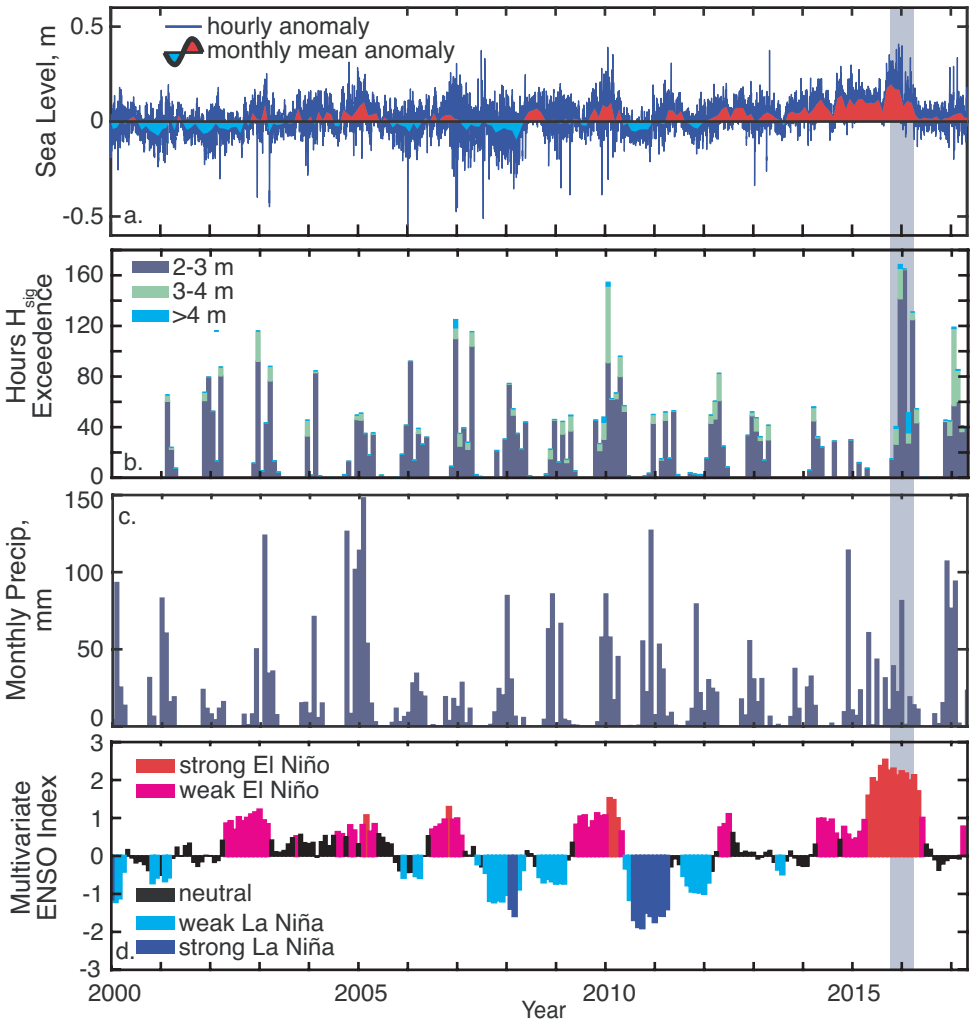

Figure 5.S1: Conditions in Southern California Jan 2000 to May 2017. Gray vertical bar indicates 2015-2016 El Niño. a.) Hourly and monthly mean sea level anomaly (deviation from predicted water level) at the La Jolla tide gauge (tidesandcurrents.nooa.gov). b.) Hours per month when the cumulative wave height exceeded 2 m (dark blue), 3 m (green), and 4 m (light blue) at Torrey Pines Outer Buoy (cdip.ucsd.edu) c.) Monthly precipitation totals from the San Diego Airport (ncdc.noaa.gov) d.). Monthly values of Multivariate ENSO Index where red indicates El Niño conditions and blue indicates La Nina conditions (www.esrl.noaa.gov).

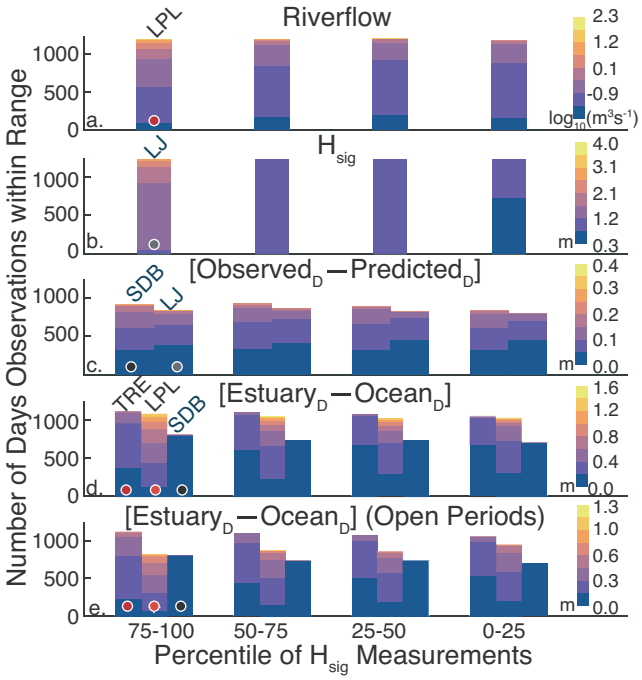

Figure 5.S2: Historical observations grouped by significant wave height measurement quartiles presented as histograms of occurrences (number of days over 14 years of data) within each quartile group. Yellows indicate higher values of the value of interest; purples indicate lower values. a.) Riverflow at Los Peñasquitos Lagoon (waterdata.usgs.gov; USGS Stream Gauge: 11023340) b.) 24-hour low-passed significant wave height (cdip.ucsd.edu; CDIP Buoy: 100) c.) Detided ocean water level anomalies, observed water level minus predicted water level for San Diego Bay and La Jolla tide gauges (tidesandcurrents.noaa.gov; Station ID: 9410170 and 9410230) d.) Detided estuary water level minus detided ocean water level for TRE, LPL and SDB. e.) same as d, but only data during open periods is included. For example, Panel d shows that the highest detided estuary deviations above ocean water levels are up to 1.6 m in magnitude and occur relatively more frequently for both ICEs (TRE and LPL) when wave heights are in their highest quartile.

5.8 Acknowledgments

We thank members and volunteers of the Giddings, Guza, and Pawlak labs at UCSD, Whitcraft Lab at CSULB (esp. M. Burdick-Whipp), and the scientists at the Tijuana River National Estuarine Research Reserve for help with data collection. This work was partially funded by California Sea Grant grant # NA14OAR4170075 with SCCWRP, University of Southern California Sea Grant grant #75193327 with Scripps Institution of Oceanography, California Department of Parks and Recreation Division of Boating and Waterways

Oceanography Program under contract #C1670005 with Scripps Institution of Oceanography, California Coastal Conservancy, NOAA National Estuarine Research Reserve System Science Collaborative, Los Peñasquitos Lagoon Foundation (esp. Mike Hastings), and a Blasker Environment Grant from the San Diego Foundation to Scripps Institution of Oceanography. Funding for Seal Beach, Mugu Lagoon, and Newport Bay data collection was provided by the DOI Southwest Climate Adaptation Science Center and U.S. Geological Survey, Western Ecological Research Center. This work was additionally supported by two traineeships through University of Southern California Sea Grant and the NOAA Ernest F. Hollings Undergraduate Scholarship. One anonymous reviewer, Dr. Sean Vitousek, and Dr. John Calloway provided valuable feedback which substantially improved this manuscript. Publicly available data are cited within the text, captions and references. Estuary data will be made available through the UCSD library. Any use of trade, product, or firm names in this publication is for descriptive purposes only and does not imply endorsement by the U.S. government.

Chapter 5, in full, is a the reproduction of a manuscript that is accepted to *Estuaries and Coasts*: Madeleine Harvey, Sarah N. Giddings, Eric D. Stein, Jeffrey A. Crooks, Christine Whitcraft, Timu Gallien, John L. Largier, Liesl Tiefenthaler, Hallee Meltzer, Geno Pawlak, Karen Thorne, Karina Johnston, Richard Ambrose, Stephen C. Schroeter, Henry M. Page, Hany Elwany. (2019). Effects of Elevated Sea Levels and Waves on Southern California Estuaries during the 2015-2016 El Niño. I was the primary investigator and author of this work.

Summary and Conclusions

This dissertation investigates the hydrodynamic variability of low-inflow, bar-built, and intermittently closed estuaries over various time scales including tidal, diurnal, spring-neap, seasonal, and interannual. Unprecedented, long-term field observations collected in Los Peñasquitos Lagoon (LPL) over several unique periods of Southern California climatology add valuable insight into how these estuaries respond to changing nearshore and upstream forcings. While LPL would historically have functioned more like an open, low-inflow estuary with periodic inverse circulation structures; development in and around the watershed has prevented it from going inverse (except during periods of extreme drought) and has encouraged sill growth and closures. When the sill near the mouth is low, the estuary functions, in many ways, like a larger, canonical estuary with evidence of strain-induced period stratification and canonical exchange flow that is larger during neap tides. However, a combination of flood dominance and wave-induced sediment transport contribute to inlet accretion and sill growth. As the sill grows, the estuarine exchange strengthens, particularity during spring tides, thereby departing from canonical estuarine theory.

During particularly low river discharge, and/or large wave conditions, wave-driven sediment accumulation can exceed tidal/fluvial erosion enough to raise the sill to form a barrier berm at the estuary inlet that completely separates the estuary from the ocean thereby effectively forming a salt-stratified lake. Generally, following closures, estuarine water levels increase due to a combination of river flows, overtopping, precipitation, and urban runoff; stratification develops; and dissolved oxygen near the bottom declines rapidly. However, between different closures the circulation patterns can vary dramatically, but they are relatively consistent amongst

seasons where the amount of incoming freshwater dictates the strength and depth of stratification. The predominant period of circulation during closures is diurnal. This diurnal circulation can be attributed to differential heating and cooling driving thermal exchange circulation cells that is weakened by diurnal winds which drive circulation cells in the opposite sense. Most closures that occurred during the observation period were mechanically breached to restore tidal flushing to the estuary. Throughout Southern California, many naturally occurring intermittently closed estuaries are managed to maintain an open state through dredging, building hard structures to prevent sedimentation and enhance scour, or some combination of methods that functionally convert intermittently closed estuaries to perennially open estuaries.

During the 2015-2016 winter, observations from 12 additional Southern California low-inflow estuaries (6 intermittently closed estuaries and 6 perennially open estuaries) were conducted and used to compare estuarine response to similar offshore forcing conditions. Water levels from such a wide range of systems experiencing similar forcing conditions are rarely measured simultaneously. Results suggest that intermittently closed estuaries worldwide may be more susceptible to altered water levels as well as morphological changes resulting from sea-level rise and higher wave heights. Continuous, long-term monitoring of low-inflow, bar-built, and intermittently closed estuaries is necessary to further our understanding of how these, systems that are common worldwide and provide extensive ecosystem functions and services, will respond and adapt to a changing climate.

References

Adams, Janine. (2014). A review of methods and frameworks used to determine the environmental water requirements of estuaries. Hydrological Sciences Journal 59: 451–465. doi:10.1080/02626667.2013.816426.

Bagnold, R. (1966). An approach to the sediment transport problem from general physics.

Barnard, Patrick L, Daniel Hoover, David M. Hubbard, Alex Snyder, Bonnie C. Ludka, Jonathan Allan, George M. Kaminsky, Peter Ruggiero, Timu W. Gallien, Laura Gabel, Diana McCandless, Heather M. Weiner, Nicholas Cohn, Dylan L. Anderson & Katherine A. Serafin. 2017. Extreme ocean forcing and coastal response due to the 2015-2016 El Niño. Nature Communications 8:14365. doi:10.1038/ncomms14365.

Becker, A., Laurenson, L., & Bishop, K. (2009). Artificial mouth opening fosters anoxic conditions that kill small estuarine fish. Estuarine, Coastal and Shelf Science, 82(4), 566–572. https://doi.org/10.1016/j.ecss.2009.02.016

Behrens, D. K., Bombardelli, F. A., & Largier, J. L. (2016). Landward Propagation of Saline Waters Following Closure of a Bar-Built Estuary: Russian River (California, USA). Estuaries and Coasts, 39(3), 621–638. https://doi.org/10.1007/s12237-015-0030-8

Behrens, D. K., Bombardelli, F. A., Largier, J. L., & Twohy, E. (2009). Characterization of time and spatial scales of a migrating rivermouth. Geophysical Research Letters, 36(9). https://doi.org/10.1029/2008gl037025

Behrens, D. K., Bombardelli, F. A., Largier, J. L., & Twohy, E. (2013). Episodic closure of the tidal inlet at the mouth of the Russian River — A small bar-built estuary in California. Geomorphology, 189, 66–80. https://doi.org/10.1016/j.geomorph.2013.01.017

Bertin, X., & Olabarrieta, M. (2016). Relevance of infragravity waves in a wave-dominated inlet. *Journal of Geophysical Research: Oceans*, 121(8), 5418–5435. https://doi.org/10.1002/2015jc011444

Bertin, X., de Bakker, A., van Dongeren, A., Coco, G., André, G., Ardhuin, F., et al. (2018). Infragravity waves: From driving mechanisms to impacts. Earth-Science Reviews, 177(Mar. Geol. 118 1994), 774–799. https://doi.org/10.1016/j.earscirev.2018.01.002

Bertin, X., Fortunato, A. B., & Oliveira, A. (2009). A modeling-based analysis of processes driving wave-dominated inlets. Continental Shelf Research, 29(5–6), 819–834. https://doi.org/10.1016/j.csr.2008.12.019

Bertin, X., Mendes, D., Martins, K., Fortunato, A. B., & Lavaud, L. (2019). The Closure of a Shallow Tidal Inlet Promoted by Infragravity Waves. Geophysical Research Letters, 46(12), 6804–6810. https://doi.org/10.1029/2019gl083527

Blanton, J., Ferreira, M., & Andrade, F. (2000). Effect of a broad shallow sill on tidal circulation and salt transport in the entrance to a coastal plain estuary (Mira—Vila Nova de Milfontes, Portugal). Estuaries, 23(3), 293–304. https://doi.org/10.2307/1353322

Bond, M. H., Hayes, S. A., Hanson, C. V., & MacFarlane, B. R. (2008). Marine survival of steelhead (Oncorhynchus mykiss) enhanced by a seasonally closed estuary. Canadian Journal of Fisheries and Aquatic Sciences, 65(10), 2242–2252. https://doi.org/10.1139/f08-131

Bond, N. A., Cronin, M. F., Freeland, H., & Mantua, N. (2015). Causes and impacts of the 2014 warm anomaly in the NE Pacific. Geophysical Research Letters, 42, 3414–3420. https://doi.org/10.1002/2015GL063306

Bromirski, Peter D, Reinhard E Flick, and Daniel R Cayan. 2003. Storminess variability along the California Coast: 1858–2000. Journal of Climate 16: 982–993.

Cai, W., S. Borlace, M. Lengaigne, P.V. Rensch, M. Collins, G. Vecchi, A. Timmermann, A. Santoso, M.J. McPhaden, L. Wu, M.H. England, G. Wang, E. Guilyardi, and F. Jin. 2014. Increasing frequency of extreme El Niño events due to greenhouse warming. Nature climate change. 4(2). doi: 10.1038/nclimate2100.

California Natural Resources Agency. 2010. State of the state's wetlands: 10 years of challenges and progress.

Cayan, Daniel R, Peter D Bromirski, Katharine Hayhoe, Mary Tyree, Michael D Dettinger, and Reinhard E Flick. 2008. Climate change projections of sea level extremes along the California coast. Climatic Change 87: 57–73. doi:10.1007/s10584-007-9376-7.

cdip.usd.edu. 2017. CDIP (The Coastal Data Information Program) Historic Data. https://cdip.ucsd.edu / Buoy ID: 100. Accessed October 11 2017.

Chant, R. J., Sommerfield, C. K., & Talke, S. A. (2018). Impact of Channel Deepening on Tidal and Gravitational Circulation in a Highly Engineered Estuarine Basin. Estuaries and Coasts, 41(6), 1587–1600. https://doi.org/10.1007/s12237-018-0379-6

Characterizing submarine ground-water discharge using fiber-optic distributed temperature sensing and marine electrical resistivity,. (n.d.).

Chelton, Dudley B, and Ross E Davis. 1982. Monthly mean sea level variability along the West Coast of North America. Journal of Physical Oceanography 12: 757–784.

Clark, N. E., Eber, L., Laurs, R. M., Renner, J. A., & Saur, J. F. T. (1974). Heat exchange between ocean and atmosphere in the eastern North Pacific for 1961–71. NOAA Tech. Rep. NMFS SSRF-682.

Clark, R., & O'Connor, K. (2019). A systematic survey of bar-built estuaries along the California coast. Estuarine, Coastal and Shelf Science, 226, 106285. https://doi.org/10.1016/j.ecss.2019.106285

Cole, K. L., & Wahl, E. (2000). A Late Holocene Paleoecological Record from Torrey Pines State Reserve, California. Quaternary Research, 53(3), 341–351. https://doi.org/10.1006/qres.1999.2121

Cole, Kenneth L., and Eugene Wahl. 2000. A late Holocene paleoecological record from Torrey Pines State Reserve, California. Quaternary Research 53: 341–351. doi:10.1006/qres.1999.2121.

Committee on Sea Level Rise in California, Oregon and Washington, Board on Earth Sciences and Resources, Ocean Studies Board, Division on Earth and Life Studies, National Research Council. 2017. Sea-Level Rise for the Coasts of California, Oregon, and Washington: Past, Present, and Future. National Academies Press: 1–217. doi:10.17226/13389.

Connolly, T. P., & Kirincich, A. R. (2019). High-Resolution Observations of Subsurface Fronts and Alongshore Bottom Temperature Variability Over the Inner Shelf. Journal of Geophysical Research: Oceans, 124(1), 593–614. https://doi.org/10.1029/2018jc014454

Cooper, J. A. . (2001). Geomorphological variability among microtidal estuaries from the wave-dominated South African coast. Geomorphology, 40(1–2), 99–122. https://doi.org/10.1016/s0169-555x(01)00039-3

Cousins, M., Stacey, M. T., & Drake, J. L. (2010). Effects of seasonal stratification on turbulent mixing in a hypereutrophic coastal lagoon. Limnology and Oceanography, 55(1), 172–186. https://doi.org/10.4319/lo.2010.55.1.0172

Davidson, M. A., Morris, B. D., & Turner, I. L. (2009). A simple numerical model for inlet sedimentation at intermittently open–closed coastal lagoons. Continental Shelf Research, 29(16), 1975–1982. https://doi.org/10.1016/j.csr.2008.10.005

Dawson, M. N., Staton, J. L., & Jacobs, D. K. (2001). Phylogeography Of The Tidewater Goby, Eucyclogobius Newberryi (Teleostei, Gobiidae), In Coastal California. Evolution, 55(6), 1167–1179. https://doi.org/10.1111/j.0014-3820.2001.tb00636.x

Dodet, G., Bertin, X., Bruneau, N., Fortunato, A. B., Nahon, A., & Roland, A. (2013). Wave-current interactions in a wave-dominated tidal inlet. Journal of Geophysical Research: Oceans, 118(3), 1587–1605. https://doi.org/10.1002/jgrc.20146

Doughty, Cheryl L., Kyle C. Cavanaugh, Richard F. Ambrose and Eric D. Stein. 2018. Evaluating regional resiliency of coastal wetlands to sea level rise through hypsometry-based modeling. Global Change Biology 25:78-92. doi:10.1111/gcb.14429.

Dronkers, J. (1986). Tidal asymmetry and estuarine morphology. Netherlands Journal of Sea Research, 20(2/3), 117–131. Retrieved from www.sciencedirect.com

Dussaillant, A., Galdames, P., & Sun, C.-L. (2009). Water level fluctuations in a coastal lagoon: El Yali Ramsar wetland, Chile. Desalination, 246(1–3), 202–214. https://doi.org/10.1016/j.desal.2008.03.053

Elwany, H. M. (2011). Characteristics, Restoration, and Enhancement of Southern California Lagoons. Journal of Coastal Research, 59, 246–255. https://doi.org/10.2112/si59-026.1

Elwany, M. Hany S., Reinhard E. Flick, and Saima Aijaz. (1998). Opening and closure of a marginal Southern California lagoon inlet. Estuaries 21: 246–254.

Enfield, David B., and J S Allen. (1980). On the structure and dynamics of monthly mean sea level anomalies along the Pacific Coast of North and South America. Journal of Physical Ocean 10: 557–578.

Fairall, C., Bradley, E., Hare, J., Grachev, A., & Edson, J. (2003). Bulk Parameterization of Air–Sea Fluxes: Updates and Verification for the COARE Algorithm. Journal of Climate, 16(4), 571–591. https://doi.org/10.1175/1520-0442(2003)016<0571:bpoasf>2.0.co;2

Farrow, D., & Patterson, J. (1993). On the response of a reservoir sidearm to diurnal heating and cooling. Journal of Fluid Mechanics, 246(1), 143–161. https://doi.org/10.1017/s0022112093000072

Flick, Reinhard E. (2016). California tides, sea level, and waves - Winter 2015-2016. Shore and Beach 84: 25–30.

Frazão, O., Pereira, D., Santos, J., Dias, I., Dias, J., Vaz, N., et al. (2010). Industrialization of advanced optical technologies for environmental monitoring. Clean Technologies and Environmental Policy, 12(1), 65–73. https://doi.org/10.1007/s10098-009-0222-7

Friedrichs, C. T., & Madsen, O. S. (1992). Nonlinear diffusion of the tidal signal in frictionally dominated embayments. Journal of Geophysical Research: Oceans, 97(C4), 5637–5650. https://doi.org/10.1029/92JC00354

Friedrichs, Carl T. (2010). Barotropic tides in channelized estuaries. Contemporary issues in estuarine physics. Cambridge: Cambridge University Press. doi:10.1017/CBO9780511676567.

Gale, E., Pattiaratchi, C., & Ranasinghe, R. (2006). Vertical mixing processes in Intermittently Closed and Open Lakes and Lagoons, and the dissolved oxygen response. Estuarine, Coastal and Shelf Science, 69(1–2), 205–216. https://doi.org/10.1016/j.ecss.2006.04.013

Gale, E., Pattiaratchi, C., & Ranasinghe, R. (2007). Processes driving circulation, exchange and flushing within intermittently closing and opening lakes and lagoons. Marine and Freshwater Research, 58(8), 709–719. https://doi.org/10.1071/MF06121

Geyer, R. W., & MacCready, P. (2013). The Estuarine Circulation. Fluid Mechanics, 46(1), 175–197. https://doi.org/10.1146/annurev-fluid-010313-141302

Geyer, R. W., & Smith, D. J. (1987). Shear Instability in a Highly Stratified Estuary. Journal of Physical Oceanography, 17, 1668 1679. https://doi.org/10.1175/1520-0485(1987)017<1668:siiahs>2.0.co;2

Geyer, W. (2010). Estuarine Salnity Structure and Circulation, 12–26. https://doi.org/10.1017/cbo9780511676567.003

Geyer, W. R., & Ralston, D. K. (2011). Treatise on Estuarine and Coastal Science, 2, 37–51. https://doi.org/10.1016/b978-0-12-374711-2.00206-0

Goodman, A. C., Thorne, K. M., Buffington, K. J., Freeman, C. M., & Janousek, C. N. (2018). El Niño Increases High-Tide Flooding in Tidal Wetlands Along the U.S. Pacific Coast. Journal of Geophysical Research: Biogeosciences, 123(10), 3162–3177. https://doi.org/10.1029/2018JG004677

Goodman, Arianna, Karen Thorne, Kevin Buffington, Chase Freeman, and Christopher Janousek. (2018). El Niño Increases High-Tide Flooding in Tidal Wetlands Along the U.S. Pacific Coast. Journal of Geophysical Research: Biogeosciences 123. wiley: 3162–3177. doi:10.1029/2018JG004677.

Griggs, Gary, Dan Cayan, Claudia Tebaldi, Helen A. Fricker, Joseph Arvai, Robert DeConto, Robert E. Kopp. (2017). Rising seas in California: An update on sea-level rise science. California ocean science trust.

Hansen, J.V. (1966). New Dimensions in Estuary Classification. https://doi.org/10.2307/2833361

Hartmann, D. L. (2015). Pacific sea surface temperature and the winter of 2014. Geophysical Research Letters, 42(6), 1894–1902. https://doi.org/10.1002/2015GL063083

Harvey, M.E., S.N. Giddings, E. Stein, J. Crooks, C. Whitcraft, T. Gallien, J. Largier, L. Tieffenthaler, H. Meltzer, G. Pawlak, K. Thorne, K Johnston, R. Ambrose, S. Schroeter, H. M. Page, H. Elwany (2019), Effects of elevated sea levels and waves on Southern California estuaries during the 2015-2016 El Niño. Estuaries and Coasts.

Hastings, M., & Elwany, H. (2012). Managing the Inlet at Los Penasquitos Lagoon. Shore and Beach, 80(1), 2012.

Hausner, M. B., Suárez, F., Glander, K. E., van de Giesen, N., Selker, J. S., & Tyler, S. W. (2011). Calibrating Single-Ended Fiber-Optic Raman Spectra Distributed Temperature Sensing Data. Sensors, 11(11), 10859–10879. https://doi.org/10.3390/s111110859

Hayes, M. O. (1979). Barrier island morphology as a function of tidal wave and wave regime . In Barier Islands from Mexico to the Gulf of St. Laurance (pp. 1–28). New York: Academic Press.

Hearn, C. J., & Largier, J. (1997). The Summer Buoyancy Dynamics of a Shallow Mediterranean Estuary and Some Effects of Changing Bathymetry; Tomales Bay, California. Estuarine, Coastal and Shelf Sciences, 45(4), 497–506. https://doi.org/10.1006/ecss.1996.0197

Henderson, R., Day-Lewis, F., & Harvey, C. (2009). Investigation of aquifer-estuary interaction using wavelet analysis of fiber-optic temperature data. Geophysical Research Letters, 36(6). https://doi.org/10.1029/2008gl036926

Henderson, Rory & Day-Lewis, Frederick & Harvey, Charles. (2008). Characterizing Submarine Ground-Water Discharge Using Fiber-Optic Distributed Temperature Sensing and Marine Electrical Resistivity. 10.4133/1.2963319.

Holleman, Rusty C., and Mark T. Stacey. (2014). Coupling of sea level rise, tidal amplification, and inundation. Journal of Physical Oceanography 44: 1439–1455. doi:10.1175/JPO-D-13-0214.1.

Holmquist, James R, Lisamarie Windham-Myers Norman Bliss, Stephen Crooks, James T. Morris, J. Patrick Megonigal, Tiffany Troxler, Donald Weller, John Callaway, Judith Drexler, Matthew C. Ferner, Meagan E. Gonneea, Kevin D. Kroeger, Lisa Schile-Beers, Isa Woo, Kevin Buffington, Joshua Breithaupt, Brandon M. Boyd, Lauren N. Brown, Nicole Dix, Lyndie Hice, Benjamin P . Horton, Glen M. MacDonald, Ryan P. Moyer, William Reay, Timothy Shaw, Erik Smith, Joseph M. Smoak, Christopher Sommerfield, Karen Thorne, David Velinsk, Elizabeth Watson, Kristin Wilson Grimes, and Mark Woodrey. (2018). Accuracy and precision of tidal wetland soil Carbon mapping in the conterminous United States. Scientific Reports 8:6478. doi:10.1038/s41598-018-26948-7.

Hubbard, David M. (1996.) Tidal cycle distortion in Carpinteria Salt Marsh, California. Bulletin of the Southern California Academy of Sciences 95: 88–98.

Hughes, B. B., Levey, M. D., Brown, J. A., Fountain, M. C., Carlisle, A. B., Green, C. M., et al. (2014). Nursery functions of U.S. West Coast estuaries: The state of knowledge for juvinels of focal invertabrete and fish species, 168.

Imberger, J., & Patterson, J. C. (1989). Physical Limnology. Advances in Applied Mechanics, 27, 303–475. https://doi.org/10.1016/s0065-2156(08)70199-6

Jacobs, David, Eric D. Stein, and Travis Longcore. (2010). Classification of California Estuaries Based on Natural Closure Patterns: Templates for Restoration and Management. Southern California Coastal Water Research Project. Technical Report 619.

Janousek, C., K. Buffington, K. Thorne, G. Guntenspergen, J. Takekawa, B. Dugger. (2016). Potential effects of sea-level rise on plant productivity: species-specific responses in northeast. Pacific tidal marshes Marine Ecology Progress Series 548, 111-125. doi:10.3354/meps11683.

Josey, S. A., Oakley, D., & Pascal, R. W. (1997). On estimating the atmospheric longwave flux at the ocean surface from ship meteorological reports. Journal of Geophysical Research: Oceans, 102(C13), 27961–27972. https://doi.org/10.1029/97jc02420

Kobs, S., Holland, D. M., Zagorodnov, V., Stern, A., & Tyler, S. W. (2014). Novel monitoring of Antarctic ice shelf basal melting using a fiber-optic distributed temperature sensing mooring. Geophysical Research Letters, 41(19), 6779–6786. https://doi.org/10.1002/2014gl061155

Largier, J. L. (2010). Low inflow estuaries: hypersaline, inverse, and thermal scenarios. Contemporary issues in estuarine physics. Cambridge: Cambridge University Press. doi:10.1017/CBO9780511676567.

Largier, J. L., J.H. Slinger, and S. Taljaard. (1992). The Stratified Hydrodynamics of the Palmiet - A Prototypical Bar-Built Estuary. In Dynamics and Exchanges in Estuaries and the Coastal Zone, D. Prandle (Ed.). doi:10.1029/CE040p0135.

Largier, J.L., & Taljaard, S. (1991). The dynamics of tidal intrusion, retention, and removal of seawater in a bar-built estuary. Estuarine, Coastal and Shelf Science, 33(4), 325–338. https://doi.org/10.1016/0272-7714(91)90061-f

Largier, JL, Slinger, J., & Taljaard, S. (2013). Dynamics and Exchanges in Estuaries and the Coastal Zone. American Geophysical Union, 135–153. https://doi.org/10.1029/ce040p0135

Largier, John L, Hearn, C. J., & Chadwick, B. D. (1996). Density Structures in "Low Inflow Estuaries." wiley (pp. 227–241). wiley. https://doi.org/10.1029/ce053p0227

Largier, John L, Hollibaugh, J., & Smith, S. (1997). Seasonally Hypersaline Estuaries in Mediterranean-climate Regions. Estuarine, Coastal and Shelf Science, 45, 789 797.

Largier, John, O'Connor, K., & Clark, R. (2019). Considerations for Management of the Mouth State of Caliofornia's Bar-built Estuaries Prepared for: Pacific States Marine Fisheries Commission and NOAA (No. NA14NMF437012).

Lee, Sang-Ki, Hosmay Lopez, Eui-Seok Chung, Pedro DiNezio, Sang-Wook Yeh, and Andrew T. Wittenberg. (2018). On the fragile relationship between El Niño and California rainfall. Geophysical Research Letters 45:907-915. doi:10.1002/2017GL076197.

Lucas, A., & Pinkel, R. (2018). Continuous space-time measurements of shoaling internal waves in the inner shelf bottom boundary layer.

Los Peñasquitos Lagoon Foundation, ESA, Norby Biological Consulting, KTU+A. (2016). Los Peñasquitos Lagoon Enhancement Plan.

Ludka, B., Gallien, T., & Research …, C. S. (2016). Mid-El Niño erosion at nourished and unnourished Southern California beaches. https://doi.org/10.1002/2016GL068612

Ludka, Bonnie C, Timu Gallien, Sean C. Crosby, and Robert T. Guza. (2016). Mid-El Niño erosion at nourished and unnourished Southern California beaches. Geophysical Research Letters: 1–7. doi:10.1002/(ISSN)1944-8007.

Ludka, Bonnie C., Robert T. Guza, and William C. O'Reilly. (2018). Nourishment evolution and impacts at four southern California beaches: A sand volume analysis. Coastal Engineering 136:96–105. doi:10.1016/j.coastaleng.2018.02.003.

MacCready, P., & Geyer, R. W. (2010). Advances in Estuarine Physics. Annual Review of Marine Science, 2(1), 35–58. https://doi.org/10.1146/annurev-marine-120308-081015

Malhadas, Madalena, Paulo Leitão, Adélio Silva, and Ramiro Neves. (2009). Effect of coastal waves on sea level in Óbidos Lagoon, Portugal. Continental Shelf Research 29: 1240–1250. doi:10.1016/j.csr.2009.02.007.

Masselink, G., & Pattiaratchi, C. B. (2001). Characteristics of the Sea Breeze System in Perth, Western Australia, and Its Effect on the Nearshore Wave Climate. Journal of Coastal Research, 17, 173–187.

McSweeney, S., Keenedy, D., & Rutherfurd, I. (2017). A geomorphic classification of intermittently open/closed estuaries (IOCE) derived from estuaries in Victoria, Australia. Progress in Physical Geography, 41(4), 421–449. https://doi.org/10.1177/0309133317709745

Moffett, K. B., Tyler, S. W., Torgersen, T., Menon, M., Selker, J. S., & Gorelick, S. M. (2008). Processes Controlling the Thermal Regime of Saltmarsh Channel Beds. Environmental Science & Technology, 42(3), 671–676. https://doi.org/10.1021/es071309m

Molina, L., Pawlak, G., Wells, J., Monismith, S., & Merrifield, M. (2014). Diurnal cross-shore thermal exchange on a tropical forereef. Journal of Geophysical Research: Oceans, 119(9), 6101–6120. https://doi.org/10.1002/2013jc009621

Monismith, S. G., Imberger, J., & Morison, M. L. (1990). Convective motions in the sidearm of a small reservoir. Limnology and Oceanography, 35(8), 1676–1702. https://doi.org/10.4319/lo.1990.35.8.1676

Moreno, I., Ávila, A., & Losada, M. (2010). Morphodynamics of intermittent coastal lagoons in Southern Spain: Zahara de los Atunes. Geomorphology, 121(3–4), 305–316. https://doi.org/10.1016/j.geomorph.2010.04.028

Morris, B.D., and I.L. Turner, (2010). Morphodynamics of intermittently open–closed coastal lagoon entrances: New insights and a conceptual model, Marine Geology, 271(1–2), 55-66, doi: 10.1016/j.margeo.2010.01.009.

ncdc.noaa.gov. (2018). National Climatic Data Center. https://www.ncdc.noaa.gov/data-access/ Station ID: USW00023188. Accessed February 2019.

Nepf, H., & Geyer, W. (1996). Intratidal variations in stratification and mixing in the Hudson estuary. Journal of Geophysical Research: Oceans, 101(C5), 12079–12086. https://doi.org/10.1029/96jc00630

Nidzieko, N. J. (2010). Tidal asymmetry in estuaries with mixed semidiurnal/diurnal tides. Journal of Geophysical Research: Oceans (1978–2012), 115(C8). https://doi.org/10.1029/2009JC005864

Nidzieko, N. J., & Monismith, S. G. (2013). Contrasting Seasonal and Fortnightly Variations in the Circulation of a Seasonally Inverse Estuary, Elkhorn Slough, California. Estuaries and Coasts, 36, 1–17. https://doi.org/10.1007/s12237-012-954-1

Nidzieko, N., & Ralston, D. (2012). Tidal asymmetry and velocity skew over tidal flats and shallow channels within a macrotidal river delta. Journal of Geophysical Research: Oceans (1978–2012), 117(C3), n/a-n/a. https://doi.org/10.1029/2011jc007384

O'Reilly, William C., and Robert T. Guza. (1993). A comparison of two spectral wave models in the Southern California Bight. Coastal Engineering 19: 263–282.

O'Reilly, William C., Corey B Olfe, Julianna Thomas, R J Seymour, and Robert T Guza. (2016). The California coastal wave monitoring and prediction system. Coastal Engineering 116: 118–132. doi:10.1016/j.coastaleng.2016.06.005.

Okely, P., & Imberger, J. (2007). Horizontal transport induced by upwelling in a canyon-shaped reservoir. Hydrobiologia, 586(1), 343–355. https://doi.org/10.1007/s10750-007-0706-6

Olabarrieta, M., Warner, J. C., & Kumar, N. (2011). Wave-current interaction in Willapa Bay. Journal of Geophysical Research: Oceans (1978–2012), 116(C12). https://doi.org/10.1029/2011JC007387

Orescanin, M. M., & Scooler, J. (2018). Observations of Episodic Breaching and Closure at an Ephemeral River. Continental Shelf Research, 166(Mar. Geol. 271 2010), 77–82. https://doi.org/10.1016/j.csr.2018.07.003

Orescanin, M., Raubenheimer, B., & Elgar, S. (2014). Observations of wave effects on inlet circulation. Continental Shelf Research, 82, 37–42. https://doi.org/10.1016/j.csr.2014.04.010

Orescanin, M.A. and J. Scooler. (2018). Observations of episodic breaching and closure at an ephemeral river, Continental Shelf Research, 166, 77-82, doi:10.1016/j.csr.2018.07.003.

Phlips, E J, S Badylak, and T Grosskopf. 2002. Factors Affecting the Abundance of Phytoplankton in a Restricted Subtropical Lagoon, the Indian River Lagoon, Florida, USA. Estuarine, Coastal and Shelf Science 55: 385–402. doi:10.1006/ecss.2001.0912.

Pratt, Jamie. (2014). California Inlets: A Coastal Management "No Man's Land." Prepared for Surfrider Foundation.

Ralston, D. K., & Geyer, R. W. (2019). Response to Channel Deepening of the Salinity Intrusion, Estuarine Circulation, and Stratification in an Urbanized Estuary. Journal of Geophysical Research: Oceans. https://doi.org/10.1029/2019JC015006

Ralston, D. K., Geyer, R. W., & Lerczak, J. A. (2008). Subtidal Salinity and Velocity in the Hudson River Estuary: Observations and Modeling. Journal of Physical Oceanography, 38(4), 753–770. https://doi.org/10.1175/2007jpo3808.1

Ranasinghe, R., & Pattiaratchi, C. (1999a). Circulation and mixing characteristics of a seasonally open tidal inlet: a field study. Marine and Freshwater Research, 50(4), 281–290. https://doi.org/10.1071/mf98037

Ranasinghe, R., & Pattiaratchi, C. (1999b). The seasonal closure of tidal inlets: Wilson Inlet—a case study. Coastal Engineering, 37(1), 37–56. https://doi.org/10.1016/s0378-3839(99)00007-1

Ranasinghe, R., & Pattiaratchi, C. (2003). The Seasonal Closure of Tidal Inlets: Causes and Effects. Coastal Engineering Journal, 45(4), 601–627. https://doi.org/10.1142/S0578563403000919

Ranasinghe, R., Pattiaratchi, C., & Masselink, G. (1999). A morphodynamic model to simulate the seasonal closure of tidal inlets. Coastal Engineering, 37(1), 1–36. https://doi.org/10.1016/s0378-3839(99)00008-3

Raposa, Kenneth. 2002. Early Responses of Fishes and Crustaceans to Restoration of a Tidally Restricted New England Salt Marsh. Restoration Ecology 10: 665–676. doi:10.1046/j.1526-100X.2002.01047.x.

Raubenheimer, B., Elgar, S., & Guza, R. (1998). Estimating Wave Heights from Pressure Measured in Sand Bed. Journal of Waterway, Port, Coastal, and Ocean Engineering, 124(3), 151–154. https://doi.org/10.1061/(asce)0733-950x(1998)124:3(151)

Reid, E. C., Carlo, T., Cohen, A. L., Wong, G. T., Lentz, S. J., Safaie, A., et al. (2019). Internal waves influence the thermal and nutrient environment on a shallow coral reef. Limnology and Oceanography, 64(5), 1949–1965. https://doi.org/10.1002/lno.11162

Rich, A., & Keller, E. A. (2013). A hydrologic and geomorphic model of estuary breaching and closure. Geomorphology, 191, 64–74. https://doi.org/10.1016/j.geomorph.2013.03.003

Rich, Andrew, and Edward A. Keller. 2013. A hydrologic and geomorphic model of estuary breaching and closure. Geomorphology 191: 64–74. doi:10.1016/j.geomorph.2013.03.003.

Rinehimer, J., & Thomson, J. T. (2014). Observations and modeling of heat fluxes on tidal flats. Journal of Geophysical Research: Oceans, 119(1), 133–146. https://doi.org/10.1002/2013jc009225

Rinehimer, P. J., Thomson, J., & Chickadel, C. C. (2013). Thermal observations of drainage from a mud flat. Continental Shelf Research, 60, S125–S135. https://doi.org/10.1016/j.csr.2012.11.001

Roy, P. S., R.J. Williams, A.R. Jones, I. Yassini, P.J. Gibbs, B. Coates, R.J. West, P.R. Scanes, J.P. Hudson, and S. Nichol. 2001. Structure and function of south-east Australian estuaries. Estuarine, Coastal and Shelf Science 53, 351–384. doi:10.1006/ECSS.2001.0796.

Roy, P., Williams, R., & Jones, A. (2001). Structure and function of south-east Australian estuaries. Estuarine, Coastal and Shelf Science, 53(3). https://doi.org/10.1006/escc.2001.0796

Saad, Adriana M, Antonio C Baumord, and Erica P Caramaschi. 2002. Effects of Artificial Canal Openings on Fish Community Structure of Imboassica Coastal Lagoon, Rio de Janeiro, Brazil. Journal of Coastal Research SI 36:634–639.

San Elijo Lagoon Conservancy, AECOM. 2016. Environmental Impact Report/ Environmental Impact Statement for the San Elijo Lagoon Restoration Project EIR/EIS.

SANDAG. (2018). 2018 Regional Monitoring Report.

Scott, D. B., Mudie, P. J., & Bradshaw, J. S. (2011). Coastal Evolution of Southern California as Interpreted from Benthic Foraminifera, Ostracodes, and Pollen. Journal of Foraminiferal Research, 41(3), 285 307.

Sediment TMDL for Los Peñasquitos Lagoon. (2014).

Seim, H. E., & Gregg, M. C. (1997). The importance of aspiration and channel curvature in producing strong vertical mixing over a sill. Journal of Geophysical Research: Oceans, 102(C2), 3451–3472. https://doi.org/10.1029/96jc03415

Selker, J. S., Thévenaz, L., Huwald, H., Mallet, A., Luxemburg, W., van de Giesen, N., et al. (2006). Distributed fiber-optic temperature sensing for hydrologic systems. Water Resources Research, 42(12). https://doi.org/10.1029/2006wr005326

Shanafield, Banks, E., Arkwright, J., & Hausner. (2018). Fiber-Optic Sensing for Environmental Applications: Where We Have Come From and What Is Possible. Water Resources Research, 54(11), 8552–8557. https://doi.org/10.1029/2018wr022768

Shepard, Christine C., Caitlin M. Crain, and Michael W. Beck. (2011). The Protective Role of Coastal Marshes: A Systematic Review and Meta-analysis. PLoS ONE 6(11): e27374–11. doi:10.1371/journal.pone.0027374.

Siler, N., Kosaka, Y., Xie, S.-P., & Li, X. (2017). Tropical ocean contributions to California's surprisingly dry El Niño of 2015/16. Journal of Climate, 30(24), 10067–10079. https://doi.org/10.1175/JCLI-D-17-0177.1

Siler, Nicholas, Yu Kosaka, Shang-Ping Xie, Xichen Li. (2017). Tropical ocean contribution to California's surprisingly dry El Niño of 2015/2016. Journal of Climate 30:10067-10079.doi: 10.1175/JCLI-D-17-0177.1

Simpson, J., Brown, J., Matthews, J., & Allen, G. (1990). Tidal straining, density currents, and stirring in the control of estuarine stratification. Estuaries, 13(2), 125–132. https://doi.org/10.2307/1351581

Southern California Wetlands Recovery Project. (2018). Wetlands on the Edge: The Future of Southern California's Wetlands: Regional Strategy 2018. Prepared by the California State Coastal Conservancy, Oakland, Ca.

Sousa, M. & Vaz, Nuno & Dias, João. (2011). Physical forcing of the water temperature variability along the Espinheiro Channel (Ria de Aveiro, Portugal). Journal of Coastal Research. 1594-1598.

Sweet, William V, R Horton, R E Kopp, A N LeGrande, and A Romanou. (2017). Sea level rise. Climate science special report fourth national climate assessment, Volume I. 333-363. doi:10.7930/J0VM49F2.

Sweet, William V., and Joseph Park. (2014). From the extreme to the mean: Acceleration and tipping points of coastal inundation from sea level rise. Earths Future 2: 1–22. doi:10.1002/28ISSN/92328-4277.

Tagliapietra, D., M. Sigovini, A.V. Ghirardini. (2009). A review of terms and definitions to categorise estuaries, lagoons and associated environments. Mar. Freshw. Res., 60, pp. 497-509.

Takekawa, John Y., Isa Woo, Rachel Gardiner, Michael Casazza, Joshua T. Ackerman, Nadav Nur, Leonard Liu, and Hildie Spautz. (2011). Avian Communities in Tidal Salt Marshes

of San Francisco Bay: A Review of Functional Groups by Foraging Guild and Habitat Association. San Francisco Estuary and Watershed Science 9: 1–25.

Tebaldi, Claudia, Bejamin H. Strauss, and Chris E. Zervas. (2012). Modeling sea-level rise impacts on storm surges along US Coasts. Environmental Research Letters 7: 14032 doi:10.1088/1748-9326/7/1/014032.

Teske, P. R., & Wooldridge, T. (2001). A comparison of the macrobenthic faunas of permanently open and temporarily open/closed South African estuaries. Hydrobiologia, 464(1–3), 227–243. https://doi.org/10.1023/a:1013995302300

Teske, Peter R, and Tris Wooldridge. (2001). A comparison of the macrobenthic faunas of permanently open and temporarily open/closed South African estuaries. Hydrobiologia 464: 227–243. doi:10.1023/A:1013995302300.

Thomson, R. E., & Emery, W. J. (2014). Data Analysis Methods in Physical Oceanography (Third Edition), 593–637. https://doi.org/10.1016/b978-0-12-387782-6.00006-5

Thomson, Richard E., and William J. Emery. (2014). Data Analysis Methods in Physical Oceanography, Third Edition. Waltham, MA: Elsevier B.V.

Thorne, Karen M, Deborah L Elliott-Fisk, Chase M Freeman, Thuy-Vy D Bui, Katherine W Powelson, Christopher N Janousek, Kevin J Buffington, and John Y Takekawa. (2017). Are coastal managers ready for climate change? A case study from estuaries along the Pacific coast of the United States. Ocean & Coastal Management 143. Ocean & Coastal Management: 38–50. doi:10.1016/j.ocecoaman.2017.02.010.

Thorne, Karen M., Glen M. MacDonald, Rich F. Ambrose, Kevin J. Buffington, Chase M. Freeman, Christopher N. Janousek, Lauren N. Brown, James R. Holmquist, Glenn R. Guntenspergen, Katherine W. Powelson, Patrick L. Barnard, and John Y. Takekawa. (2016). Effects of climate change on tidal marshes along a latitudinal gradient in California. U.S. Geological Survey Open-File Report 2016-1125:1–87. doi:10.3133/ofr20161125.

Thorne, Karen, Glen MacDonald, Glenn Guntenspergen, Richard Ambrose, Kevin Buffington, Bruce Dugger, Chase Freeman, Christopher Janousek, Lauren Brown, Jordan Rosencranz, James Holmquist, John Smol, Kathryn Hargan, and John Takekawa. (2018). U.S. Pacific coastal wetland resilience and vulnerability to sea-level rise. Science Advances 4:eaao327. doi:10.1126/sciadv.aao3270.

Tidesandcurrents.noaa.gov. 2018. NOAA Products Tides and Water Levels, https://tidesandcurrents.noaa.gov/stations.html?type=Water+Levels, Station IDs: 9410230, 9410660, 9410170, and 9410840. Accessed February 2019.

Tyler, S. W., Selker, J. S., Hausner, M. B., Hatch, C. E., Torgersen, T., Thodal, C. E., & Schladow, G. S. (2009). Environmental temperature sensing using Raman spectra DTS fiber-optic methods. Water Resources Research, 45(4). https://doi.org/10.1029/2008wr007052

Uncles, R. J., Stephens, J. A., & Harris, C. (2014). Freshwater, tidal and wave influences on a small estuary. Estuarine, Coastal and Shelf Science, 150, 252–261. https://doi.org/10.1016/j.ecss.2014.05.035

van Belzen, Jim, Johan van de Koppel, Matthew Kirwan, Daphne van der Wal, Peter Herman, Vasilis Dakos, Sonia Kéfi, Marten Scheffer, Glenn Guntenspergen, and Tjeerd Bouma. (2017). Vegetation recovery in tidal marshes reveals critical slowing down under increased inundation. Nature Communications 8. nature: ncomms15811. doi:10.1038/ncomms15811.

van Emmerik, T. H. M., Rimmer, A., Lechinsky, Y., Wenker, K. J. R., Nussboim, S., & van de Giesen, N. C. (2013). Measuring heat balance residual at lake surface using Distributed Temperature Sensing. Limnology and Oceanography: Methods, 11(2), 79–90. https://doi.org/10.4319/lom.2013.11.79

Vercauteren, N., Huwald, H., Bou-Zeid, E., Selker, J. S., Lemmin, U., Parlange, M. B., & Lunati, I. (2011). Evolution of superficial lake water temperature profile under diurnal radiative forcing. Water Resources Research, 47(9). https://doi.org/10.1029/2011wr010529

Walters, R. A., & Heston, C. (1982). Notes and Correspondence: Removing Tidal-Period Variations from Time-Series Data Using Low-Pas Digital Filters. Journal of Physical Oceanography, 12. doi:10.1175/1520-0485.

Waterdata.usgs.gov. (2018). https://waterdata.usgs.gov/ca/nwis/uv/ National Water Information System: USGS Stream Gauge: 11023340. Accessed February 2019.

White, M. D., & Greer, K. A. (2006). The effects of watershed urbanization on the stream hydrology and riparian vegetation of Los Peñasquitos Creek, California. Landscape and Urban Planning, 74(2), 125–138. https://doi.org/10.1016/j.landurbplan.2004.11.015

Whitfield, A. K. (1992). The characterization of southern African estuarine systems. Southern African Journal of Aquatic Sciences 26, 31–38.

WIlliams, M. E. (2014). Hydrodynamics and Salt Dispersion in Intermittenly Closed Bar-Built Estuaries, 1 115.

Williams, M., & Stacey, M. (2016). Tidally discontinuous ocean forcing in bar-built estuaries: The interaction of tides, infragravity motions, and frictional control. Journal of Geophysical Research: Oceans, 121(1), 571–585. https://doi.org/10.1002/2015jc011166

Williams, Megan E., and Mark T. Stacey. (2016). Tidally discontinuous ocean forcing in bar-built estuaries: The interaction of tides, infragravity motions, and frictional control. Journal of Geophysical Research: Oceans 121: 571–585. doi:10.1002/2015JC011166.

Young, Adam P., Reinhard E. Flick, Timu W. Gallien, Sarah N. Giddings, Robert T. Guza, Madeleine Harvey, Luc Lenain, Bonnie C. Ludka, W. Kendall Melville, and William C. O'Reilly. 2018. Southern California Coastal Response to the 2015-2016 El Niño . Journal of Geophysical Research: Earth Surface 123:3069-3083. doi:10.1029/2018JF004771

Zedler, Joy B. (2010). How frequent storms affect wetland vegetation: a preview of climate-change impacts. Frontiers in Ecology and the Environment 8: 540–547. doi:10.1890/090109.

Zedler, Joy B., and Suzanne Kercher. (2005). Wetland Resources: Status, Trends, Ecosystem Services, and Restorability. Annual Review of Environment and Resources 30: 39–74. doi:10.1146/annurev.energy.30.050504.144248.